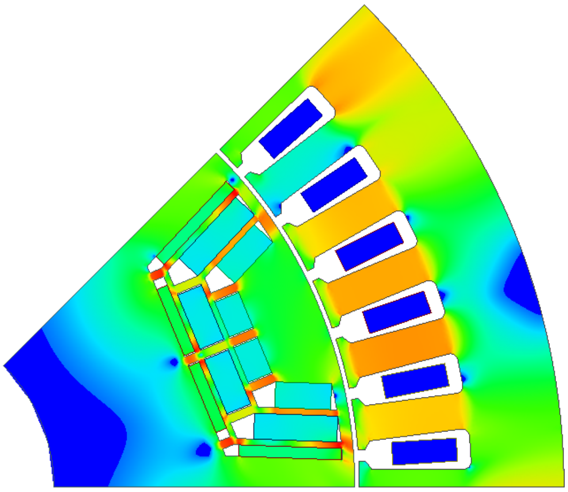

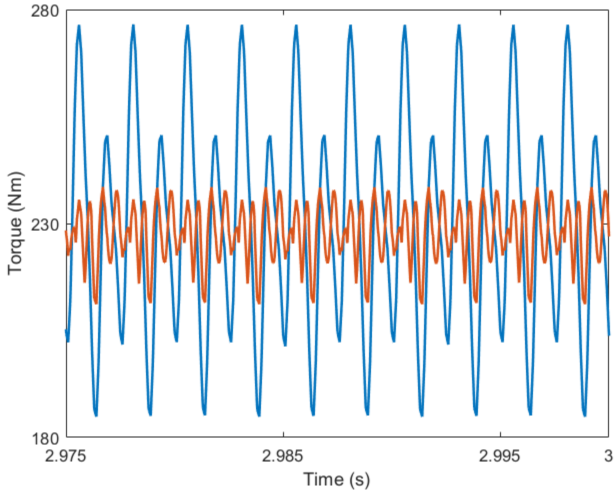

Design and Comparative Analysis of PM Traction Machines with Harmonic Current-Based Torque Ripple Reduction for Electric Truck Applications

Design and Comparative Analysis of PMaSynRM and Spoke-Type PMSM with Optimal Torque Ripple Control for Electric Truck Applications using LQI Regulator, Linear Time-Varying Kalman Filter and Torque Ripple Optimizer

Master's thesis in Master programmes: Mobility Engineering, Sustainable Electric Power Engineering and Electromobility

HRISHIKESH GIRISH SHIRSAT, VISHALI KANNAN

DEPARTMENT OF ELECTRICAL ENGINEERING
CHALMERS UNIVERSITY OF TECHNOLOGY
Gothenburg, Sweden 2026
www.chalmers.se

Master's thesis 2026

Design and Comparative Analysis of PM Traction Machines with Harmonic Current-Based Torque Ripple Reduction for Electric Truck Applications

Design and Comparative Analysis of PMaSynRM and Spoke-Type PMSM with Optimal Torque Ripple Control for Electric Truck Applications using LQI Regulator, Linear Time-Varying Kalman Filter and Torque Ripple Optimizer

Hrishikesh Girish Shirsat
Vishali Kannan

Department of Electrical Engineering
Division of Electric Power Engineering
Chalmers University of Technology
Gothenburg, Sweden 2026

Design and Comparative Analysis of PM Traction Machines with Harmonic Current-Based Torque Ripple Reduction for Electric Truck Applications
Design and Comparative Analysis of PMaSynRM and Spoke-Type PMSM with Optimal Torque Ripple Control for Electric Truck Applications using LQI Regulator, Linear Time-Varying Kalman Filter and Torque Ripple Optimizer
HRISHIKESH GIRISH SHIRSAT
VISHALI KANNAN

Supervisor: Torbjörn Thiringer, Department of Electrical Engineering
Examiner: Torbjörn Thiringer, Department of Electrical Engineering

Master's Thesis 2026
Department of Electrical Engineering
Division of Electric Power Engineering
Chalmers University of Technology
SE-412 96 Gothenburg
Telephone +46 31 772 1000

Cover: A magnetic field plot of PMaSynRM motor and a plot of torque ripple reduction

Typeset in LaTeX
Printed by Chalmers Reproservice
Gothenburg, Sweden 2026

Design and Comparative Analysis of PM Traction Machines with Harmonic Current-Based Torque Ripple Reduction for Electric Truck Applications
HRISHIKESH GIRISH SHIRSAT
VISHALI KANNAN
Department of Electrical Engineering
Chalmers University of Technology

Abstract

Permanent magnet traction machines for electric truck applications must combine high torque capability, wide speed operation, high efficiency, low material cost, and reduced dependence on rare-earth magnets. This thesis presents the design, finite-element analysis, drive-cycle evaluation, sustainability assessment, and torque ripple reduction of three machine topologies: a hybrid-magnet permanent magnet-assisted synchronous reluctance machine (PMaSynRM), a ferrite spoke-type permanent magnet synchronous machine (PMSM), and a NdFeB V-type PMSM used as a reference. The comparison considers torque-speed and power-speed capability, field-weakening performance, loss and efficiency behaviour, magnetic saturation, demagnetization, mechanical rotor stress, material usage, cost, and environmental impact.

The results show that all three machines can meet the required traction performance, but with different trade-offs. The NdFeB V-PMSM provides the most compact design and strong torque production, but it is the most expensive solution and has the highest CO_2e per kilogram due to its strong dependence on NdFeB magnet material. The ferrite spoke PMSM reduces rare-earth magnet dependency and achieves the highest power capability in the field-weakening region by using ferrite magnets and flux concentration. It is also the cheapest machine and has the lowest CO_2e per kilogram, but its larger and heavier structure leads to higher total emissions and increased core losses, especially at higher speeds. The hybrid PMaSynRM, which uses both ferrite and NdFeB magnets, reduces NdFeB usage while maintaining competitive torque-speed performance, low drive-cycle losses, and high average efficiency. Overall, it offers the best compromise between electromagnetic performance, rare-earth magnet reduction, cost, efficiency, and sustainability.

In addition to the motor design comparison, this thesis investigates steady-state torque ripple reduction using a map-based reduced-order model. A field-oriented control structure with feedforward voltage compensation and LQI current control is implemented, including digital controller sampling delays and zero-order hold effects. A linear time-varying Kalman filter is used to estimate flux components and torque, while a harmonic current optimizer modifies selected current harmonic components to reduce torque ripple without causing drift in the mean current or mean torque. The proposed optimizer achieves torque ripple reduction of up to 70-80% at steady state while respecting inverter switching constraints. The Kalman filter accurately estimates fluxes and mean torque but cannot fully reconstruct torque ripple caused by cogging and slotting effects.

Keywords: Permanent Magnet Synchronous Machine (PMSM), PM-assisted Synchronous Reluctance Motor (PM-SynRM), Torque Ripple Reduction, Electric Vehicles (EV), Spoke-Type PMSM, Field-Oriented Control (FOC), Kalman Filter (KF), Harmonic Current Injection, Finite Element Analysis (FEA)

Acknowledgements

We would like to sincerely thank Chalmers University of Technology for giving us the opportunity to carry out this thesis and for providing a supportive environment throughout our work. The resources, learning atmosphere, and academic guidance at Chalmers helped us develop our understanding and apply our knowledge to a challenging and meaningful project. This thesis has been an important part of our journey, and the experience has helped us grow both as students and as future engineers. We are especially grateful to Professor Torbjörn Thiringer for his guidance, patience, and support during the thesis. His feedback and suggestions helped us improve our work step by step and gave us clarity whenever we faced difficulties. We truly appreciate the time he spent discussing our ideas, reviewing our progress, and encouraging us throughout the project. We would also like to thank our friends, classmates, and family members for their constant support and motivation during this period.

Hrishikesh Girish Shirsat
Vishali Kannan
Gothenburg, 2026

List of Acronyms

AC	Alternating Current
AI	Artificial Intelligence
AI-ML	Artificial Intelligence–Machine Learning
CAD	Computer-Aided Design
DC	Direct Current
DSP	Digital Signal Processor
EKF	Extended Kalman Filter
EMF	Electromotive Force
EV	Electric Vehicle
FEA	Finite Element Analysis
FOC	Field-Oriented Control
FoS	Factor of Safety
FPGA	Field-Programmable Gate Array
FW	Field Weakening
HEV	Hybrid Electric Vehicle
IPMSM	Interior Permanent Magnet Synchronous Machine
KF	Kalman Filter
LQI	Linear Quadratic Integral Regulator
LQR	Linear Quadratic Regulator
LUT	Look-Up Table
LTV	Linear Time-Varying
MMF	Magnetomotive Force
MTPA	Maximum Torque Per Ampere
MTPV	Maximum Torque Per Voltage
NdFeB	Neodymium-Iron-Boron
NEDC	New European Driving Cycle
NVH	Noise, Vibration and Harshness
PI	Proportional-Integral
PM	Permanent Magnet
PMaSynRM	Permanent Magnet-Assisted Synchronous Reluctance Motor
PM-SynRM	Permanent Magnet-Assisted Synchronous Reluctance Motor
PMSM	Permanent Magnet Synchronous Machine
PWM	Pulse-Width Modulation
RLS	Recursive Least Squares

RMS	Root Mean Square
ROM	Reduced-Order Model
RPM	Revolutions Per Minute
SVM	von Mises Stress, as used for rotor mechanical stress analysis
WLTC	Worldwide Harmonized Light Vehicles Test Cycle
ZOH	Zero-Order Hold

Nomenclature

Indices and Subscripts

a, b, c	Stator phase quantities in the three-phase reference frame
d, q	Direct- and quadrature-axis quantities in the synchronous reference frame
e	Electrical quantity
k	Discrete-time sample index
m	Mass of the vehicle chosen
$6, 12$	Sixth- and twelfth-order harmonic components
ff	Feedforward component
ref	Reference value
avg	Average value
max	Maximum value
min	Minimum value
$\theta_{e,k}$	Electrical rotor-angle grid point used in angle-dependent modelling
$\{I_d\}$	Set of d-axis current breakpoints used in the ROM plant model
$\{I_q\}$	Set of q-axis current breakpoints used in the ROM plant model
N	Number of samples or electrical-angle points

Variables

ρ	Air density
C_d	Aerodynamic drag coefficient
A_f	Vehicle frontal area
C_{rr}	Rolling-resistance coefficient
m_{eq}	Equivalent vehicle mass including rotating inertias
g	Gravitational acceleration

θ	Road grade angle
r_w	Effective wheel rolling radius
i_{tot}	Total gear ratio between motor and wheels
η_{dl}	Driveline efficiency
P_{max}	Maximum mechanical power capability
ω_{base}	Base angular speed of the traction motor
P	Number of poles
p	Number of pole pairs
m	Number of stator phases when used in winding equations
q	Number of slots per pole per phase
g	Air-gap length
d_{wire}	Diameter of an individual copper strand or wire
k_{fill}	Slot fill factor
R_s	Stator phase resistance
L_d	Direct-axis inductance
L_q	Quadrature-axis inductance
ψ_m	Permanent-magnet flux linkage
I_{max}	Maximum allowable stator current magnitude
V_{max}	Maximum allowable dq voltage magnitude
V_{dc}	DC-link voltage
μ	Magnetic permeability
μ_0	Permeability of free space
μ_r	Relative permeability
$\mathcal{R}$	Magnetic reluctance
l	Magnetic path length
A	Cross-sectional area of a magnetic path
l_{eff}	Effective active stack length
r	Air-gap radius
B_r	Magnet residual flux density
H_{cB}	Coercive force of the magnet
H_{cJ}	Intrinsic coercive force of the magnet
$(BH)_{max}$	Maximum energy product of the magnet
f	Frequency
f_e	Electrical frequency

f_{sw}	Inverter switching frequency
T_s	Sampling period
λ	Leakage coefficient of the leaky voltage-model flux observer
D_r	Rotor outer diameter
D_{sh}	Shaft diameter
W	Magnet width in the motor geometry
T	Magnet thickness
R	Rotor rib thickness in geometry tables
A	V-angle of the embedded magnet pair in the V-PMSM geometry
W_1, W_4	NdFeB center and side magnet widths in the PMaSynRM rotor
W_2, W_5	Middle ferrite center and side magnet widths in the PMaSynRM rotor
W_3, W_6	Outer ferrite center and side magnet widths in the PMaSynRM rotor
T_1	NdFeB magnet thickness in the PMaSynRM rotor
T_2	Middle ferrite magnet thickness in the PMaSynRM rotor
T_3	Outer ferrite magnet thickness in the PMaSynRM rotor
L_1	NdFeB magnet distance from rotor center
L_2	Middle ferrite magnet distance from rotor center
L_3	Outer ferrite magnet distance from rotor center
F_{trac}	Required tractive force at the driven wheels
F_{aero}	Aerodynamic drag force
F_{roll}	Rolling-resistance force
F_{grade}	Grade-resistance force
v	Vehicle speed
$\frac{dv}{dt}$	Longitudinal vehicle acceleration
T_w	Wheel torque
T_m	Motor mechanical torque
T_e	Electromagnetic torque
T_{PM}	Permanent-magnet torque component
T_{rel}	Reluctance torque component
T_{actual}	Total actual electromagnetic torque including residual effects
T_{res}	Residual torque component, including cogging torque and nonlinear effects
T_L	Load torque

P_{mech} — Mechanical output power

P_{out} — Output mechanical power used in efficiency calculation

P_{loss} — Total electromagnetic loss

P_{cu} — Stator copper loss

P_{fe} — Iron or core loss

P_{pm} — Permanent-magnet eddy-current loss

P_{hyst} — Hysteresis loss

P_{eddy} — Eddy-current loss

η — Efficiency

ω_w — Wheel angular speed

ω_m — Mechanical angular speed of the motor

ω_e — Electrical angular speed

θ_e — Electrical rotor position

θ_m — Mechanical rotor position

Φ — Magnetic flux

$\mathcal{F}$ — Magnetomotive force

$\mathcal{F}_g$ — Air-gap magnetomotive force

$\mathcal{F}_\theta$ — Tangential electromagnetic force

B — Magnetic flux density

B_{rad} — Radial component of air-gap flux density

B_{tan} — Tangential component of air-gap flux density

H — Magnetic field intensity

τ_θ — Tangential magnetic shear stress

W'_m — Magnetic co-energy

P_{hyst} — Hysteresis loss

P_{eddy} — Eddy-current loss

η — Efficiency

ω_w — Wheel angular speed

ω_m — Mechanical angular speed of the motor

ω_e — Electrical angular speed

θ_e — Electrical rotor position

θ_m — Mechanical rotor position

Φ — Magnetic flux

$\mathcal{F}$ — Magnetomotive force

$\mathcal{F}_g$	Air-gap magnetomotive force
$\mathcal{F}_\theta$	Tangential electromagnetic force
B	Magnetic flux density
B_{rad}	Radial component of air-gap flux density
B_{tan}	Tangential component of air-gap flux density
H	Magnetic field intensity
τ_θ	Tangential magnetic shear stress
W'_m	Magnetic co-energy
p_{fe}	Specific core loss
p_h	Specific hysteresis loss component
p_{cl}	Specific classical eddy-current loss component
p_{exc}	Specific excess loss component
k_h	Hysteresis-loss coefficient
k_{cl}	Classical eddy-current-loss coefficient
k_{exc}	Excess-loss coefficient
α	Steinmetz exponent for hysteresis loss
k_{bf}	Core-loss build factor
δ	Skin depth of the conductor
A_i	Cross-sectional area of active material i
L_{stk}	Active stack length
V_i	Volume of active material i
ρ_i	Density of active material i
m_i	Mass of active material i
c_i	Unit cost of active material i
C_i	Cost of active material i
CE_i	Embodied carbon emission of material i
CF_i	Carbon-emission factor of material i
$\mathbf{x}$	State vector
$\mathbf{u}$	Input vector
$\mathbf{y}$	Output or measurement vector
$\delta\mathbf{x}$	Small-signal state deviation from the operating point
$\delta\mathbf{u}$	Small-signal input deviation from the operating point
$\mathbf{A}$	Continuous-time state matrix or Jacobian with respect to states
$\mathbf{B}$	Continuous-time input matrix or Jacobian with respect to inputs

$\mathbf{A}_{avg}$	Angle-averaged continuous-time state matrix
$\mathbf{B}_{avg}$	Angle-averaged continuous-time input matrix
$\mathbf{A}_d$	Discrete-time state matrix
$\mathbf{B}_d$	Discrete-time input matrix
$\mathbf{A}_{aug}$	Augmented discrete-time state matrix for LQI design
$\mathbf{B}_{aug}$	Augmented discrete-time input matrix for LQI design
$\mathbf{C}$	Output matrix
$\mathbf{D}$	Feedthrough matrix
$\mathbf{M}$	Differential flux-linkage matrix used in the nonlinear ROM plant
$\mathbf{e}$	Current tracking error vector
$\boldsymbol{\xi}$	Integral state vector in the LQI controller
$\mathbf{Q}$	State-weighting matrix in LQI design or process-noise covariance in Kalman filtering
$\mathbf{R}$	Input-weighting matrix in LQI design or measurement-noise covariance in Kalman filtering
$\mathbf{P}$	Riccati matrix in LQI design or estimation-error covariance in Kalman filtering
$\mathbf{K}_{aug}$	Augmented LQI gain matrix
$\mathbf{K}_x$	LQI proportional state-feedback gain
$\mathbf{K}_i$	LQI integral gain
$\Delta\mathbf{u}$	Feedback voltage correction generated by the LQI controller
u_d, u_q	Feedback-controller voltage outputs in the dq frame
$v_{d,ff}, v_{q,ff}$	Feedforward dq-axis voltage components
J	Cost function used in rotor optimization or torque-ripple optimization; also rotational inertia in the mechanical equation depending on context
T_{max}	Maximum torque over one electrical period
T_{min}	Minimum torque over one electrical period
T_{avg}	Average torque over one electrical period
T_{rms}	RMS value of torque ripple
T_{mean}	Mean torque during harmonic injection
$T_{mean,baseline}$	Mean torque without harmonic injection
ω	Penalty weight in the torque-ripple optimizer cost function when used outside speed equations
$\mathbf{c}$	Harmonic coefficient vector used by the torque-ripple optimizer

i_{d0}, i_{q0}	Mean or fundamental dq-axis current references before harmonic injection
a_{d6}, b_{d6}	Cosine and sine coefficients of the sixth-order d-axis flux harmonic
a_{q6}, b_{q6}	Cosine and sine coefficients of the sixth-order q-axis flux harmonic
a_{d12}, b_{d12}	Cosine and sine coefficients of the twelfth-order d-axis flux or current harmonic
a_{q12}, b_{q12}	Cosine and sine coefficients of the twelfth-order q-axis flux or current harmonic
A_{d12}	Amplitude of the twelfth-order d-axis injected current harmonic
A_{q6}	Amplitude of the sixth-order q-axis injected current harmonic
A_{q12}	Amplitude of the twelfth-order q-axis injected current harmonic
ϕ_{d12}	Phase angle of the twelfth-order d-axis harmonic
ϕ_{q6}	Phase angle of the sixth-order q-axis harmonic
ϕ_{q12}	Phase angle of the twelfth-order q-axis harmonic
c_6, s_6	Shorthand notation for $\cos(6\theta_e)$ and $\sin(6\theta_e)$
c_{12}, s_{12}	Shorthand notation for $\cos(12\theta_e)$ and $\sin(12\theta_e)$
$\hat{\mathbf{x}}_{k\|k-1}$	Predicted state estimate before measurement correction
$\hat{\mathbf{x}}_{k\|k}$	Corrected state estimate after measurement correction
$\hat{\mathbf{y}}_k$	Predicted measurement vector
$\tilde{\mathbf{y}}_k$	Modified measurement vector after subtracting known resistive voltage drops
$\mathbf{w}_k$	Process-noise vector
$\mathbf{v}_k$	Measurement-noise vector
$\boldsymbol{\nu}_k$	Innovation vector in the Kalman filter
$\mathbf{S}_k$	Innovation covariance matrix
$\mathbf{K}_k$	Kalman gain matrix
$\psi_{d,init}, \psi_{q,init}$	Initial dq-axis flux values used in the leaky voltage-model flux observer

Contents

1 Introduction

The demand for electrified transport is increasing, which in turn increases the need for high-efficiency, high-power-density traction systems, especially for commercial electric vehicles. In recent years, certain machine topologies, such as Permanent Magnet-assisted Synchronous Reluctance Motors (PMaSynRMs) and Spoke-Type Permanent Magnet Synchronous Machines (PMSMs), have attracted significant research interest due to their advantages in efficiency, torque density, field-weakening capability, and reduced rare-earth magnet usage. However, both topologies are mainly affected by torque ripple caused by slotting effects, magnetic saturation, and air-gap flux harmonics, which degrade drive performance and increase noise and vibration. Therefore, the development of these motor designs requires careful electromagnetic design, with proper selection of rotor geometry, magnet arrangement, winding configuration, and slot-pole combination, supported by finite element analysis for performance evaluation.In addition, suitable control strategies are required to ensure smooth torque production and high drive performance over the operating range.

1.1 Problem description

In PMaSynRM and Spoke-Type PMSM traction drives for heavy-duty EVs, torque ripple remains a critical challenge because it causes vibration, acoustic noise, reduced control accuracy, and increased mechanical stress, especially at high torque and over a wide speed range. It arises mainly from slotting, air-gap flux harmonics, magnetic saturation, and inverter-induced current harmonics. Therefore, integrated design-and-control strategies with advanced current control are required to cancel dominant ripple components while limiting additional copper and iron losses across the operating region [1].

1.2 Previous work

Prior research on torque ripple reduction in PMaSynRMs and related PM-assisted saliency machines shows that the ripple originates from rotor–stator geometric interactions, spatial harmonics, and saturation. Also, some work shows that careful rotor flux-barrier shaping and placement can lower torque pulsations by modifying air-gap permeance harmonics and smoothing the reluctance torque production while preserving the torque capability [1]. In parallel, the drive related studies shows that the periodic disturbances oriented current controllers can attenuate torque ripple by rejecting/cancelling dominant harmonic components in the current/torque path, improving torque smoothness without requiring extensive mechanical changes [2]. However, most previous studies focus either on machine design or on control design separately. A comparative study that combines electromagnetic design, magnet selection, and torque-ripple reduction for both PMaSynRM and spoke-type PMSM traction motors in heavy-duty EV applications remains limited.

1.3 Purpose

The purpose of this thesis is to design and compare different traction PM topologies for EV truck applications using FEA and performance mapping. Both rare-earth and ferrite magnet variants are evaluated in order to quantify performance, cost, and the associated design trade-offs. Short-circuit and demagnetization analyses are carried out to assess fault behaviour and magnet integrity. Drive-cycle simulations are used to evaluate energy consumption and torque quality under realistic operating conditions. Additionally a Field Oriented Controller is to be designed and equipped with Torque Ripple Optimizer and Parameter Estimator (Kalman Filter), with a target torque-ripple reduction of 70-80%.

2

PMSM Theory

2.1 Vehicle Dynamics

2.1.1 Longitudinal Vehicle Dynamics

The traction motor requirements are derived from the longitudinal motion of the vehicle. During driving, the tractive force at the wheels must overcome the external road-load forces and provide the force required for vehicle acceleration. The main longitudinal forces acting on a vehicle travelling on an inclined road are illustrated in Figure 2.1.

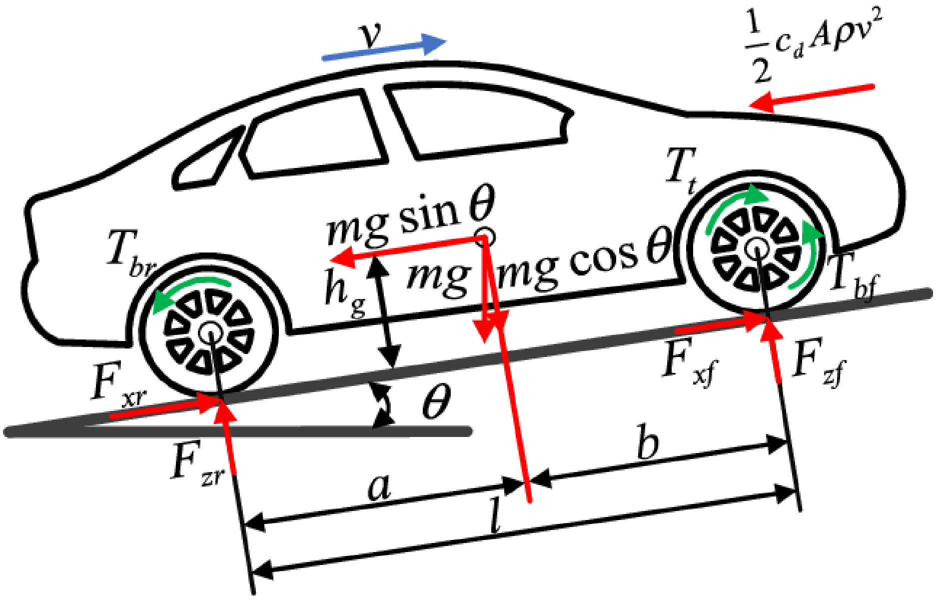

Figure 2.1: Longitudinal vehicle dynamics force diagram showing aerodynamic drag, gravitational force components, normal reactions, longitudinal tire forces, wheel torques, road grade angle and vehicle velocity [3]

As shown in Figure 2.1, the vehicle is subjected to aerodynamic drag, rolling resistance, grade resistance and inertia during acceleration. The road grade angle θ divides the vehicle weight into a normal component $mg\cos\theta$ and a longitudinal component $mg\sin\theta$. The normal component influences the normal reactions at the front and rear wheels while the longitudinal component acts against the motion during uphill driving and assists the motion during downhill driving.

The longitudinal force balance can be written as

$$F_{\text{trac}} = F_{\text{aero}} + F_{\text{roll}} + F_{\text{grade}} + m_{\text{eq}}\frac{dv}{dt}, \tag{2.1}$$

where F_{trac} is the required tractive force at the driven wheels, v is the vehicle speed, m_{eq} is the equivalent vehicle mass, and dv/dt is the longitudinal acceleration. The equivalent mass includes the effect of rotating inertias in the wheels, driveline and electric machine.

The road-load forces are expressed as

$$F_{\text{aero}} = \frac{1}{2}\rho C_d A_f v^2, \tag{2.2}$$

$$F_{\text{roll}} = C_{\text{rr}} mg\cos\theta, \tag{2.3}$$

$$F_{\text{grade}} = mg\sin\theta, \tag{2.4}$$

where ρ is the air density, C_d is the aerodynamic drag coefficient, A_f is the frontal area, C_{rr} is the rolling resistance coefficient, m is the vehicle mass, g is the gravitational acceleration and θ is the road grade angle. The aerodynamic drag increases with the square of vehicle speed while rolling resistance is mainly proportional to the normal load on the tires. The grade resistance becomes significant when the vehicle is travelling on an inclined road.

The required tractive force is related to the wheel torque demand by

$$T_{\text{w}} = F_{\text{trac}} r_{\text{w}}, \tag{2.5}$$

where T_{w} is the wheel torque and r_{w} is the rolling radius of the tire. The corresponding wheel angular speed is

$$\omega_{\text{w}} = \frac{v}{r_{\text{w}}}. \tag{2.6}$$

The driveline and gearbox are used to transform torque and speed between the motor and the wheels. The total gear ratio is defined as

$$i_{\text{tot}} = \frac{\omega_{\text{m}}}{\omega_{\text{w}}}, \tag{2.7}$$

where ω_{m} is the motor angular speed. During traction operation the motor torque required to produce the wheel torque is

$$T_{\text{m}} = \frac{T_{\text{w}}}{i_{\text{tot}}\eta_{\text{dl}}}, \tag{2.8}$$

where η_{dl} is the driveline efficiency. This efficiency accounts for mechanical losses in the transmission, bearings, differential and other driveline components. Therefore the gear ratio increases the torque available at the wheels while the motor rotates at a higher speed than the wheels.

2.1.2 Torque-Speed and Power Requirements

The traction motor of an electric vehicle must satisfy two main requirements. First, it must provide high torque at low vehicle speed for vehicle launch, acceleration, start-stop driving and gradeability. Second, it must provide sufficient power at higher vehicle speeds for cruising and high-speed transients.

The mechanical output power is given by

$$P_{\mathrm{mech}} = T_{\mathrm{m}}\omega_{\mathrm{m}} \tag{2.9}$$

where P_{mech} is the mechanical output power, T_{m} is the motor torque, and ω_{m} is the motor mechanical angular speed.

At low and medium speeds the motor is usually current-limited. In this region the maximum torque is constant and the output power increases almost linearly with speed

$$P_{\mathrm{mech}} \propto \omega_{\mathrm{m}} \tag{2.10}$$

Above the base speed, the motor becomes voltage-limited because the back-EMF increases with speed. The machine then enters the field-weakening region. In this region, the available torque decreases with speed in order to keep the output power within the maximum power capability. The torque in the field-weakening region is given by

$$T_{\mathrm{m}}(\omega_{\mathrm{m}}) \approx \frac{P_{\mathrm{max}}}{\omega_{\mathrm{m}}}, \qquad \omega_{\mathrm{m}} > \omega_{\mathrm{base}} \tag{2.11}$$

where P_{max} is the maximum mechanical power and ω_{base} is the base speed.

2.2 Traction Machines Considered

Two permanent magnet traction machine topologies are considered in this thesis: a permanent magnet assisted synchronous reluctance machine (PMaSynRM) and a spoke type permanent magnet synchronous machine (spoke type PMSM). Both topologies are suitable candidates for traction applications because they can provide high torque density, high efficiency, and field-weakening capability. However they achieve these characteristics through different rotor structures and torque-production mechanisms.

2.2.1 PM-Assisted Synchronous Reluctance Machine Principles

A synchronous reluctance machine produces torque due to rotor saliency. The rotor contains flux barriers that create different magnetic reluctances along the direct and quadrature axes. As a result, the d and q axis inductances are unequal, and the rotor tends to align itself with the stator magnetic field in a position of minimum reluctance. This produces reluctance torque without requiring rotor windings or permanent magnets [4].

When permanent magnets are inserted into the flux barriers, the machine becomes a permanent magnet assisted synchronous reluctance machine (PMaSynRM). In this case, the total electromagnetic torque consists of two main components: the reluctance torque produced by rotor saliency and the permanent magnet torque produced by the interaction between the stator current and the magnet flux.

The use of permanent magnets improves the performance of a pure synchronous reluctance machine by increasing the air-gap flux, torque density, efficiency, and power factor. At the same time, the reluctance torque contribution allows the machine to use less permanent-magnet material than a conventional PMSM for a similar performance target. Therefore, the PMaSynRM is an attractive topology when the design objective is to balance traction performance with magnet cost, rare-earth material usage and sustainability considerations [4].

2.2.2 Spoke-Type PMSM Topology

The spoke type PMSM is an interior permanent-magnet topology in which the magnets are placed radially in the rotor similar to spokes in a wheel. The magnets are usually magnetized in the tangential direction. This arrangement causes the magnet flux to be concentrated through the rotor iron before crossing the air gap. As a result, the effective air-gap flux density can become higher than the remanent flux density of the magnet material itself. This flux concentration effect is especially useful when ferrite magnets are used because ferrite magnets have lower remanent flux density than NdFeB magnets [4].

The increased air-gap flux density improves the torque density of the machine for a given stator and rotor size. This makes the spoke type PMSM attractive for traction applications where high torque and high power density are required within inverter voltage and current limits.

However spoke type PMSMs also have several design challenges. Since the magnets are buried inside the rotor, part of the magnet flux may leak through rotor iron paths instead of crossing the air gap. This leakage flux reduces the useful air-gap flux and can reduce torque production. The rotor also requires bridges, ribs, or retaining structures to keep the magnets mechanically secure at high speed. These structures must be strong enough to withstand centrifugal forces, but they can also create additional leakage paths and local saturation. Therefore, the spoke-type PMSM requires careful electromagnetic and mechanical design especially for high-speed traction operation [4].

2.3 dq Modelling, Torque Production and Performance Characteristics

This section describes the electromagnetic torque-production mechanism and the *dq*-axis modelling framework used to analyse the electric machines.

2.3.1 Magnetic Circuit and Role of the Iron Core

The stator and rotor cores of the electric machines are made of laminated electrical steel. The purpose of the core material is to provide a low-reluctance path for the magnetic flux produced by the permanent magnets and stator windings. This is possible because soft magnetic materials have high permeability compared with air. The reluctance of a magnetic path can be written as

$$\mathcal{R} = \frac{l}{\mu A}, \tag{2.12}$$

where l is the magnetic path length, A is the cross-sectional area, and μ is the permeability of the material. The magnetomotive force (MMF) required to drive a flux Φ through this path is

$$\mathcal{F} = \Phi\mathcal{R}. \tag{2.13}$$

By Ampere's Law, the MMF drop along a magnetic path is

$$\mathcal{F} = \int H\,dl \tag{2.14}$$

where H is the magnetic field intensity. In the air gap,

$$B = \mu_0 H \tag{2.15}$$

whereas in the unsaturated region of the steel

$$B = \mu_0\mu_r H \tag{2.16}$$

with $\mu_r \gg 1$. Therefore for a given flux density B the required magnetic field intensity H is much smaller in the steel than in the air gap. This means that the MMF drop inside the stator and rotor cores is relatively small so most of the available MMF is applied across the air gap.

2.3.2 Effect of Magnetic Saturation

The low-reluctance behaviour of the steel is valid mainly in the unsaturated region of the B-H curve. As the flux density increases the magnetic domains in the material become increasingly aligned. Beyond the knee of the B-H curve, the permeability

$$\mu = \frac{dB}{dH} \tag{2.17}$$

decreases significantly. In this region a large increase in magnetic field intensity produces only a small additional increase in flux density. The steel therefore no longer behaves as an effective low-reluctance path.

Saturation is undesirable because it increases the MMF drop inside the iron. Therefore, more of the available magnet and winding excitation is consumed inside the core instead of being used across the air gap. In addition, the torque no longer increases proportionally with current since the additional current produces only a small increase in useful air-gap flux. This reduces the torque per ampere and may require higher current for the same torque thus increasing the copper loss.

Local saturation in the stator teeth, stator yoke, rotor bridges, or rotor ribs can also distort the air-gap flux-density waveform. This can increase torque ripple, acoustic noise and iron loss. Therefore, the machine should be designed so that the steel is used effectively without excessive local saturation.

2.3.3 Air-Gap Field and Maxwell-Stress Torque Production

The MMF drop across the air gap does not directly become torque. Instead, it establishes the air-gap magnetic field, and torque is produced by the tangential component of the electromagnetic stress in the air gap [5]. The sequence is as follows:

$$\mathcal{F}_g \to \mathbf{B}_g \to \tau_\theta \to F_\theta \to T_e, \tag{2.18}$$

where $\mathcal{F}_g$ is the air-gap MMF, $\mathbf{B}_g$ is the air-gap flux density, τ_θ is the tangential magnetic shear stress, F_θ is the tangential electromagnetic force and T_e is the electromagnetic torque.

The air-gap flux-density vector can be resolved into radial and tangential components as illustrated in Figure 2.2.

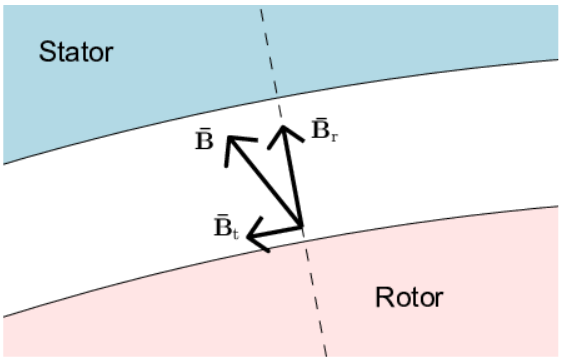

Figure 2.2: Components of the air-gap flux-density vector. The radial component $B_{\text{rad}} = B_r$ acts normal to the air-gap while the tangential component $B_{\text{tan}} = B_t$ produces electromagnetic shear stress [6]

The radial component acts mainly normal to the rotor surface, while the tangential component is associated with useful torque production.

A purely radial air-gap field mainly produces normal attraction between the stator and rotor. It contributes to radial force, vibration and acoustic noise, but it does not directly produce torque. Useful torque is produced when the air-gap field has a tangential stress component. Therefore both the magnitude and spatial orientation of the air-gap field are important for torque production [6].

The air-gap flux density can be decomposed as

$$\mathbf{B} = B_{\text{rad}}\hat{r} + B_{\text{tan}}\hat{\theta} \tag{2.19}$$

where B_{rad} is the radial component and B_{tan} is the tangential component. Using the Maxwell stress tensor the tangential shear stress in the air gap can be expressed as [5]

$$\tau_\theta = \frac{B_{\text{rad}}B_{\text{tan}}}{\mu_0} \tag{2.20}$$

For a radial-flux machine with active stack length l and air-gap radius r, the electromagnetic torque can be expressed as

$$T_e = \frac{lr^2}{\mu_0}\int_0^{2\pi} B_{\text{rad}}(\theta)B_{\text{tan}}(\theta)\,d\theta \tag{2.21}$$

Equation (2.21) shows that torque is produced by the product of the radial and tangential flux-density components. If the tangential component is zero, the field produces radial attraction but no average torque. Physically, torque is produced when the rotor and stator magnetic fields are spatially displaced causing the resultant air-gap field to develop a tangential component

2.3.4 dq Reference Frame Model

The d and q axis definition is illustrated in Figure 2.3.

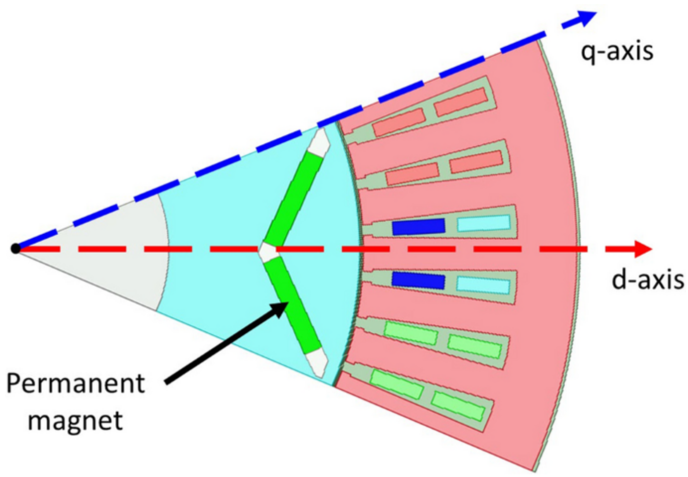

Figure 2.3: Definition of the d and q axes in a permanent magnet machine. The d axis is aligned with the rotor permanent-magnet flux direction, while the q axis is perpendicular to the d axis [7]

For control and performance analysis, the machine is described in a rotating dq reference frame. For the permanent-magnet machines considered in this thesis, the d axis is taken along the rotor direct axis, which is aligned with the rotor permanent-magnet flux direction, while the q axis is perpendicular to it. In the rotating dq reference frame, balanced sinusoidal three-phase quantities appear as constant values in steady state, which simplifies machine analysis and control design.

The d axis current component is associated with the direct-axis flux path and is commonly used for flux control, field weakening, and reluctance-torque utilization. The q axis current component is perpendicular to the magnet flux axis and is mainly responsible for torque production. Therefore, the dq model provides a convenient basis for field-oriented control because the current vector can be separated into flux-producing and torque-producing components [7].

The equivalent dq-axis circuits of a permanent-magnet synchronous machine are shown in Figure 2.4.

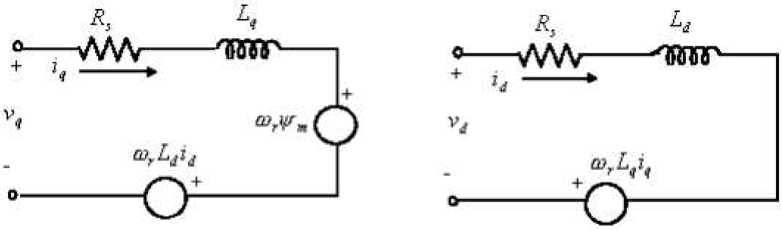

Figure 2.4: Equivalent circuits of the permanent magnet synchronous machine in the rotating dq reference frame. The d and q axis circuits include the stator resistance, d and q axis inductances, permanent magnet flux linkage and speed-dependent coupling voltage terms [8]

The circuits show the stator resistance, the d and q axis inductances, the permanent-magnet flux linkage and the speed-dependent cross-coupling voltage terms.

The stator voltage equations in the rotor-oriented dq frame are

$$v_d = R_s i_d + \frac{d\psi_d}{dt} - \omega_e \psi_q, \tag{2.22}$$

$$v_q = R_s i_q + \frac{d\psi_q}{dt} + \omega_e \psi_d, \tag{2.23}$$

where v_d and v_q are the dq-axis voltages, i_d and i_q are the dq-axis currents, ψ_d and ψ_q are the dq-axis flux linkages, R_s is the stator phase resistance, and ω_e is the electrical angular speed.

For a simplified PMSM model, the flux linkages can be written as

$$\psi_d = L_d i_d + \psi_m, \tag{2.24}$$

$$\psi_q = L_q i_q, \tag{2.25}$$

where L_d and L_q are the d and q axis inductances, respectively, and ψ_m is the permanent-magnet flux linkage. Substituting Equations (2.24) and (2.25) into the voltage equations gives

$$v_d = R_s i_d + L_d \frac{di_d}{dt} - \omega_e L_q i_q, \tag{2.26}$$

$$v_q = R_s i_q + L_q \frac{di_q}{dt} + \omega_e L_d i_d + \omega_e \psi_m. \tag{2.27}$$

Equations (2.26) and (2.27) correspond to the equivalent circuits shown in Figure 2.4. The terms $R_s i_d$ and $R_s i_q$ represent the resistive voltage drops, while $L_d di_d/dt$ and $L_q di_q/dt$ represent the inductive voltage drops. The terms $-\omega_e L_q i_q$ and $+\omega_e L_d i_d$ represent the coupling between the two axes due to the rotating reference frame. The term $\omega_e \psi_m$ in the q-axis voltage equation represents the back electromotive force associated with the permanent magnet flux linkage.

2.3.5 dq Torque Equation and Field Interaction

In a permanent magnet synchronous machine, the air-gap flux is produced by both the rotor permanent magnets and the stator current. The rotor magnets establish a flux fixed to the rotor, while the stator currents create a rotating magnetic field. Electromagnetic torque is produced when these two fields interact with a spatial phase difference.

The general electromagnetic torque expression for a sinusoidal three-phase synchronous machine can be written as

$$T_e = \frac{3}{2} p \left(\psi_d i_q - \psi_q i_d \right), \tag{2.28}$$

where p is the number of pole pairs.

Substituting (2.24) and (2.25) into (2.28) gives

$$T_e = \frac{3}{2} p \left[\psi_m i_q + (L_d - L_q) i_d i_q \right]. \tag{2.29}$$

The first term,

$$T_{\mathrm{PM}} = \frac{3}{2} p \psi_m i_q \tag{2.30}$$

is the permanent-magnet torque. It is produced by the interaction between the rotor magnet flux and the stator q axis current. This explains why i_q is very effective for torque production as it produces a stator field component orthogonal to the rotor magnet flux and therefore generates tangential electromagnetic stress.

The second term,

$$T_{\text{rel}} = \frac{3}{2}p(L_d - L_q)i_d i_q \tag{2.31}$$

is the reluctance torque. This component exists when the rotor is salient, meaning that the magnetic reluctance is different along the d and q axes. In many IPMSM and PMaSynRM designs, $L_q > L_d$, so a negative d axis current together with a positive q axis current can contribute positive reluctance torque according to (2.29).

The d axis current is not directly effective for permanent-magnet torque production because it is aligned with the rotor magnet flux. A positive or negative i_d mainly strengthens or weakens the effective air-gap flux rather than directly producing the tangential field component required for PM torque. However in salient machines i_d affects reluctance torque and is therefore important for maximum-torque-per-ampere (MTPA) operation.

2.3.6 Energy and Co-Energy Interpretation

The same torque-production mechanism can also be interpreted using magnetic energy and co-energy. The electromagnetic field stores energy and this stored energy depends on rotor position because the reluctance and the alignment between stator and rotor fields change with rotor angle. The electromagnetic torque can be expressed as

$$T_e = \left.\frac{\partial W'_m}{\partial \theta_m}\right|_{i=\text{constant}} \tag{2.32}$$

where W'_m is the magnetic co-energy and θ_m is the mechanical rotor position. This expression means that the rotor experiences torque because the electric machine tends to move toward a position that increases magnetic co-energy.

2.3.7 Voltage and Current Constraints

The operating point of a traction motor is limited by the inverter current and voltage ratings. The current limit defines the maximum allowable stator current magnitude while the voltage limit defines the maximum voltage that can be supplied by the inverter for a given DC-link voltage. These constraints are represented in the i_d-i_q plane, as shown in Figure 2.5.

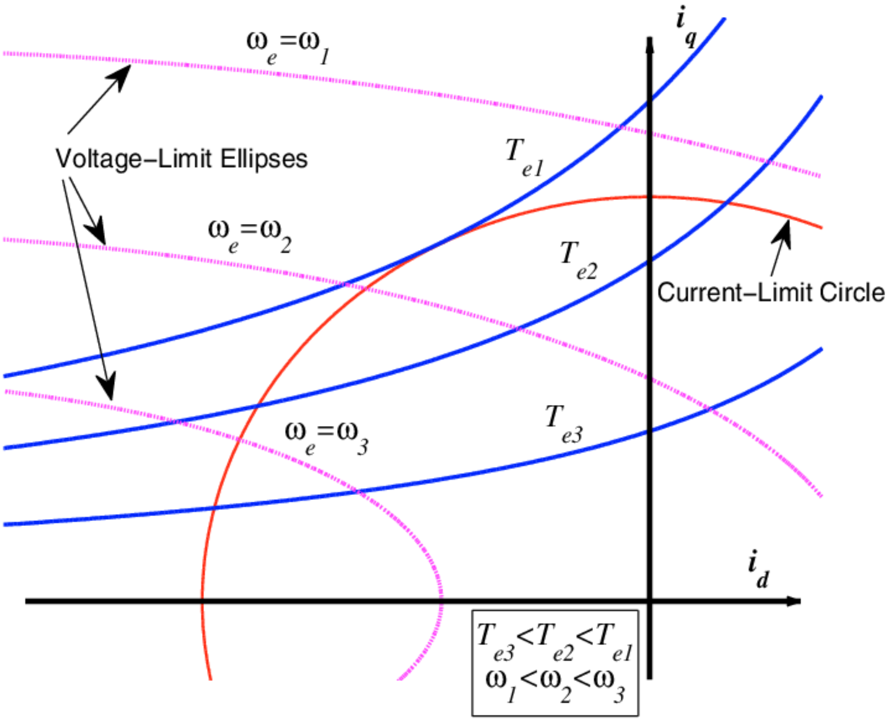

Figure 2.5: Current-limit circle, voltage-limit ellipses and constant-torque curves in the i_d-i_q plane [9]

The current limit is represented as a circle in the dq plane,

$$i_d^2 + i_q^2 \leq I_{\max}^2, \tag{2.33}$$

where $I_{\max}$ is the maximum allowable stator current magnitude. This limit is mainly determined by the inverter current rating, winding thermal limit and machine cooling capability. Any operating point outside this circle would require a current magnitude larger than the allowable value.

The voltage limit is represented as

$$v_d^2 + v_q^2 \leq V_{\max}^2, \tag{2.34}$$

where $V_{\max}$ is the maximum allowable dq voltage magnitude. If peak phase voltage is used in the dq model, the maximum fundamental voltage using PWM is

$$V_{\max} \approx \frac{V_{\mathrm{dc}}}{\sqrt{3}}. \tag{2.35}$$

From Equations (2.22) and (2.23), the voltage increases with electrical speed because of the speed-dependent terms $-\omega_e \psi_q$ and $+\omega_e \psi_d$. Therefore, as speed increases the voltage constraint becomes more restrictive. In the i_d-i_q plane, this is seen as a voltage-limit ellipse that shrinks with increasing electrical speed.

The feasible operating region is the overlap between the current-limit circle and the voltage-limit ellipse.

2.3.8 MTPA, Field-Weakening and MTPV Operation

The current reference of a permanent-magnet traction machine is selected according to the current limit, voltage limit and torque demand. These operating constraints can be represented in the i_d-i_q plane, as shown in Figure 2.6. The figure illustrates the current-limit circle, voltage-limit ellipses at different speeds, constant-torque curves and the transition between maximum-torque-per-ampere (MTPA), field-weakening (FW) and maximum-torque-per-voltage (MTPV) operation.

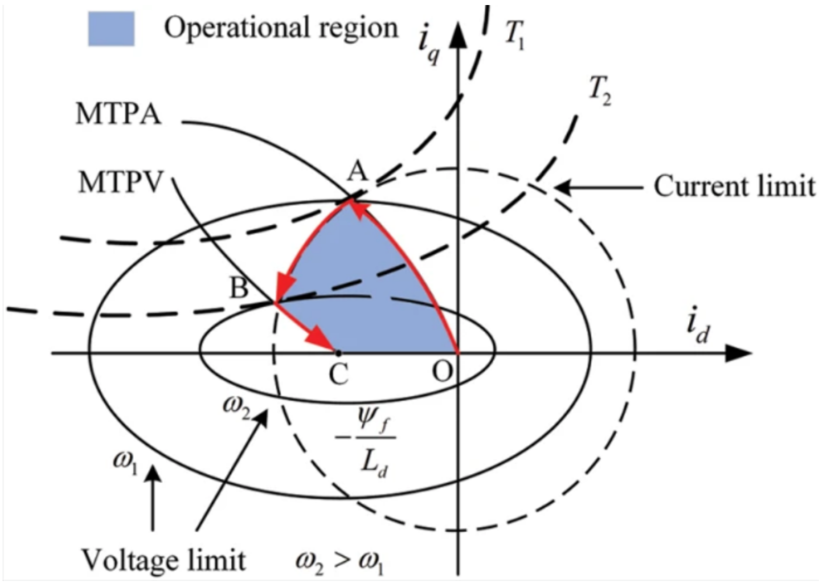

Figure 2.6: MTPA, field-weakening and MTPV operation in the i_d-i_q plane [10]

At low and medium speeds, the machine is usually current-limited rather than voltage-limited. In this region, the control objective is commonly maximum-torque-per-ampere (MTPA). MTPA selects the current vector (i_d, i_q) that produces the required torque with minimum current magnitude [10]. This reduces copper loss and improves efficiency. In Figure 2.6, this corresponds to operation along the MTPA trajectory until the voltage limit becomes active.

As speed increases the voltage required by the machine also increases because of the back-EMF terms in the dq voltage equations. When the required voltage reaches the inverter voltage limit, the machine enters the field-weakening region. In this region, negative d axis current is applied to reduce the effective d axis flux linkage and keep the voltage demand within the available DC-link voltage. Therefore the operating point moves away from the MTPA curve and follows Field Weakening (AB curve in Figure 2.6) trajectory constrained by both the current-limit circle and the voltage-limit ellipse.

At very high speed, the feasible optimum may approach the maximum-torque-per-voltage (MTPV) trajectory. In the MTPV region, the current vector is selected to maximize the achievable torque under the voltage constraint at a given speed. Depending on the machine parameters, voltage limit, current limit and maximum operating speed this region may or may not appear as a clearly separate operating region. Therefore some machines may show only MTPA and field-weakening operation within the speed range without reaching a distinct MTPV trajectory.

2.3.9 Loss Mechanisms and Efficiency Analysis

Loss and efficiency maps describe machine performance over a wide range of torque-speed operating points rather than at a single operating condition. The main loss components considered in the machine are stator copper loss, iron or core loss and permanent magnet loss. The total loss can be written as

$$P_{\mathrm{loss}} = P_{\mathrm{cu}} + P_{\mathrm{fe}} + P_{\mathrm{pm}} \tag{2.36}$$

where P_{cu} is the copper loss, P_{fe} is the iron or core loss and P_{pm} is the permanent magnet loss. Mechanical loss has not been considered in this study.
The stator copper loss is caused by winding resistance and can be estimated as

$$P_{\mathrm{cu}} = 3I_{\mathrm{rms}}^2 R_s \tag{2.37}$$

where I_{rms} is the phase RMS current and R_s is the phase resistance at a particular temperature. When high-frequency harmonics, slot leakage fluxes and inverter switching ripples are considered the effective AC winding resistance can be higher than the DC resistance due to skin and proximity effects.

The core loss P_{fe} occurs in the laminated electrical steel and is mainly caused by the alternating magnetic flux density in the stator and rotor cores. In this thesis, the Bertotti loss separation model is used in which the specific iron loss is separated into hysteresis loss, eddy-current loss and excess loss. For sinusoidal flux density with peak value B and frequency f, the specific core loss can be written as [11]

$$p_{\mathrm{fe}} = p_{\mathrm{h}} + p_{\mathrm{e}} + p_{\mathrm{exc}} \tag{2.38}$$

with

$$p_{\mathrm{h}} = k_{\mathrm{h}} f B^{\alpha}, \tag{2.39}$$

$$p_{\mathrm{e}} = k_{\mathrm{e}} f^2 B^2, \tag{2.40}$$

$$p_{\mathrm{exc}} = k_{\mathrm{exc}} f^{3/2} B^{3/2}. \tag{2.41}$$

where p_{h} is the hysteresis loss component, p_{el} is the classical eddy-current loss component and p_{exc} is the excess loss component. The coefficients k_{h}, k_{el}, and k_{exc} are material dependent coefficients obtained from the electrical steel loss data while α is the Steinmetz exponent associated with the hysteresis loss. The hysteresis loss is related to the energy dissipated during repeated magnetization of the steel. The classical eddy-current loss is caused by circulating currents induced in the laminations. The excess loss accounts for additional dynamic losses associated with non-uniform domain-wall motion and local flux-density variations.

The iron loss data used in the simulation are usually obtained from standard material tests such as Epstein-frame or single-sheet measurements. However the losses in a practical motor core can be higher than the losses predicted directly from these material data. This difference is commonly accounted for using a build factor. The build factor represents the ratio between the iron loss observed in the practical core and the iron loss predicted from standard material data:

$$k_{\text{bf}} = \frac{P_{\text{fe,practical}}}{P_{\text{fe,material}}}. \tag{2.42}$$

The build factor is used because the real motor core is affected by manufacturing and operating effects that are not fully represented in standard material test data. These effects include punching of laminations, residual mechanical stress or stacking pressure in the stator and rotor.

Permanent magnet losses are caused by time-varying magnetic fields inside the magnets. These losses can increase at high speed and when slotting harmonics, current harmonics or PWM-induced harmonics are present.

The efficiency is calculated as

$$\eta = \frac{P_{\text{out}}}{P_{\text{out}} + P_{\text{loss}}}. \tag{2.43}$$

where P_{out} is the output mechanical power.

It should be noted that the peak efficiency value alone does not fully describe the suitability of a traction machine. A traction motor operates over a wide range of torque and speed conditions and so the location and size of the high-efficiency region in the efficiency map are important. A design with a very high peak efficiency may be less attractive if this peak occurs in a rarely used operating region. For vehicle applications the high-efficiency region should coincide with the frequent operating points of the drive cycle.

2.4 Demagnetization Theory

Permanent magnets in traction machines can be exposed to severe demagnetizing fields during fault conditions and high current operation. In particular, a three-phase short circuit can produce large transient currents that oppose the magnetization direction of the magnets. If the local magnet operating point is forced beyond the irreversible demagnetization region, the magnet may not fully recover its original remanence after the fault is removed. This reduces the effective air-gap flux density and can lead to lower torque capability, poorer efficiency and degraded machine performance.

The demagnetization behaviour of a permanent magnet is commonly studied using the second quadrant of the magnetic characteristic as shown in Figure 2.7. The normal demagnetization curve describes the relation between the flux density B and the magnetic field intensity H. The intrinsic curve describes the magnetization of the permanent magnet and is directly related to irreversible demagnetization. For this reason the intrinsic curve is used in this work to evaluate whether the magnet operating point enters an irreversible demagnetization region.

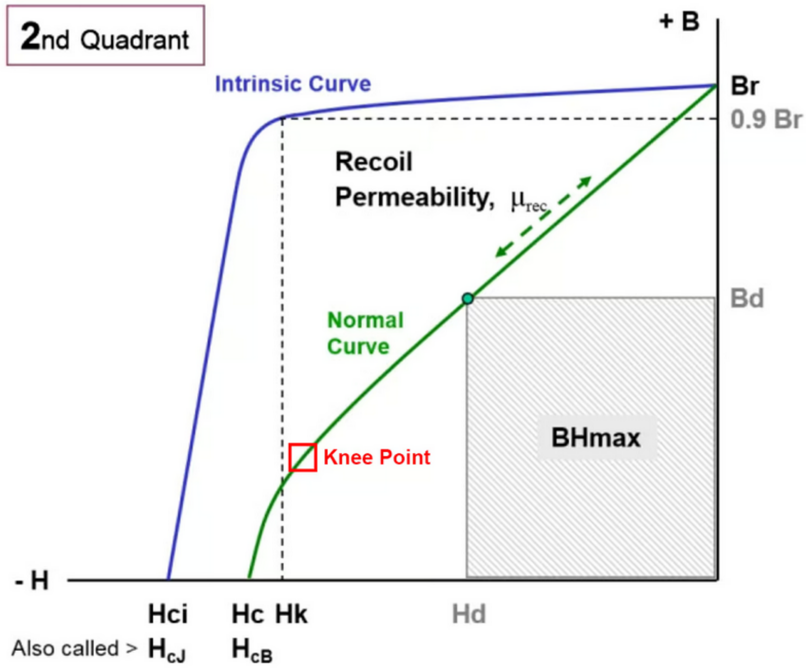

Figure 2.7: Intrinsic demagnetization curve, knee point and recoil behaviour of a permanent magnet [12].

Figure 2.7 illustrates the intrinsic demagnetization curve and the corresponding knee point. The knee point is one of the most important features of the curve because it separates the reversible operating region from the irreversible demagnetization region. If the magnet operating point remains above the knee point, the magnet strength is reversible. So when the demagnetizing field is removed, the magnet can approximately return along a recoil line without a significant permanent reduction in remanence.

However if the operating point passes below the knee point then irreversible demagnetization can occur. In this case, the magnet no longer returns to its original remanent flux density after the demagnetizing field is removed. Instead it follows a new recoil path and settles at a lower remanence. This means that the local magnet strength has been permanently reduced. The reduction in remanence decreases the magnet flux contribution which can reduce the torque capability and efficiency of the machine.

The risk of demagnetization is strongly dependent on temperature. NdFeB magnets usually become more vulnerable to irreversible demagnetization at elevated temperature because their intrinsic coercivity decreases as temperature increases. Ferrite magnets often have the opposite critical trend. Their intrinsic coercivity decreases at low temperature which can make cold conditions more severe for ferrite demagnetization.

3

Material Selection and Simulation Methodology

3.1 Traction Motor Requirements

The traction motor considered in this work is intended for a medium-duty urban distribution application based on the Volvo FL Electric vehicle class. The Volvo FL Electric is designed for applications such as door-to-door deliveries, waste collection, and city logistics, where frequent start-stop operation, high low-speed torque, and good drivability are required. Therefore, the motor must be capable of delivering high torque in the low-speed region, while also maintaining sufficient power capability in the high-speed field-weakening region.

The main motor-level design requirements used in the ANSYS Maxwell 2D electromagnetic model are given in Table 3.1 [13].

Table 3.1: Traction motor design requirements used for the electromagnetic model.

Requirement	**Value**
Vehicle application	Medium-duty urban distribution truck
Maximum motor torque	425 Nm
Maximum motor power	185 kW
Base speed at full load	4000 rpm
Maximum mechanical speed	7000 rpm
Nominal DC-link voltage	600 V
Maximum RMS phase current	300 A

The motor is required to operate in the constant-torque region up to the base speed of approximately 4000 rpm. In this region, the current limit is the dominant constraint, and the motor should be able to deliver up to 425 Nm for vehicle launch, low-speed acceleration and gradeability. The peak power of motor is 185 kW.

Above the base speed the motor enters the field-weakening region. In this region the available DC-link voltage limits the maximum phase voltage, and therefore the torque must decrease as speed increases. The control objective in this region is to maintain the output power close to the peak power capability while respecting the voltage and current limits.

3.2 Materials Used

3.2.1 Stator and Rotor Core Material

The stator and rotor cores of the electric machines were modelled using M19-29G electrical steel. This material corresponds is a fully processed non-oriented electrical steel with a 29 gauge lamination thickness ofapproximately 0.356 mm. M-19 refers to the AISI electrical-steel grade designation, where the M-number is the magnetic grade, while 29G indicates the 29 gauge lamination thickness [14] [15].

M19-29G was selected as it is a well-documented core material rather than as the result of a complete electrical-steel grade optimization. It is a standard non-oriented electrical steel with available magnetic characterization data, including B-H curve and core loss information. This is important because the electromagnetic performance of the machine depends strongly on the nonlinear saturation behaviour of the stator teeth, stator yoke, rotor ribs and rotor bridges.

The material is fully processed, meaning that the required magnetic properties are already developed by the manufacturer. So the material can be used directly for laminated core production without requiring a final annealing process to develop the magnetic quality.

Table 3.2: Main properties of M19-29G electrical steel used in the electromagnetic model [14] [15].

Parameter	Value
Material designation	M19-29G
Material type	Non-oriented electrical steel
Processing condition	Fully processed
Lamination thickness	0.356 mm
Density	7650 kg/m^3
Core Loss	3.42 W/kg at 1.5 T and 60 Hz

M19-29G is non-oriented which means that its magnetic properties are approximately uniform in different directions in the plane of the lamination. This is suitable for rotating electrical machines because the magnetic flux direction changes around the stator teeth, stator yoke, rotor core and rotor bridges. Unlike non-oriented steel, grain oriented electrical steel is optimized mainly along the rolling direction and is therefore more suitable for transformer cores, where the flux direction is nearly fixed. In a PMSM or PMaSynRM, using grain-oriented steel would only benefit regions where the local flux happens to align with the rolling direction while other regions could experience poorer magnetic properties and increased anisotropy. For this reason non-oriented electrical steel is preferred for the present electric machine application.

Other electrical steel grades could also be considered, for example, thinner or more advanced high-frequency motor steels can reduce iron losses, especially at high speed. However comparing such materials would require a separate material optimization study including loss data, saturation behaviour, manufacturability, cost, temperature effects and availability. Since the main objective of this work is to compare motor topologies and magnet configurations, the same M19-29G material was used consistently for all investigated designs. This allows the comparison to focus on rotor topology, torque production, saturation behaviour and torque ripple rather than on electrical-steel grade selection.

The nonlinear B-H curve of M19-29G used is shown in Fig. 3.1.

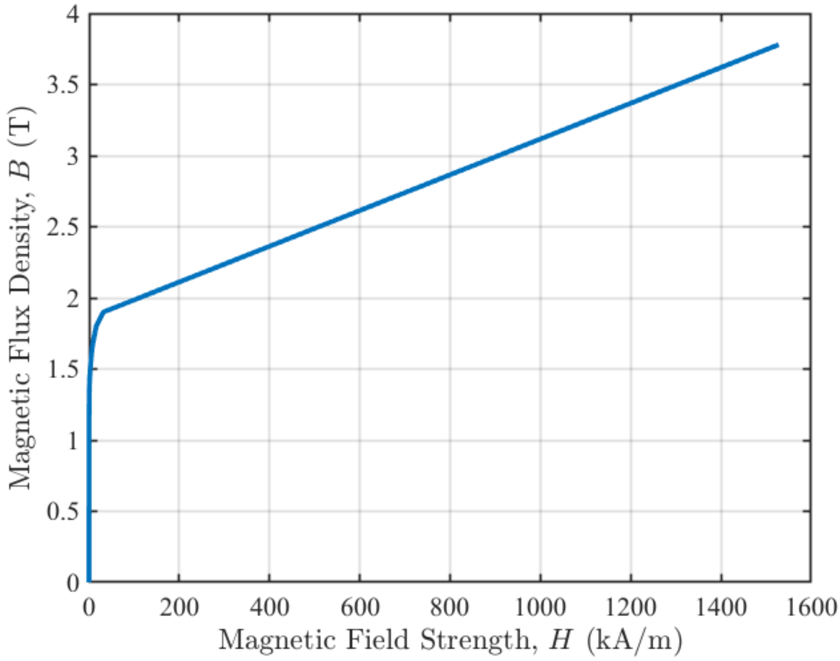

Figure 3.1: Normal B-H magnetization curve of M19-29G electrical steel used for the stator and rotor core material.

3.2.2 Magnet Material

The PMaSynRM uses two permanent magnet materials: FB13B ferrite magnets from TDK [16] and N42SH NdFeB magnets from Arnold Magnetic Technologies [17] where the high flux density NdFeB magnets provide strong magnetic flux while the ferrite magnets reduce the dependency on NdFeB material and contribute additional air-gap flux. Spoke PMSM, meanwhile, uses only the Ferrite Magnets to provide all the air-gap flux.

Unlike the electrical steel used in the stator and rotor core, permanent magnets are not described using a first-quadrant magnetization curve. Instead, their operating behaviour is represented using second-quadrant demagnetization curves. These curves describe the relationship between the magnet flux density and the demagnetizing field acting on the magnet.

The residual flux density B_r describes the flux density remaining in the magnet when the applied magnetic field is zero. The coercive force H_{cB} indicates the demagnetizing field required to reduce the magnetic flux density B to zero. The intrinsic coercive force H_{cJ} describes the resistance of the magnet to irreversible demagnetization. The maximum energy product $(BH)_{\max}$ is a measure of the magnetic energy density that the magnet can supply to the external magnetic circuit. A higher value of $(BH)_{\max}$ indicates that a smaller magnet volume can produce high magnetic loading.

3.2.2.1 FB13B Ferrite Magnet

FB13B is a high-performance La-Co ferrite magnet material. Compared with NdFeB, the residual flux density and maximum energy product are lower, but ferrite magnets are attractive because of their lower cost, high temperature stability and reduced dependence on rare-earth NdFeB material. The second-quadrant demagnetization curves of FB13B are shown in Fig. 3.2.

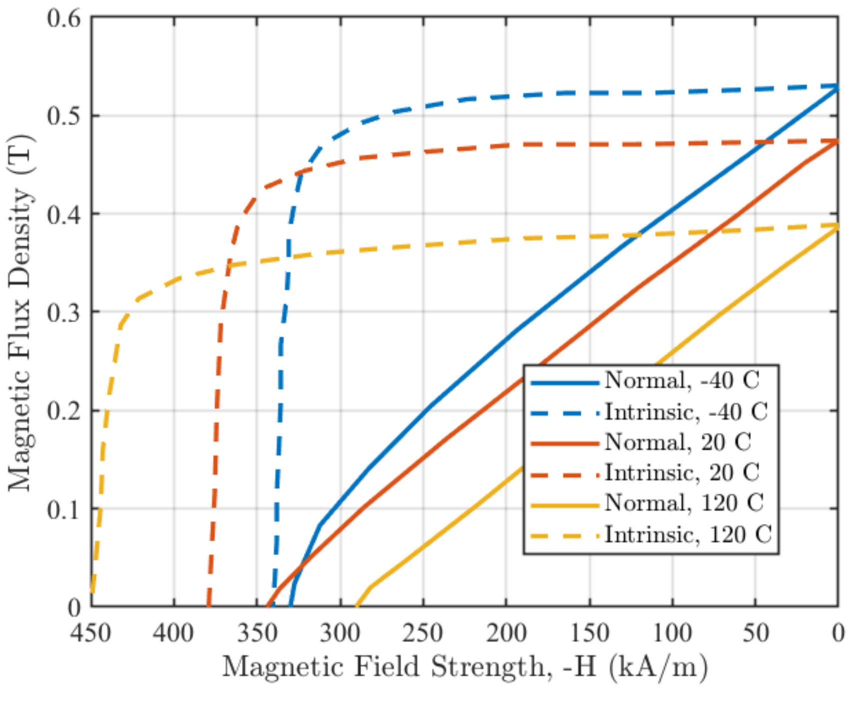

Figure 3.2: Second-quadrant demagnetization curves of the TDK FB13B ferrite magnet material.

3.2.2.2 N42SH NdFeB Magnet

N42SH is a sintered neodymium-iron-boron magnet material. It has a much larger residual flux density and maximum energy product than FB13B which makes it suitable for increasing the air-gap flux and torque density of the machine.

The "SH" temperature grade indicates that the material is intended for high temperature operation compared with the standard NdFeB grades. The second-quadrant demagnetization curves of N42SH are shown in Fig. 3.3.

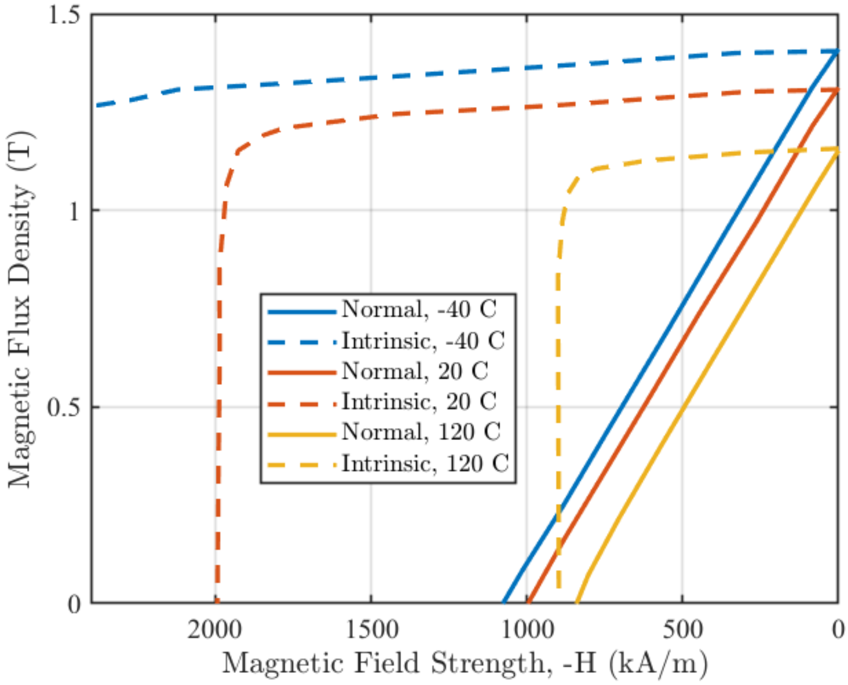

Figure 3.3: Second-quadrant demagnetization curves of the Arnold Magnetic Technologies N42SH NdFeB magnet material.

3.2.2.3 Magnet Material Properties

The main material properties of the two permanent magnets are given in Table 3.3. The values are taken from the manufacturer datasheets.

Table 3.3: Material properties of FB13B ferrite and N42SH NdFeB permanent magnets [16] [17].

Property	**TDK FB13B**	**Arnold N42SH**
Magnet type	Ferrite magnet	Sintered NdFeB magnet
Material description	High-power La-Co ferrite	Neodymium-iron-boron, high temperature grade
Residual flux density, B_r	475 ± 10 mT	1280-1340 mT, nominal 1310 mT
Coercive force, H_{cB}	340 ± 20 kA/m	955-1019 kA/m, nominal 987 kA/m
Intrinsic coercive force, H_{cJ}	380 ± 20 kA/m	Minimum 1592 kA/m
Maximum energy product, $(BH)_{\max}$	44.0 ± 1.6 kJ/m^3	310-350 kJ/m^3, nominal 330 kJ/m^3

3.2.3 Stator Winding Material

The stator winding was modelled using copper litz wire with an individual wire diameter of 0.4 mm. The winding material and conductor type were selected based on electrical conductivity, thermal performance, and the need to reduce AC winding losses caused by high-frequency current components.

Copper was selected instead of aluminium because copper has a significantly higher electrical conductivity [18]. Aluminium has only about 61% of the electrical conductivity of copper meaning that a larger aluminium cross-sectional area is required to obtain the same resistance. In a traction motor, the stator slot area is limited by the electromagnetic design, insulation requirements, cooling and mechanical constraints. Therefore using copper allows lower winding resistance and lower copper loss for a given slot area [18].

A litz wire was selected instead of a round wire to reduce AC winding losses. Litz wire consists of many thin, individually insulated copper strands connected electrically in parallel. These strands are twisted or transposed along the length of the conductor so that each strand occupies different positions within the bundle. This arrangement helps distribute the current more uniformly among the strands and reduces the effects of skin effect and proximity effect. Skin effect causes AC current to concentrate near the surface of a conductor, while proximity effect is caused by the magnetic fields of neighbouring conductors, which distort the current distribution inside the wire. Both effects increase the effective AC resistance of the winding. By using many small insulated strands litz wire reduces these high-frequency losses compared with an equivalent solid round conductor [19].

The skin depth is the depth below the conductor surface at which the AC current density has decreased to approximately $1/e$ of its surface value. For a conductor such as copper, the skin depth is given by [20]

$$\delta = \sqrt{\frac{\rho}{\pi f \mu}}, \tag{3.1}$$

where ρ is the electrical resistivity of copper, f is the current frequency, and μ is the absolute permeability of copper. The skin depth decreases as frequency increases meaning that high-frequency current harmonics affect skin effect more than the fundamental current.

The electrical frequency of the motor is

$$f_e = p\frac{n_m}{60}, \tag{3.2}$$

where p is the number of pole pairs and n_m is the mechanical speed in rpm. For the electric machine with $p = 4$ at the maximum speed of 7000 rpm,

$$f_e = 4\frac{7000}{60} \approx 467\,\text{Hz}. \tag{3.3}$$

Since 11th and 13th current harmonics are injected in the abc frame, the corresponding harmonic frequencies at maximum speed are

$$f_{11} = 11f_e \approx 5133\,\text{Hz}, \tag{3.4}$$

$$f_{13} = 13f_e \approx 6067\,\text{Hz}. \tag{3.5}$$

Using the copper resistivity at room temperature, $\rho \approx 1.724 \times 10^{-8}$ Ωm, the estimated skin depths are

$$\delta_{11} \approx 0.92\,\text{mm}, \tag{3.6}$$

$$\delta_{13} \approx 0.85\,\text{mm}. \tag{3.7}$$

The selected copper wire diameter is

$$d_{\text{wire}} = 0.4\,\text{mm}. \tag{3.8}$$

Therefore,

$$d_{\text{wire}} < \delta_{13} < \delta_{11}. \tag{3.9}$$

This shows that the selected 0.4 mm copper wire diameter is smaller than the skin depth even at the 13th harmonic frequency at maximum speed. Therefore, the current distribution within each strand is expected to remain relatively uniform and the skin-effect loss inside an individual strand is limited. This makes copper litz wire a suitable choice for the winding especially because the motor uses high RMS phase current and additional harmonic current injection for torque ripple reduction.

Although the selected strand diameter is smaller than the skin depth at the considered harmonic frequencies this only confirms that skin effect within each individual strand is limited. However, the total AC winding loss in the stator can still increase due to proximity effect, where time-varying magnetic fields from neighbouring conductors, slot leakage flux and other strands distort the current distribution. In addition, conductor packing, strand transposition quality, temperature-dependent copper resistance and inverter PWM-induced current harmonics can further influence the effective AC resistance of the winding. Therefore, the benefit of litz wire is not only that each strand is sufficiently small with respect to the skin depth, but also that the strands are individually insulated and transposed along the conductor length. This construction helps the strands experience similar average electromagnetic conditions, promotes a more uniform current distribution and reduces both skin-effect and proximity-effect losses compared with a round conductor.

3.3 Finite-Element Simulation Procedure

The electromagnetic performance of the machine was evaluated using a transient solver in ANSYS Maxwell 2D. The transient magnetic solver was selected because it computes the time-varying magnetic field in the time domain and solves for the instantaneous field solution at each time step. This is suitable for rotating electrical machines where the magnetic field varies due to rotor, permanent magnets and time-varying current excitation.

Fig. 3.4 illustrates an example of a 1/8th reduced model in Ansys Maxwell 2D

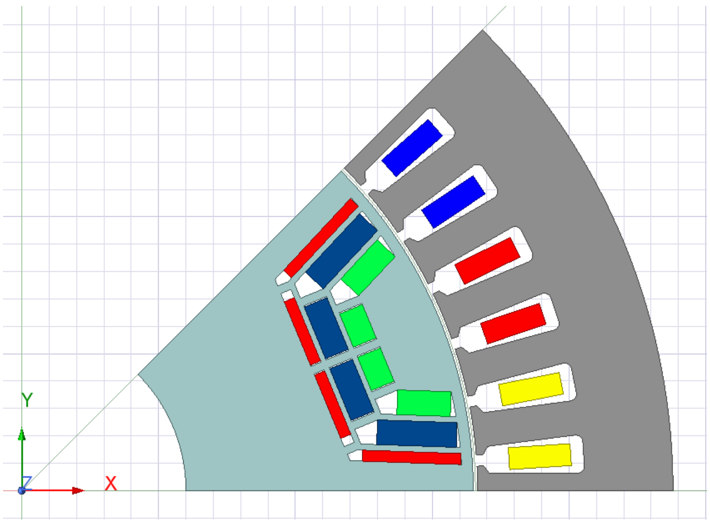

Figure 3.4: An example of 1/8th Reduced Model used to save computational resources by taking advantage of symmetry

To reduce the computational cost, only one-eighth of the complete machine geometry was modelled as shown in Fig. 3.4. This reduction was possible due to the geometric and magnetic periodicity of the machine. Anti-periodic boundary conditions were applied on the two radial symmetry boundaries so that the field solution in the modelled sector correctly represents the corresponding repeated sectors of the full machine.

The refined mesh in the air gap is shown in Fig. 3.5.

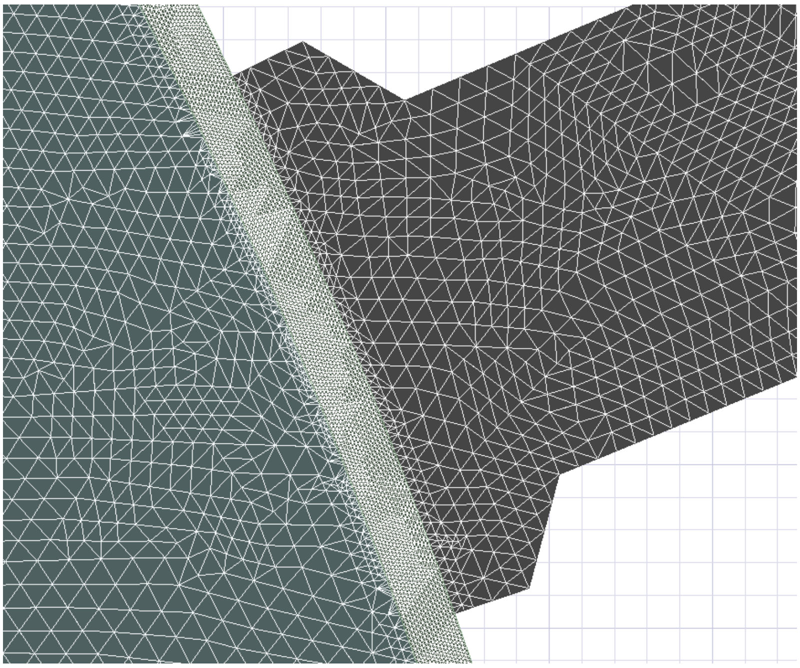

Figure 3.5: Refined Mesh in the Air Gap for determining accurate torque ripple

The mesh was refined using an inside-selection length-based mesh operation. A maximum element size of 0.5 mm was assigned to the main active electromagnetic regions, including the rotor, stator, air gap, coils, and permanent magnets. The air-gap region was refined carefully because the air-gap field distribution strongly influences torque production, torque ripple, and force calculation accuracy.

The torque-speed operating grid used for loss and efficiency mapping is shown in Fig. 3.6.

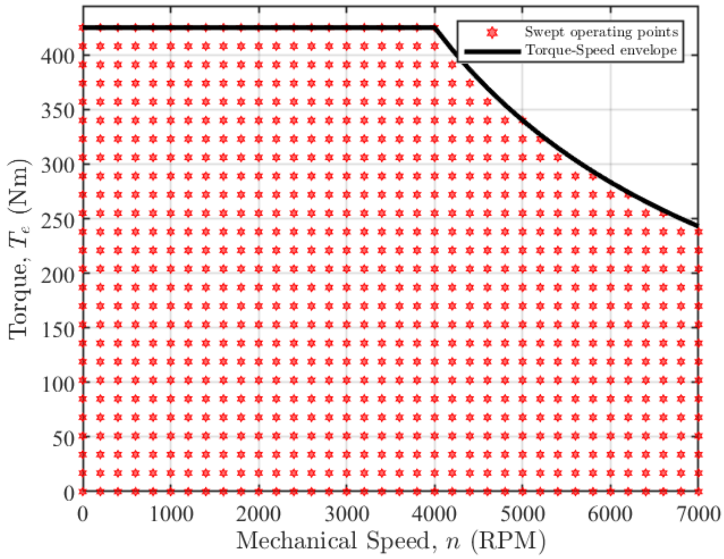

Figure 3.6: Torque-Speed operating grid used for loss and efficiency mapping

For generating the grid as shown in Fig. 3.6, a transient simulation was carried out at a constant mechanical speed of 1000 rpm. The current operating points were defined in the rotor *dq* reference frame. The *d*-axis current was swept from −450 A to 0 A, and the *q*-axis current was swept from 0 A to 450 A, both with a step size of 75 A. This resulted in 7 x 7 = 49 different current operating points. For each operating point, transient quantities such as torque, flux density, losses and efficiency-related data were extracted from the Maxwell solution.

The simulation results obtained at 1000 rpm were then used as the base electromagnetic data for post-processing over the required torque-speed operating range. The operating grid was defined from 0 to 7000 rpm in steps of 10 rpm and from 0 to 425 Nm in steps of 10 Nm. In the constant-torque region, operating points up to 425 Nm were considered. Above the base speed of 4000 rpm, the maximum allowable torque was reduced according to the field-weakening torque-speed envelope.

It should be noted that this approach represents a post-processing extension of the simulation data rather than a direct Maxwell simulation at every torque-speed point. Therefore the scaled loss and efficiency results should be interpreted as estimates based on the available current sweep data and the assumed speed-dependent scaling procedure.

3.4 Driving Cycle and Driveline Simulation Setup

3.4.1 Selection of Driving Cycles

To evaluate the traction system under different operating conditions, two custom driving cycles were developed in this work: a city driving cycle and a highway driving cycle. Custom driving cycles were preferred over standard driving cycles like NEDC or WLTC because the vehicle considered in this thesis is a medium-duty electric truck with a limited top speed of approximately 90 km/h. Many standard drive cycles contain speed ranges above this value and will place the vehicle in operating regions which are not possible to reach. To maintain consistency with the top speed capability of the vehicle, the speed range in the simulation was restricted accordingly.

3.4.2 Description of the Driving Cycles

The velocity and acceleration profiles of the two custom driving cycles are shown in Figures 3.7 and 3.8. For each driving cycle, the velocity profile is shown on the left and the corresponding acceleration profile is shown on the right.

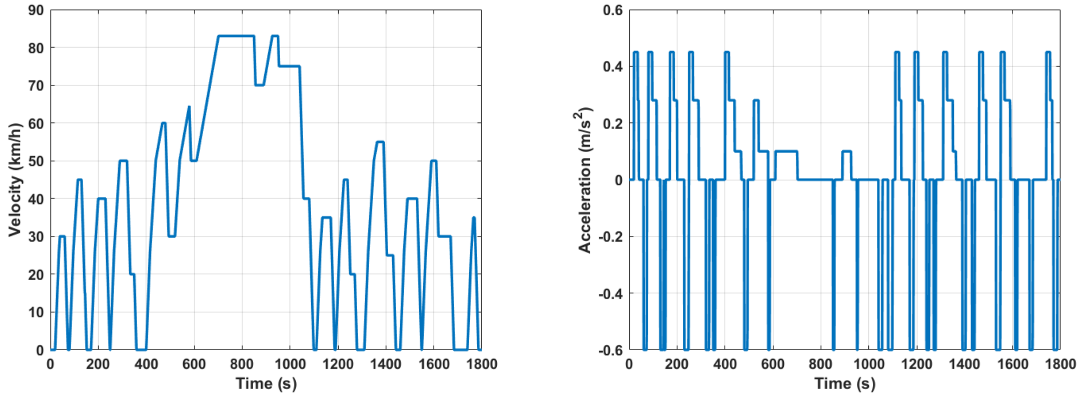

Figure 3.7: Velocity and Acceleration profiles of the custom city driving cycle

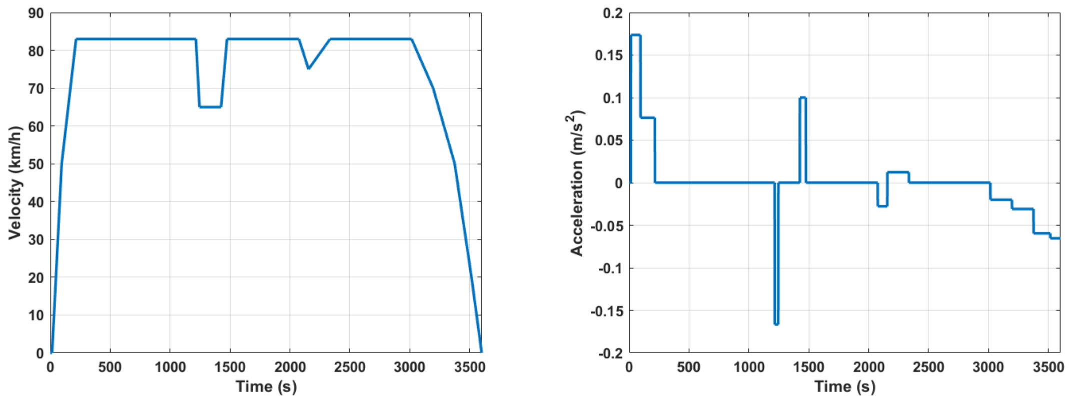

Figure 3.8: Velocity and Acceleration profiles of the custom highway driving cycle

The two custom cycles were selected to represent two distinct operating scenarios. The city cycle represents urban delivery operation where the vehicle is subjected to frequent start-stop events, repeated acceleration and braking and low average speed. It is therefore useful for evaluating low speed tractive effort, regenerative braking behaviour and the suitability of the lower gear ratio. The highway cycle meanwhile represents operation with longer periods of nearly constant cruising speed with occasional braking and acceleration. This cycle is more suitable for evaluating higher-speed efficiency, driveline behaviour in the upper gear and the ability of the traction motor to operate efficiently over cruising interval. The road gradient plots and the gear selection plots are shown in Figure A.1 and A.2 of Appendix A respectively.

3.4.3 Vehicle, Driveline and Regeneration Parameters

The main parameters used in the driving-cycle simulation are summarized in Table 3.4.

Table 3.4: Main parameters used in the driving-cycle simulation.

Parameter	**Value**
Vehicle mass, m	16 000 kg
Drag coefficient, C_d	0.6
Frontal area, A_f	6.5 m^2
Rolling resistance coefficient, C_{rr}	0.008
Vehicle top speed	83 km/h
Tire size	285/70 R19.5
Gearbox efficiency, η_{gear}	0.97
Maximum regenerative power, $P_{\text{regen,max}}$	100 kW
Zero-regen speed threshold	3 km/h
Full-regen speed threshold	8 km/h
First gear ratio	22.0
Second gear ratio	14.2
Upshift speed	25 km/h
Downshift speed	8 km/h

The vehicle parameters define the road-load model used in the simulation. The vehicle mass, aerodynamic drag coefficient, frontal area and rolling resistance coefficient determine the tractive effort required to follow the speed and acceleration profile.

The driveline was modeled using a constant gearbox efficiency of 0.97. Since the Volvo FL Electric uses a two-speed gearbox, a two-speed transmission was also adopted in the thesis. The selected overall gear ratios were 22.0 in first gear and 14.2 in second gear.

3.4.4 Justification of the Selected Gear Ratios

The selected gear ratios were chosen as reasonable values for a medium-duty electric truck and to provide a suitable compromise between launch performance, gradeability and cruising operation.

The first gear ratio of 22.0 is relatively high and therefore provides strong torque multiplication at the wheels. This is beneficial during vehicle launch, low-speed acceleration, hill-start conditions and the start-stop nature of city driving.

The second gear ratio of 14.2 is lower and is therefore more suitable for medium and high-speed operation. By reducing the overall ratio the motor speed for a given vehicle speed is also reduced. This is beneficial as it helps to limit excessive motor speed, reduces driveline losses during cruising and enables the machine to operate in a more efficient region during highway-type operation. The ratio spread between the two gears is also moderate which is desirable for smooth shifting and to avoid an excessively large speed or torque step during a gear change.

3.4.5 Shift Strategy and Regenerative Braking Assumptions

A simple two-speed gear upshift and downshift logic was implemented for the simulation. During motoring operation, the transmission shifts from first gear to second gear above 25 km/h and downshifts from second gear to first gear below 8 km/h. The use of distinct upshift and downshift thresholds introduces a hysteresis effect which helps to avoid frequent gear hunting when the vehicle operates close to the switching speed.

Regenerative braking was also included in the model in order to make the simulation more realistic. The regenerative mechanical power at the machine shaft was limited to 100 kW. Also regeneration was forced to zero below 3 km/h since electric machines are generally less effective at very low speed and friction brakes must eventually complete the stop. Above 8 km/h full regenerative braking capability was allowed. Between these two thresholds the regenerative contribution was progressively introduced. Any remaining braking demand that could not be supplied by the electric machine was assumed to be handled by the mechanical friction brakes.

4

Electric Machine Design and Analysis

4.1 Common Machine Topology and Winding Selection

The objective of this thesis is to design, analyse and compare three traction machine concepts: a hybrid-magnet PM-assisted synchronous reluctance machine (PMaSynRM), a ferrite-magnet spoke-type PMSM and an NdFeB interior PMSM used as a reference machine. Since the purpose is to compare the effect of rotor topology and magnet material, a common stator and winding platform was used for all three machines. This allows the performance differences to be mainly attributed to the rotor structure, magnet arrangement, saliency, flux concentration, and magnet material rather than to differences in slot number, pole number, or winding layout.

4.1.1 Comparison-Oriented Design Philosophy

In a fully optimized design study, each machine topology could have its own optimal pole number, slot-pole combination, winding type and rotor geometry. For example, previous studies indicate that lower pole-number PMaSynRMs like a 6 pole PMaSynRM or higher pole-number Spoke PMSM like a 10 pole Spoke PMSM can be attractive for high torque and power density [21] [22] [23]. Spoke-type ferrite PMSMs often benefit from flux-concentrating rotor structures and suitable fractional-slot combinations. Similarly double-layer and fractional-slot windings are often used to reduce torque ripple and improve the harmonic content of the air-gap field.

However using a different stator and winding layout for each machine would make the comparison less direct. If one machine used a 6-pole winding, another used a 10-pole fractional-slot winding and the reference PMSM used an 8-pole distributed winding then the resulting performance difference would include not only the effect of rotor topology and magnet material, but also the effect of pole number, winding factor, electrical frequency and slot-pole interaction. Therefore the machines in this work were designed using the same basic stator and winding configuration with the same number of poles.

The common platform used in this thesis is a three-phase, 48-slot, 8-pole, single-layer distributed winding. This choice is not claimed to be the individual optimum for every topology. Instead it is selected as a controlled baseline for fair comparison. The same current limit, voltage limit, speed range, stator geometry and winding arrangement are applied to all three designs so that the comparison focuses primarily on the electromagnetic behaviour of the rotor and magnet.

4.1.2 Justification of the 48-Slot, 8-Pole Integer-Slot Winding

For the selected stator and pole number, the number of slots per pole per phase is

$$q = \frac{S}{mP} = \frac{48}{3 \times 8} = 2 \tag{4.1}$$

where S is the number of stator slots, m is the number of phases, and P is the number of poles. Since $q = 2$ is an integer, the selected winding is an integer-slot winding.

An integer-slot winding was selected because it provides a conventional and balanced three-phase winding layout. This is useful for a comparative design study because the winding can be kept identical for all three machines. The 48-slot, 8-pole combination is also a well-established traction motor baseline and has been used in several EV and HEV machine studies. It gives two slots per pole per phase and can provide a high fundamental winding factor when properly arranged.

The use of an integer-slot winding is therefore justified by the objective of the study. Although fractional-slot combinations can be attractive for reducing cogging torque and torque ripple, they would decrease average torque in most cases and also introduce a different harmonic spectrum and a different slot-pole interaction [24]. Since torque ripple and losses are strongly affected by the winding harmonics, using different slot-pole combinations for different machines would make the comparison less transparent. For this reason the integer-slot layout was kept constant for all machines.

4.1.3 Justification of Distributed Winding

A distributed winding was selected instead of a concentrated winding. In a distributed winding each phase is spread over multiple slots, producing a more sinusoidal air-gap MMF distribution than concentrated winding arrangements. This is beneficial for traction machines because a smoother MMF distribution can reduce harmonics, back-EMF distortion, torque ripple, iron loss, magnet eddy-current loss and NVH-related excitation.

Concentrated windings also have important advantages. They can have shorter end-windings, simpler manufacturing, improved modularity and good fault-tolerant characteristics. However, concentrated windings results in a wider harmonic spectrum. These harmonics can increase core losses, magnet losses, torque ripple and acoustic noise. Since the present application is a traction motor for a medium-duty vehicle, smooth torque production and low harmonic excitation are important, so a distributed winding was considered a suitable choice for the common comparison platform.

By using the same distributed winding for the hybrid PMaSynRM, ferrite spoke PMSM and NdFeB VPMSM, the influence of the winding harmonic spectrum is kept consistent. As a result, the comparison between the three machines is more focused on rotor topology, magnet material and flux production mechanism.

4.1.4 Justification of Single-Layer Winding

A single-layer winding was selected for the common stator platform. In a single-layer winding each stator slot contains one coil side. This gives a simple winding arrangement and is superior when the objective is to obtain a high-torque baseline with good slot utilisation or fill factor. For the present study the single-layer winding was also chosen because it keeps the winding layout simple and identical across all three motor designs.

Double-layer windings can reduce torque ripple and improve the symmetry of radial forces in many slot-pole combinations [24]. This is because double-layer arrangements often produce a more favourable MMF distribution and reduce harmonics. However double-layer windings introduces additional design variables such as coil pitch, layer arrangement and end-winding geometry which can make comparison of topologies more complicated. In many designs, the reduction in torque ripple also leads to a slight decrease in average torque.

Therefore, the single-layer winding should not be interpreted as the globally optimal winding for all three machines. Instead it is used as a consistent baseline. The main aim of the thesis is to compare the three rotor concepts under the same electromagnetic constraints. Winding optimization including comparison with double-layer, fractional-slot or concentrated windings is therefore left as a possible future work.

4.1.5 Limitations of the Common Baseline

The main limitation of using a common 48-slot, 8-pole winding is that each motor may not be individually optimized. A 6-pole PMaSynRM or a 10-pole spoke-type PMSM may perform better if each topology is optimized separately. Similarly double-layer or fractional-slot windings may reduce torque ripple compared with the selected single-layer integer-slot winding.

However, the purpose of this thesis is not to find the absolute best possible version of each machine topology. The purpose is to compare different motor concepts under common design constraints. Therefore the selected winding and slot-pole combination represent a fair comparison platform rather than an individual optimum for each topology.

4.2 Preliminary Rotor Diameter Study

The initial design objective was to use the same rotor diameter for all three machines in order to obtain a consistent comparison. This would allow the influence of rotor topology and magnet material to be studied under similar dimensional constraints. However during the preliminary design stage it became clear that using the same rotor diameter for all three topologies was not equally practical.

Before selecting the final geometries three rotor diameter cases were studied for the NdFeB VPMSM and the hybrid-magnet PMaSynRM. These cases are referred to as the small, intermediate and large rotor diameter cases. For each case the VPMSM and PMaSynRM were designed using the same rotor diameter. This was done to keep the comparison between these two machines fair and to evaluate whether the PMaSynRM could reduce NdFeB magnet usage while maintaining a reasonable active volume.

The purpose of this preliminary study was not to fully optimize each design but to identify a suitable rotor diameter range before the detailed rotor geometry optimization. The selected diameter should provide a good compromise between NdFeB magnet reduction, rotor volume and torque.

Table 4.1 compares the NdFeB magnet volume required by the VPMSM and PMaSynRM for the three rotor diameter cases.

Table 4.1: NdFeB magnet volume comparison for the preliminary rotor diameter study.

Case	**Rotor Diameter (mm)**	**VPMSM NdFeB Vol.** (cm^3)	**PMaSynRM NdFeB Vol.** (cm^3)	**NdFeB Reduction (%)**
Small diameter	140.8	53.55	47.09	12.06
Intermediate diameter	165.0	49.35	30.40	38.40
Large diameter	195.0	46.26	27.57	40.40

From Table 4.1 it can be seen that the NdFeB volume required by the PMaSynRM decreases significantly as the rotor diameter increases from the small to the intermediate case. In the small diameter case the PMaSynRM reduces the NdFeB volume by only about 12.06% compared with VPMSM. This indicates that the smaller rotor diameter does not provide enough geometrical freedom to fully exploit the hybrid PMaSynRM saliency.

When the rotor diameter is increased to the intermediate value, the NdFeB reduction increases to 38.40% which is a good improvement. The larger rotor diameter provides more space for arranging the flux barriers and Ferrite magnets which improves the ability of the PMaSynRM to produce reluctance torque and to use the permanent magnets more effectively.

For the large diameter case the NdFeB reduction increases only slightly from 38.40% to 40.40%. Therefore, most of the magnet saving benefit is already achieved at the intermediate diameter. The additional increase in rotor diameter does not produce a proportional improvement in NdFeB reduction.

Table 4.2 compares the rotor volume of the VPMSM and PMaSynRM for the same three rotor diameter cases.

Table 4.2: Rotor volume comparison for the preliminary rotor diameter study.

Case	**Rotor Diameter (mm)**	**VPMSM Rotor Vol.** (cm^3)	**PMaSynRM Rotor Vol.** (cm^3)	**Rotor Vol. increase** (%)
Small diameter	140.8	272.479	342.541	25.71
Intermediate diameter	165.0	374.193	534.562	42.86
Large diameter	195.0	433.039	657.024	51.72

Table 4.2 shows that the PMaSynRM requires a larger rotor volume than the VPMSM for all three diameter cases. This is expected because the PMaSynRM contains flux barriers and a hybrid magnet arrangement (not fully NdFeB) and so requires more rotor space to produce sufficient torque and power.

The small diameter case has the lowest rotor volume but it gives only a small NdFeB reduction. Therefore although it is compact it does not fully satisfy the main motivation of the PMaSynRM design which is to reduce rare-earth magnet usage. The large diameter case gives the highest NdFeB reduction but this improvement is small compared with the intermediate case. At the same time the rotor volume increase becomes much larger reaching 51.72% relative to the VPMSM. This makes the large diameter design less attractive.

The intermediate rotor diameter therefore gives the best compromise. It provides a large NdFeB reduction of 38.40%, while avoiding the excessive rotor volume of the large diameter design. The intermediate case also provides more geometrical freedom than the small diameter case allowing better placement of the flux barriers and magnets. This can improve the saliency of the rotor and increase the reluctance torque contribution which is one of the main advantages of the PMaSynRM topology.

Based on this preliminary study the intermediate rotor diameter was selected for the final VPMSM and PMaSynRM designs.

The same rotor diameter was also initially considered for the ferrite spoke PMSM. However this resulted in an impractical design because the ferrite spoke machine required a very long axial length (increased rotor imbalance) and very thick ferrite magnets (increased saturation) to meet the torque requirement. This is mainly due to the lower remanent flux density of ferrite magnets compared with NdFeB magnets. Although the spoke-type topology improves the utilization of ferrite magnets through flux concentration, a larger rotor diameter was still required to obtain a practical design with acceptable axial length and magnet thickness.

Therefore the ferrite spoke PMSM was allowed to use a larger rotor diameter than the VPMSM and PMaSynRM. This design decision is a practical requirement for making the heavy rare-earth element free ferrite spoke topology feasible for the specified traction application. In the final comparison both absolute performance and normalized quantities such as torque density, power density, magnet volume, rotor volume, and drive cycle energy consumption are therefore considered.

4.3 Rotor Geometry Optimization

4.3.1 Optimization Method

After the preliminary rotor diameter study each machine topology was further optimized by varying selected rotor geometrical parameters. The optimization was carried out separately for the hybrid-magnet PMaSynRM, the ferrite spoke PMSM, and the NdFeB VPMSM reference machine. This was done because each topology has a different rotor structure and therefore requires different geometrical parameters to be adjusted.

The optimization was performed in Ansys Maxwell 2D using the Screening and Optimization tool under parametric sweep. The Screening (Search-based) optimizer was selected in order to explore different designs with limited number of design variations. For each machine a total of 100 geometrical samples were evaluated. Each sample corresponds to a different combination of the selected rotor design variables.

The optimization was carried out at the operating point $(i_d, i_q) = (-100A, 200A)$. This operating point was selected because it represents an intermediate loading condition. For the considered electric truck application, the machine is not expected to operate continuously at peak torque or in the extreme field-weakening region. Therefore optimizing the rotor geometry at an intermediate operating point was considered practical and realistic.

The cost function used for the optimization was defined as

$$J = \frac{T_{\max} - T_{\min}}{T_{\text{avg}}^2}, \tag{4.2}$$

where $T_{\max}$ is the maximum torque over one electrical period, $T_{\min}$ is the minimum torque, and T_{avg} is the average torque. The numerator represents the peak-to-peak torque ripple, while the squared average torque in the denominator penalizes designs with lower average torque. So minimizing this cost function favours designs that produce low torque ripple while also maintaining high average torque.

The optimized sample was selected as the sample with the minimum value of the cost function. After the best sample was identified, the corresponding geometrical parameters were used to update the final motor design.

The geometrical parameters varied during the optimization are given in Table 4.3.

Table 4.3: Rotor geometrical parameters considered during optimization.

Machine topology	Optimized rotor geometrical parameters
Hybrid-magnet PMaSynRM	Flux-Barrier Width, Flux-Barrier Angle, Ferrite Magnet Thickness, NdFeB Magnet Thickness, Rotor Rib Thickness, Ferrite Magnet Width, NdFeB Magnet Width, Center and Side Post Thickness
Ferrite spoke PMSM	Ferrite Magnet Thickness, Ferrite Magnet Width, Rotor Bridge Thickness, air-pocket width
NdFeB VPMSM reference	V-angle of the magnet pair, NdFeB Magnet Thickness, NdFeB Magnet Width, Magnet Position from Center of Shaft, Rotor Bridge Thickness, Rotor Rib Thickness

4.3.2 Optimization Results and Final Sample Selection

The optimization results were exported from Maxwell and post-processed in MATLAB. For each machine the average torque and torque ripple of all 100 samples were plotted. The best sample was then highlighted on the plot. Figures 4.1, 4.2, and 4.3 show the optimization results for the three motor topologies.

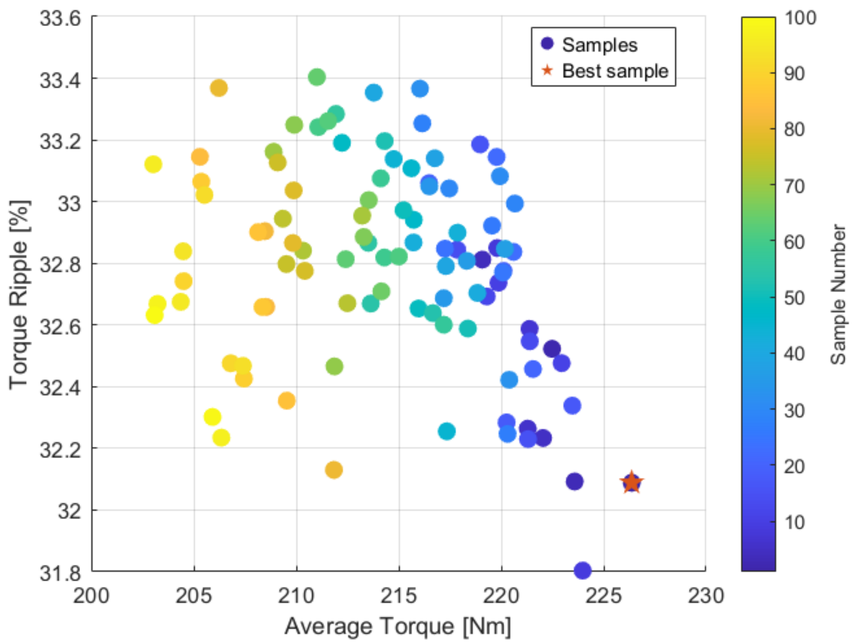

Figure 4.1: Optimization results for the hybrid magnet PMaSynRM. Each point represents one rotor geometry sample. The best sample point corresponds to the selected sample with the minimum cost function value.

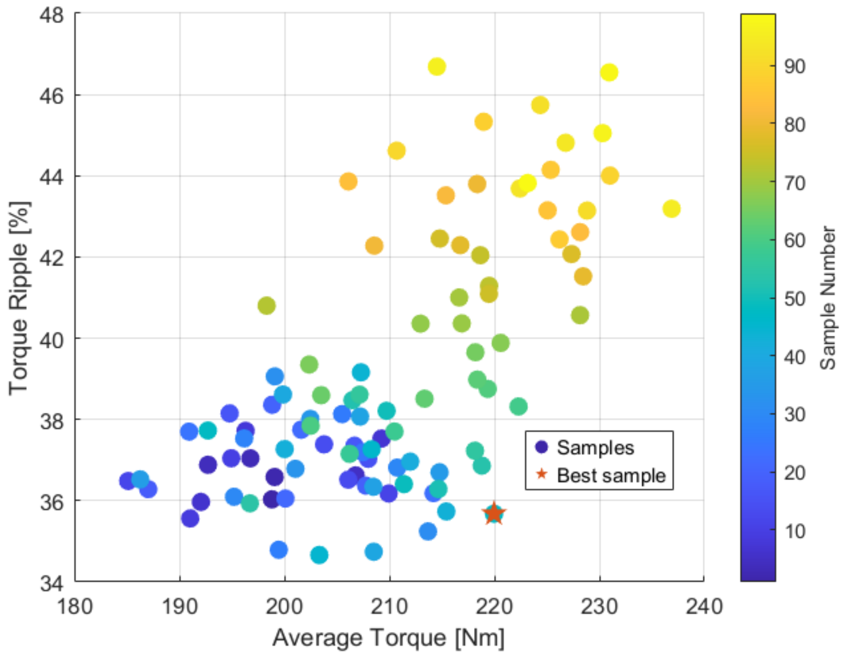

Figure 4.2: Optimization results for the ferrite spoke PMSM. Each point represents one rotor geometry sample. The best sample point corresponds to the selected sample with the minimum cost function value.

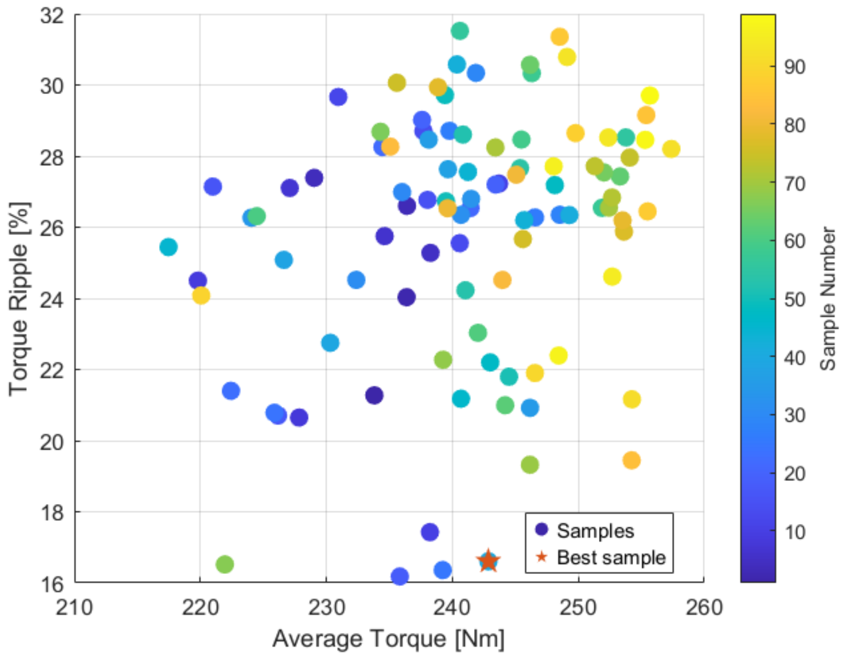

Figure 4.3: Optimization results for the NdFeB VPMSM reference machine. Each point represents one rotor geometry sample. The best sample point corresponds to the selected sample with the minimum cost function value.

After the best sample was identified for each machine, the optimized rotor geometrical parameters were applied to the final motor model. These optimized geometries were then used for the subsequent performance comparison, loss maps, efficiency map, demagnetization analysis, mechanical rotor stress analysis and drive-cycle energy-consumption study.

4.4 Final Selected Machine Geometries

After the preliminary rotor diameter study and the rotor geometry optimization, one final geometry was selected for each machine topology. The selected geometries correspond to the samples with the minimum value of the optimization cost function for the hybrid-magnet PMaSynRM, the ferrite spoke PMSM and the NdFeB VPMSM reference machine. These final geometries were then used for the subsequent electromagnetic, mechanical, demagnetization, loss-map, efficiency-map and drive cycle analysis.

The three machines use the same stator and winding platform in order to make the comparison as consistent as possible. Therefore, the main differences between the machines are introduced through the rotor topology, magnet arrangement, and magnet material. The common stator and winding parameters are given in Table 4.4. The topology-specific rotor geometries and their corresponding parameters are then presented separately for each machine.

4.4.1 Common Stator and Winding Parameters

The stator design was kept the same for all three machines. This allows the effect of the rotor topology and magnet material to be compared under the same slot number, pole number, air gap length and winding arrangement.

Table 4.4: Common stator and winding parameters used for all three machines.

Parameter	**Symbol**	**Value**	**Unit**
Number of stator slots	S	48	–
Number of poles	P	8	–
Number of phases	m	3	–
Slots per pole per phase	q	2	–
Winding type	–	Single-layer distributed	–
Air gap length	g	0.8	mm
Number of parallel branches	N_{pb}	2	–
Wire diameter	d_{wire}	0.4	mm
Slot fill factor	k_{fill}	45	%
Number of turns	N_{turns}	5	

4.4.2 Hybrid-Magnet PMaSynRM Geometry

The final selected hybrid-magnet PMaSynRM geometry is shown in Figure 4.4.

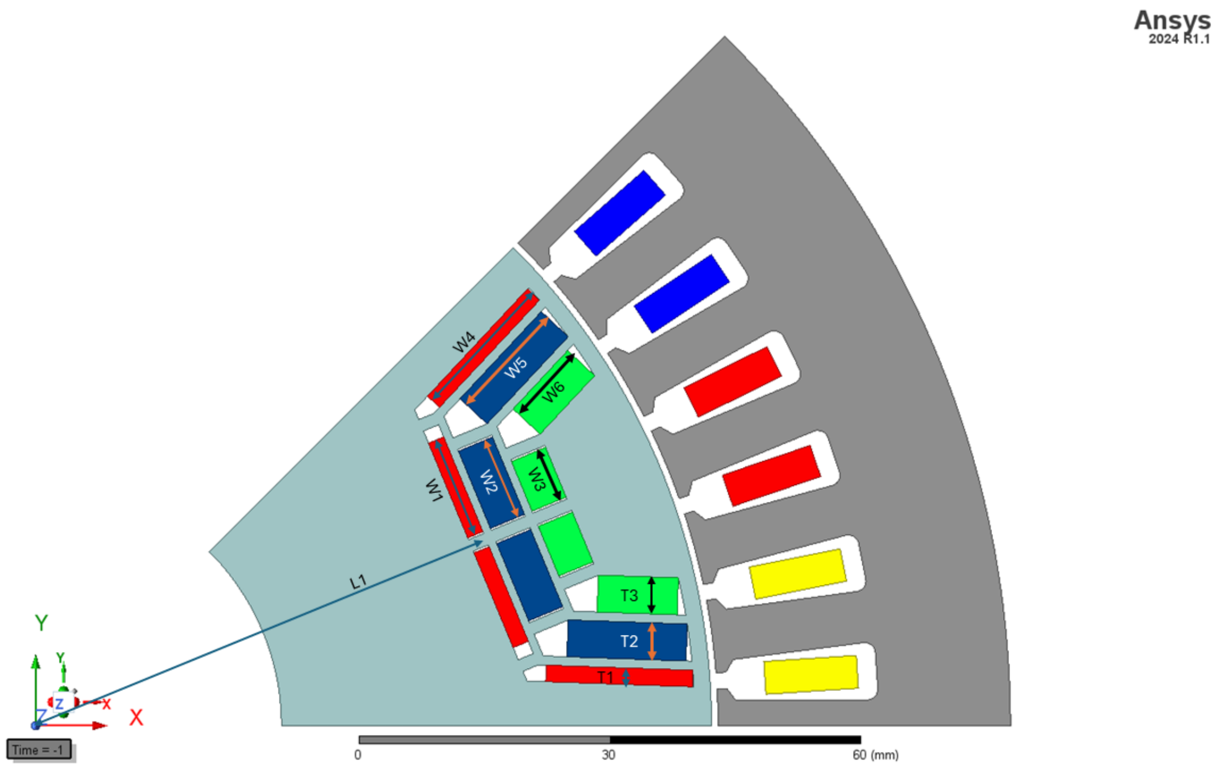

Figure 4.4: Final selected reduced geometry of the hybrid magnet PMaSynRM

The rotor contains multiple flux barriers together with ferrite and NdFeB magnets. This topology is intended to produce torque from both the permanent magnet torque component and the reluctance torque component. The use of hybrid magnets allows the NdFeB magnet volume to be reduced compared with a pure NdFeB VPMSM while the flux-barrier structure contributes to rotor saliency. The inner flux barriers contain NdFeB magnets while the outer two flux barriers contain Ferrite magnets.

Table 4.5: Final selected rotor geometrical parameters of the hybrid magnet PMaSynRM.

Parameter	Symbol	Value	Unit
Rotor outer diameter	D_r	165	mm
Shaft diameter	D_{sh}	60	mm
NdFeB centre magnet width	W_1	12.5	mm
NdFeB side magnet width	W_4	17.9	mm
NdFeB magnet thickness	T_1	2.0	mm
NdFeB magnet distance from centre	L_1	115	mm
Middle ferrite centre magnet width	W_2	10.2	mm
Middle ferrite side magnet width	W_5	14.5	mm
Middle ferrite magnet thickness	T_2	4.5	mm
Middle ferrite magnet distance from centre	L_2	121	mm
Outer ferrite centre magnet width	W_3	6.56	mm
Outer ferrite side magnet width	W_6	9.76	mm
Outer ferrite magnet thickness	T_3	4.51	mm
Outer ferrite magnet distance from centre	L_3	132	mm

4.4.3 Ferrite Spoke PMSM Geometry

The final selected ferrite spoke PMSM geometry is shown in Figure 4.5.

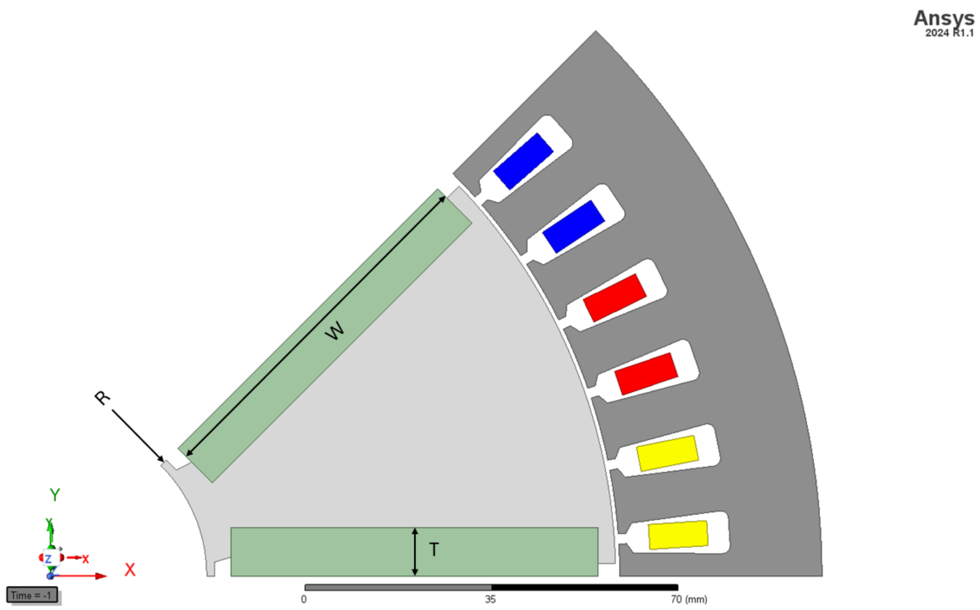

Figure 4.5: Final selected reduced geometry of the ferrite spoke PMSM.

In this topology ferrite magnets are arranged in a spoke-type configuration. The purpose of this arrangement is to concentrate the magnet flux through the rotor iron and increase the effective air-gap flux density. This is especially useful for ferrite magnets which have lower remanent flux density than NdFeB magnets.

Table 4.6: Final selected rotor geometrical parameters of the ferrite spoke PMSM.

Parameter	**Symbol**	**Value**	**Unit**
Rotor outer diameter	D_r	165	mm
Shaft diameter	D_sh	60	mm
Magnet width	W	70.5	mm
Magnet half-thickness	T	9.3	mm
Inner rib thickness	R	1.5	mm

4.4.4 NdFeB VPMSM Reference Geometry

The final selected NdFeB VPMSM reference geometry is shown in Figure 4.6.

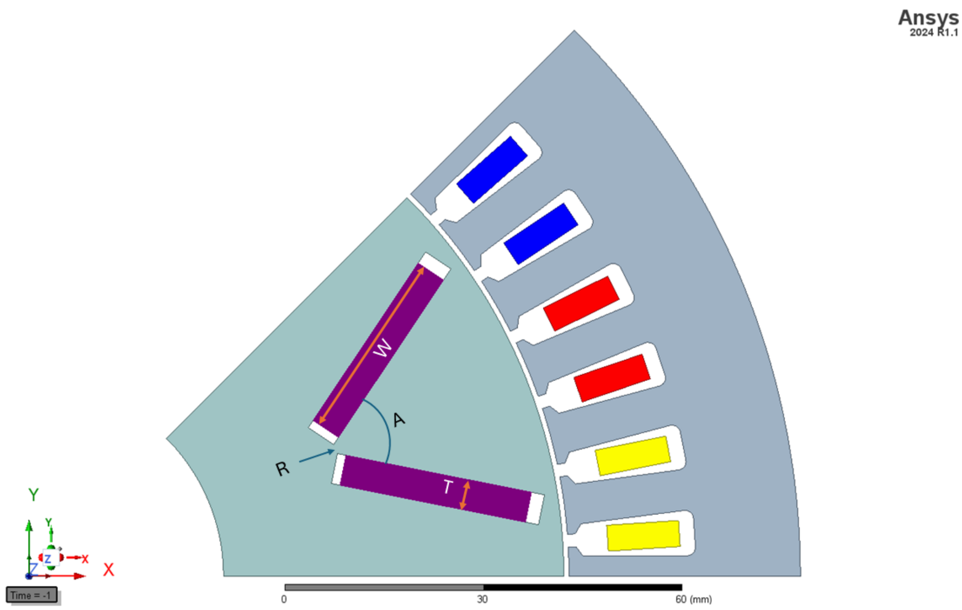

Figure 4.6: Final selected reduced geometry of the NdFeB VPMSM reference machine.

This machine uses V-shaped embedded NdFeB magnets and is included as a reference design. Since NdFeB magnets have higher remanent flux density than ferrite magnets this design provides a useful benchmark for torque density, power capability and efficiency.

Table 4.7: Final selected rotor geometrical parameters of the NdFeB VPMSM reference machine.

Parameter	**Symbol**	**Value**	**Unit**
Rotor outer diameter	D_{r}	165	mm
Shaft diameter	D_{sh}	60	mm
Magnet width	W	29.1	mm
Magnet thickness	T	4.7	mm
Rib thickness	R	1.5	mm
V-angle	A	67.5	deg

4.5 Rotor Mechanical Stress Analysis

After selecting the final optimized rotor geometries, a mechanical rotor stress analysis was carried out for the hybrid-magnet PMaSynRM, the ferrite spoke PMSM and the NdFeB VPMSM reference machine. The purpose of this analysis was to verify that the optimized rotor structures can withstand the centrifugal loading at the maximum mechanical speed of the motor.

The analysis was performed in Motor-CAD using the mechanical rotor stress module. Only mechanical centrifugal effects were considered. Thermal effects, electromagnetic effects and coupled electromagnetic-thermal-mechanical effects were not included in this analysis. Therefore the results should be interpreted as a mechanical verification of the rotor geometry under rotational loading rather than as a complete multiphysics stress analysis.

The mechanical analysis was performed at the maximum speed of 7000 rpm which corresponds to the maximum mechanical speed specified for the traction motor. A mesh size of 0.1 mm was used. The main quantities evaluated were the equivalent von Mises stress also referred to here as SVM stress and the total displacement magnitude U. The von Mises stress is used to identify highly stressed regions of the rotor, while the displacement plot is used to check whether the rotor deformation remains small.

Figures 4.7- 4.9 show the SVM stress and displacement distributions for the three optimized rotors. For each machine, the stress plot is shown on the left and the displacement plot is shown on the right.

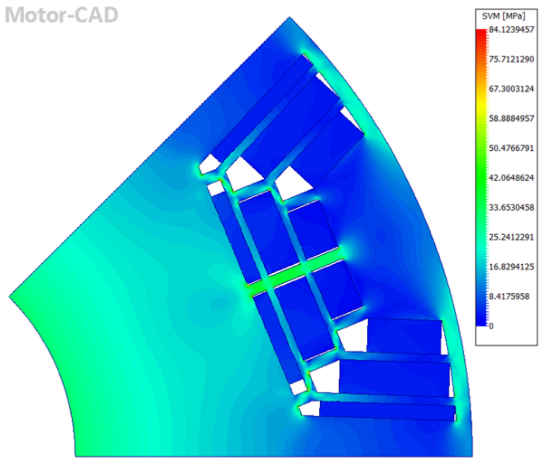

Figure 4.7: Mechanical stress analysis results for the hybrid-magnet PMaSynRM rotor at 7000 rpm **(Left - Stress Plot, Right - Displacement Plot)**.

The PMaSynRM rotor as shown in Fig 4.7 shows a high factor of safety of 4.75. The stress concentration is mainly associated with the rotor bridge and rib regions, which are responsible for mechanically supporting the flux-barrier and magnet structures under rotation. The displacement magnitude remains small, indicating that the rotor deformation is limited under the applied centrifugal loading.

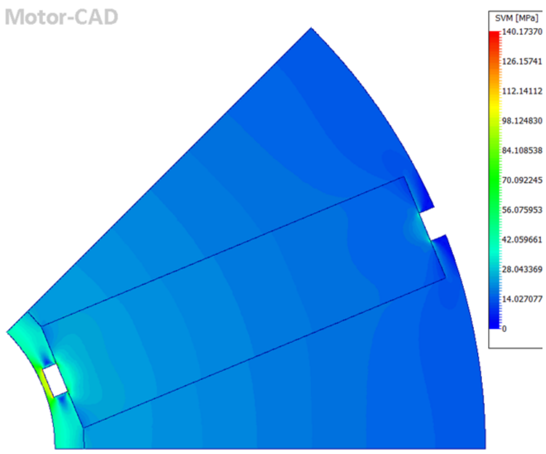

Figure 4.8: Mechanical stress analysis results for the ferrite spoke PMSM rotor at 7000 rpm **(Left - Stress Plot, Right - Displacement Plot)**.

The ferrite spoke PMSM as shown in Fig 4.8 gives the lowest factor of safety among the three machines with a value of 2.85. The highest SVM stress occurs in the inner rib of the rotor close to the shaft. This is expected because the spoke-type rotor contains air pockets and flux-concentrating paths, so the inner ribs and retaining regions carry a significant part of the centrifugal mechanical load. Although the factor of safety is lower than in the PMaSynRM and VPMSM, the displacement remains small indicating that the deformation is still limited at the maximum speed.

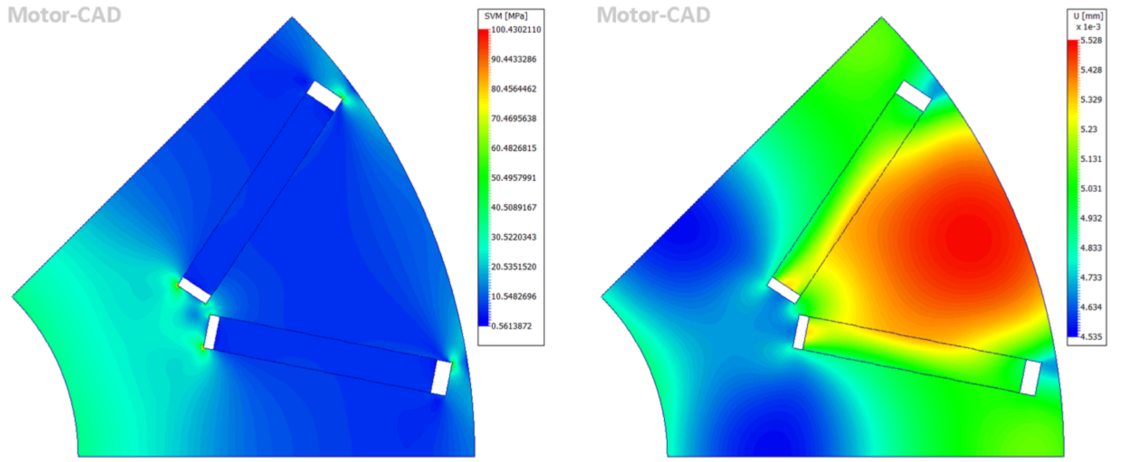

Figure 4.9: Mechanical stress analysis results for the NdFeB VPMSM reference rotor at 7000 rpm **(Left - Stress Plot, Right - Displacement Plot)**.

The NdFeB VPMSM reference rotor as shown in Fig 4.9 also gives a high factor of safety of 3.98. The stress is concentrated mainly around the magnet bridge and rib regions. These regions are important because they retain the magnets against centrifugal loading. Similar to the other two rotors the displacement is small suggesting that the rotor deformation is not critical at the maximum speed.

The maximum stress, maximum displacement and minimum factor of safety obtained for the three rotors are given in Table 4.8.

Table 4.8: Rotor Mechanical Stress Analysis results at 7000 rpm.

Machine	**Max. SVM stress (MPa)**	**Max. displacement (mm)**	**Min. FoS –**	**Critical region**
Hybrid-magnet PMaSynRM	84.124	6.89e-03	4.75	Rotor bridge/rib region
Ferrite spoke PMSM	140.174	8.78e-03	2.85	Inner rib region near the shaft
NdFeB VPMSM reference	100.43	5.528e-03	3.98	Rotor bridge/rib region

The factor of safety values show that all three rotors satisfy the mechanical stress requirement under the assumed purely mechanical centrifugal loading. However the ferrite spoke PMSM has the lowest factor of safety among the three designs.

4.6 Electromagnetic Performance Comparison

After the final geometries were selected the electromagnetic performance of the three optimized machines was evaluated and compared. The comparison focuses on the torque-speed and power-speed characteristics of the hybrid-magnet PMaSynRM, the ferrite spoke PMSM and the NdFeB VPMSM reference machine.

4.6.1 Torque-Speed Characteristics

The torque-speed characteristics of the three optimized machines are shown in Figure 4.10.

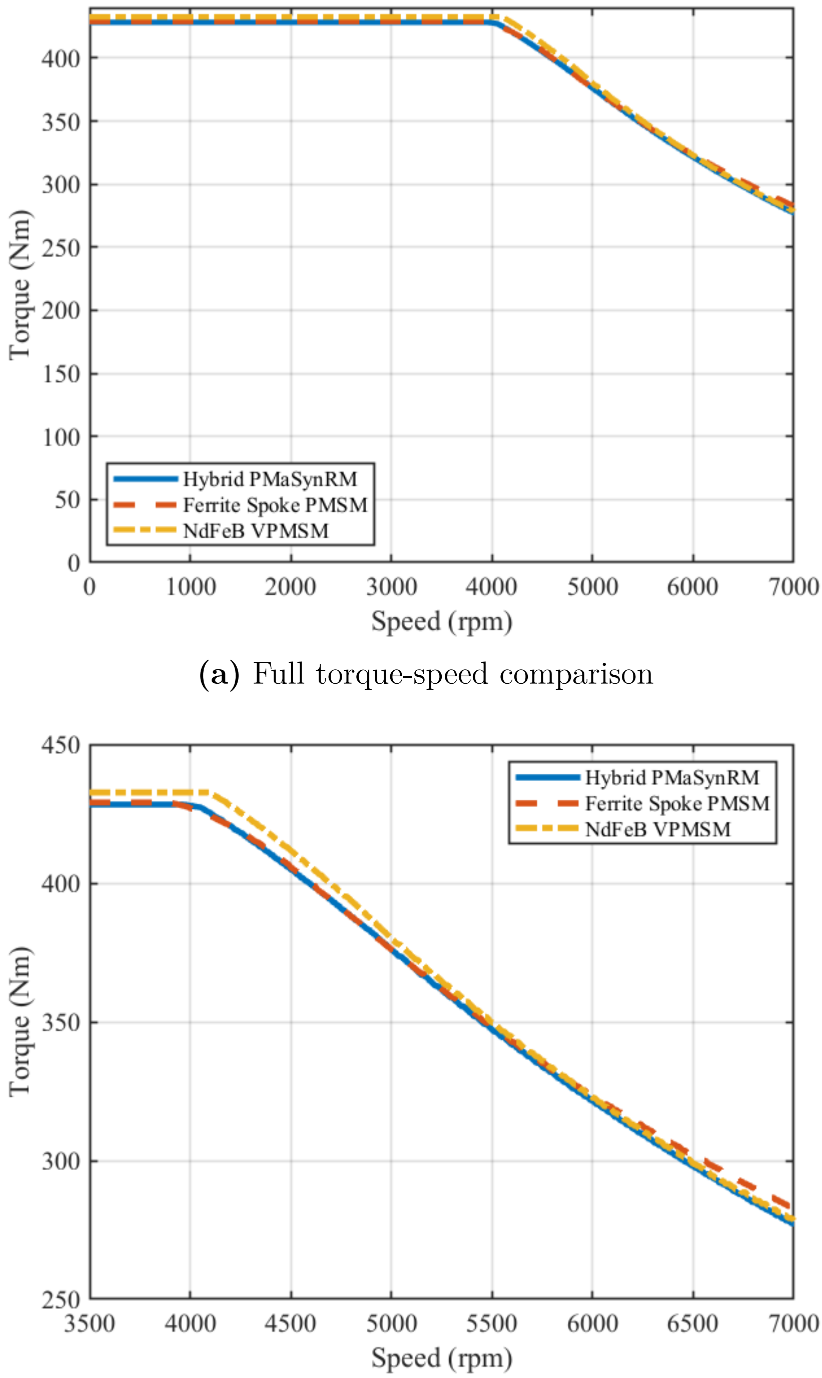

(a) Full torque-speed comparison

(b) Zoomed torque-speed comparison

Figure 4.10: Torque-speed characteristics of the three optimized machines.

In the constant torque region the NdFeB VPMSM produces the highest torque, followed by the hybrid-magnet PMaSynRM and then the ferrite spoke PMSM. This is expected because the VPMSM uses NdFeB magnets which provide a higher magnetic loading than ferrite magnets. The hybrid-magnet PMaSynRM gives a slightly lower torque than the NdFeB VPMSM, but it still remains close to the reference machine because it uses both permanent-magnet torque and reluctance torque. The ferrite spoke PMSM gives the lowest torque in this region, mainly because ferrite magnets have lower remanent flux density than NdFeB magnets.

The base-speed capability follows the same trend. The NdFeB VPMSM has the highest base speed followed by the hybrid-magnet PMaSynRM and then the ferrite spoke PMSM. This indicates that the NdFeB VPMSM and PMaSynRM can maintain the maximum torque over a slightly wider low-speed range than the ferrite spoke PMSM.

In the field-weakening region, however, the trend changes. The ferrite spoke PMSM provides the highest torque at higher speeds, while the torque values of the NdFeB VPMSM and the hybrid-magnet PMaSynRM become almost equal. This suggests that the ferrite spoke PMSM has better high-speed torque retention in the field-weakening region, even though its low-speed torque and base speed are slightly lower. Therefore the spoke topology appears to be better at higher speeds whereas the NdFeB VPMSM and PMaSynRM are better in the constant-torque region.

4.6.2 Power-Speed Characteristics

The corresponding power-speed characteristics are shown in Figure 4.11.

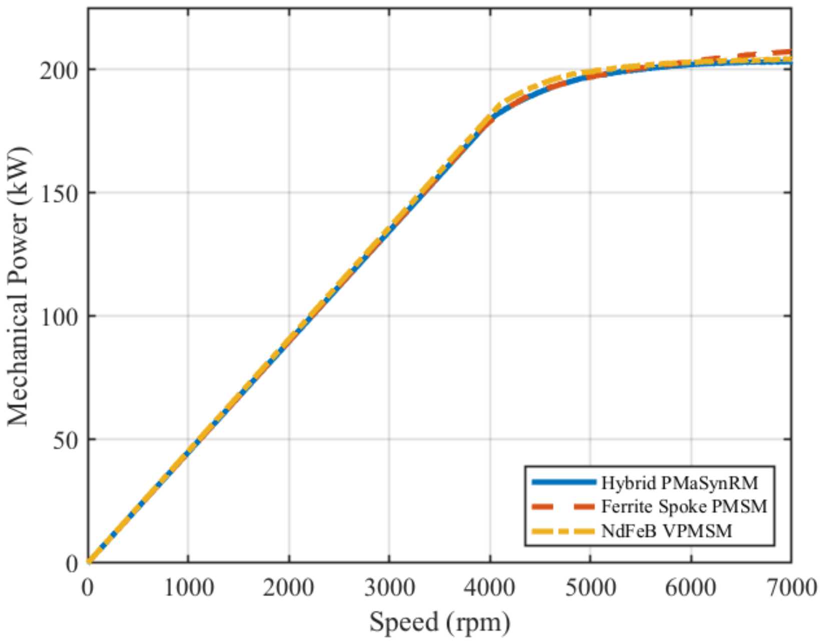

(a) Full power-speed comparison

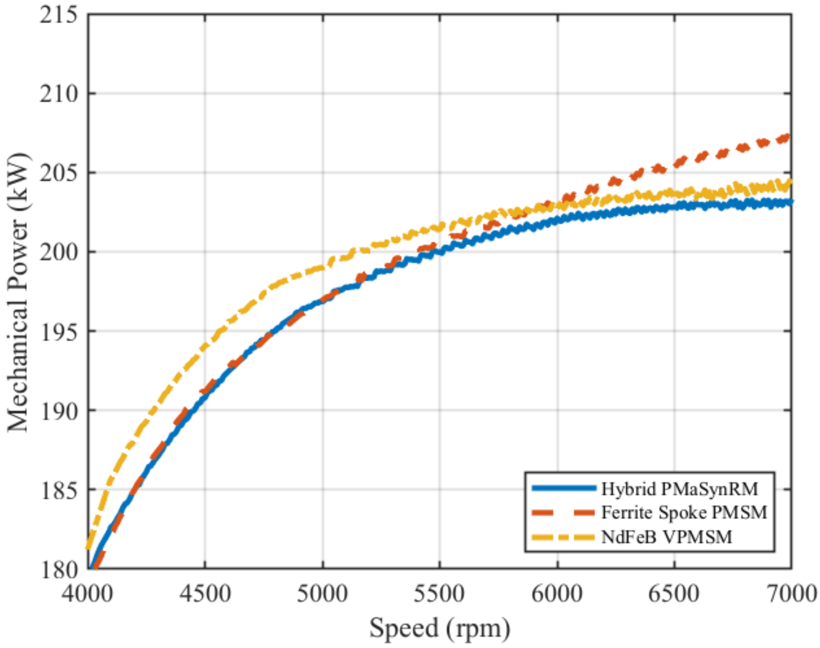

(b) Zoomed power-speed comparison

Figure 4.11: Power-speed characteristics of the three optimized machines.

Below base speed the output power of all three machines is almost the same. This occurs because all three machines are able to operate close to the same maximum torque level over the low-speed region and the mechanical power increases approximately linearly with speed in the constant-torque region.

Above base speed the difference between the machines becomes clearer. In the field-weakening region the ferrite spoke PMSM provides the highest output power. This agrees with the torque-speed result where the spoke PMSM shows better high-speed torque retention. The hybrid-magnet PMaSynRM and the NdFeB VPMSM show almost equal power in the field-weakening region indicating that their high-speed torque capability is similar after the voltage limitation becomes dominant.

The torque-speed and power-speed results show that the NdFeB VPMSM has an advantage in the constant-torque region, while the hybrid-magnet PMaSynRM remains close to the reference machine with reduced NdFeB usage. The ferrite spoke PMSM has slightly lower torque and base speed, but it performs better in the field-weakening region where it provides the highest torque and power among the three machines.

4.6.3 MTPA, Field-Weakening and MTPV Characteristics

The current trajectories of the three optimized machines were evaluated in the dq current plane in order to analyse the maximum-torque-per-ampere (MTPA), field-weakening (FW) and maximum-torque-per-voltage (MTPV) behaviour.

At low speed the optimal operating points follow the MTPA trajectory. In this region the voltage constraint is not yet limiting and the current vector is selected to produce the required torque with minimum current magnitude. As speed increases the voltage limit becomes more restrictive. In the i_d-i_q plane this appears as voltage ellipses that shrink with increasing speed. Once the MTPA operating point lies outside the voltage ellipse for a given speed, the machine can no longer operate on the MTPA trajectory and must move into the field-weakening region.

The MTPA, FW, voltage ellipses and infinite-speed point of the three machines are shown in Figures 4.12-4.14. The infinite-speed point represents the limiting current point approached at very high speed where the flux linkage must be sufficiently weakened to satisfy the voltage constraint.

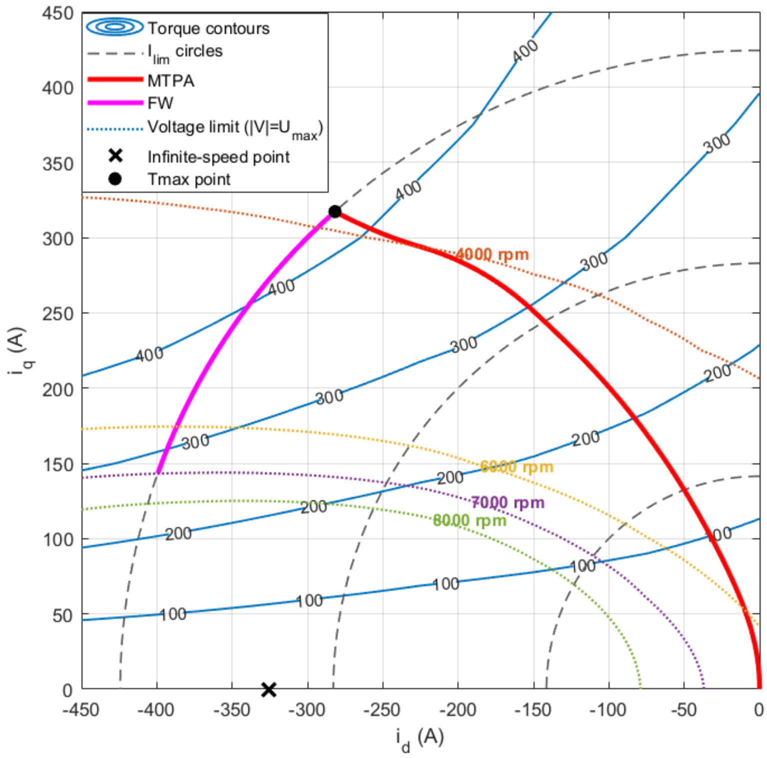

Figure 4.12: MTPA and field-weakening trajectory of the hybrid PMaSynRM in the i_d-i_q plane.

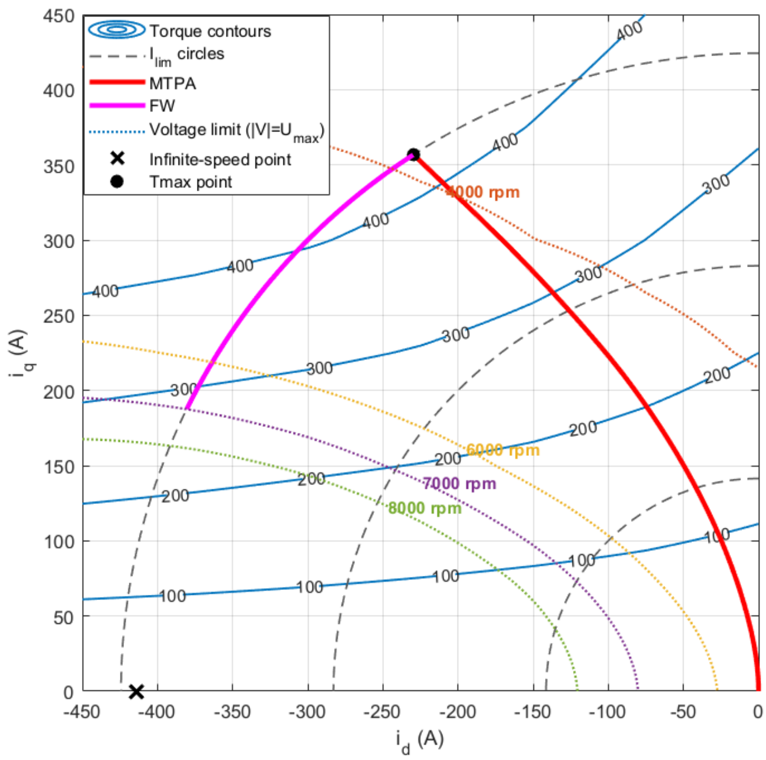

Figure 4.13: MTPA and field-weakening trajectory of the ferrite spoke PMSM in the i_d-i_q plane.

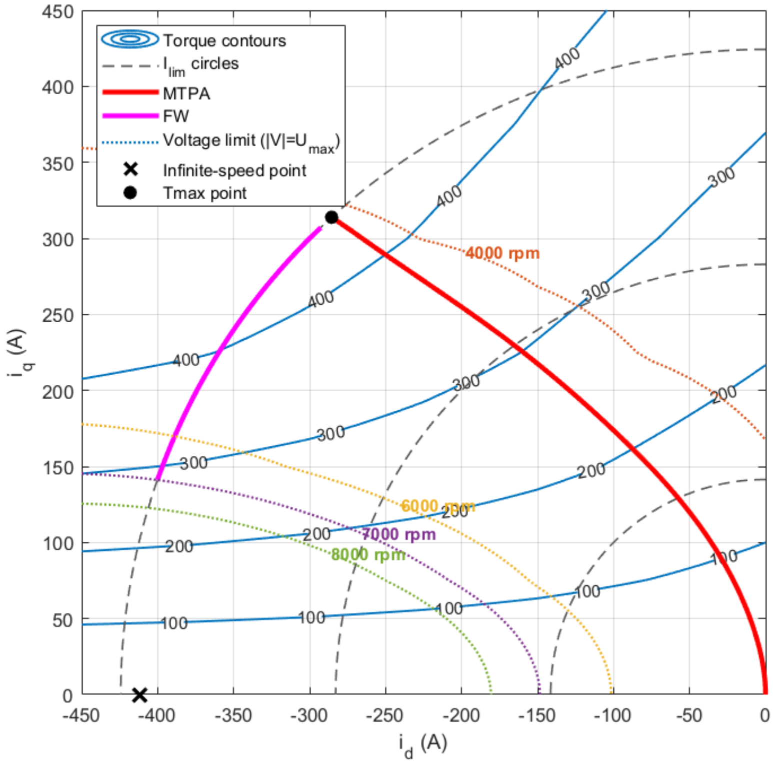

Figure 4.14: MTPA and field-weakening trajectory of the NdFeB VPMSM in the i_d-i_q plane.

For the NdFeB VPMSM and the hybrid-magnet PMaSynRM, the MTPA trajectory is inclined at approximately 50°-55° from the horizontal axis. This means that as i_q increases a noticeable increase in negative i_d is also required. This behaviour is expected for interior permanent-magnet and PM-assisted synchronous reluctance machines because negative i_d current helps exploit rotor saliency and increase the reluctance torque contribution.

For the ferrite spoke PMSM the MTPA trajectory is more vertical, with an inclination of approximately 65°-70° from the horizontal axis. This indicates that the increase in negative i_d current with increasing i_q is smaller than in the VPMSM and PMaSynRM cases. One possible reason is that the ferrite spoke PMSM behaves more strongly as a flux-concentrating permanent-magnet machine where the torque production is more dominated by the magnet torque component and less by the reluctance torque component. In that case the optimum MTPA current vector remains closer to the q-axis and requires less negative i_d current for the same increase in i_q. This is consistent with the fact that the slope of the MTPA trajectory depends on the relative contribution of permanent-magnet torque and reluctance torque.

The voltage ellipses also show the difference in base-speed capability between the machines. For the NdFeB VPMSM the MTPA operating point is still inside the voltage ellipse corresponding to approximately 4000 rpm. Therefore the VPMSM can remain on the MTPA trajectory up to a slightly higher speed. In contrast the corresponding MTPA points of the hybrid-magnet PMaSynRM and the ferrite spoke PMSM lie outside the 4000 rpm voltage ellipse. This indicates that these machines reach their voltage limit earlier and therefore have a lower base speed than the NdFeB VPMSM.

No distinct MTPV trajectory was observed within the investigated speed range up to 7000 rpm. A separate MTPV region may appear only at higher speeds with different voltage or current limits or if the machine saliency and characteristic current produce an MTPV transition within the available speed range.

4.6.4 Permanent-Magnet and Reluctance Torque Components

To understand the torque production mechanism of the three machines in more detail, the torque was separated into permanent-magnet torque and reluctance torque components. This comparison is useful because the three machines produce torque through different physical mechanisms. The NdFeB VPMSM is mainly dominated by permanent-magnet torque, the hybrid-magnet PMaSynRM produces torque from both permanent-magnet and rotor saliency while the ferrite spoke PMSM relies on ferrite magnet flux concentration.

The permanent-magnet torque components of the three machines are compared in Figure 4.15. The current angle is plotted on the horizontal axis. A current angle close to 90° corresponds to operation near the positive q-axis, while increasing the current angle towards 180° corresponds to increasing negative d axis current and reducing the q-axis current component.

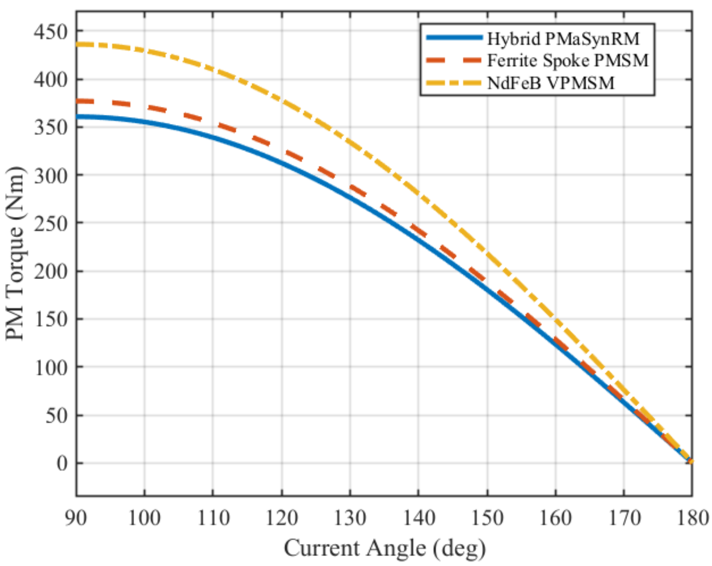

Figure 4.15: Comparison of permanent magnet torque component as a function of current angle for the three optimized machines.

From Figure 4.15 the NdFeB VPMSM produces the highest permanent-magnet torque over the full current-angle range. This is expected because the machine uses only NdFeB magnets which provide a higher air-gap flux contribution than ferrite magnets. The ferrite spoke PMSM gives the second-highest permanent-magnet torque for most of the current-angle range. This shows the benefit of the spoke-type flux-concentrating rotor, which helps to increase the effective air-gap flux density despite the lower remanence of ferrite magnets.

The hybrid-magnet PMaSynRM gives the lowest permanent-magnet torque component among the three machines. This is also expected because the PMaSynRM uses a reduced amount of NdFeB material and partly replaces the magnet torque contribution with reluctance torque.

For all three machines the permanent-magnet torque decreases as the current angle approaches 180°. This occurs because the q-axis current component decreases as the current vector moves further into the negative d axis direction. Since the permanent-magnet torque is mainly proportional to i_q, the PM torque approaches zero when the current vector becomes almost aligned with the negative d axis.

The reluctance torque components are compared in Figure 4.16.

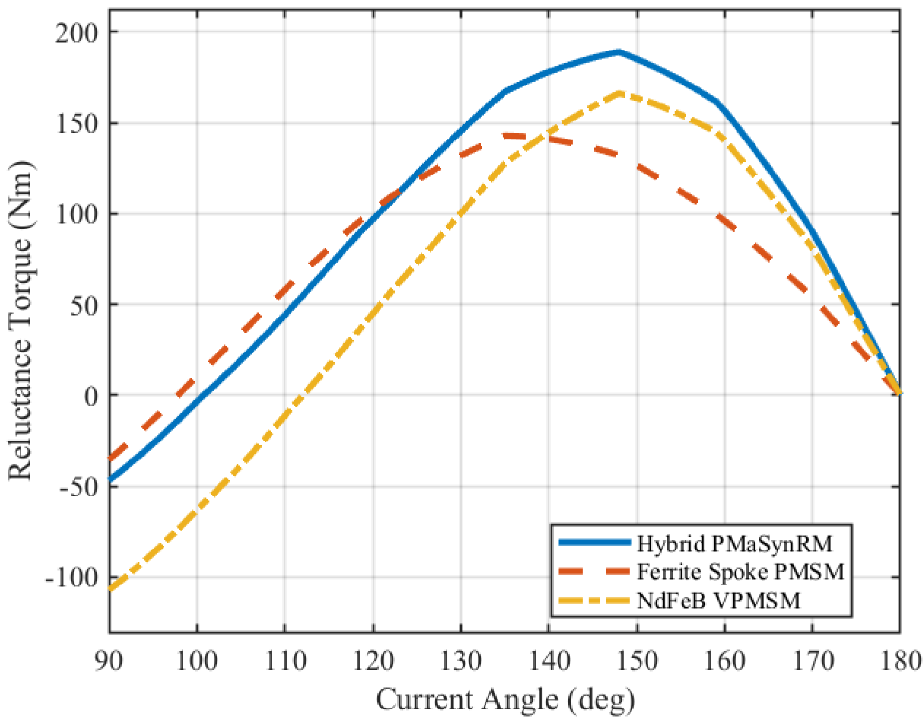

Figure 4.16: Comparison of reluctance torque component as a function of current angle for the three optimized machines.

Figure 4.16 shows that the hybrid-magnet PMaSynRM produces the highest peak reluctance torque. This is consistent with its rotor structure since the flux barriers are designed to create a strong difference between the d and q-axis magnetic paths. The larger saliency allows the PMaSynRM to compensate for its lower permanent-magnet torque and is one of the main reasons why the hybrid-magnet topology can reduce NdFeB usage while still maintaining competitive total torque.

The NdFeB VPMSM also produces a significant reluctance torque component. This is expected for an interior V-type permanent-magnet rotor because the V-shaped flux barriers and iron paths create saliency. However its peak reluctance torque is lower than that of the PMaSynRM. The VPMSM therefore obtains its overall torque mainly from the strong NdFeB magnet torque with reluctance torque acting as an additional contribution.

The ferrite spoke PMSM has the lowest peak reluctance torque among the three machines. Its reluctance torque reaches a maximum at a lower current angle and then decreases as the current angle increases further. This suggests that the spoke rotor behaves more strongly as a flux-concentrating permanent-magnet machine than as a highly salient reluctance-torque machine. The spoke rotor geometry is effective for concentrating ferrite magnet flux but it does not provide as strong a reluctance torque contribution like the flux-barrier structure of the PMaSynRM.

At lower current angles, the reluctance torque is negative for some of the machines. It means that the reluctance torque component opposes the permanent-magnet torque in that region. Since the permanent-magnet torque is still large near 90°, the total torque remains positive. As the current angle increases, the negative d axis current becomes more significant and the reluctance torque becomes positive, contributing to the total torque production.

At current angles close to 180° the reluctance torque of all three machines approaches zero. This is because the q-axis current component becomes small and the reluctance torque is proportional to the product of the d and q-axis current components. Therefore even if the negative d axis current is large the reluctance torque decreases when i_q becomes small.

4.7 Losses and Efficiency

4.7.1 Copper Loss

The copper loss maps of the three optimized machines are shown in Figure 4.17. The copper loss is mainly driven by the resistive losses in the stator winding and is strongly dependent on the current required to produce a given torque. In the constant torque region the copper loss contours are nearly horizontal because the required current is mainly determined by torque rather than speed. In the field weakening region the current vector changes with speed due to the voltage limitation and the copper loss contours bend with increasing speed.

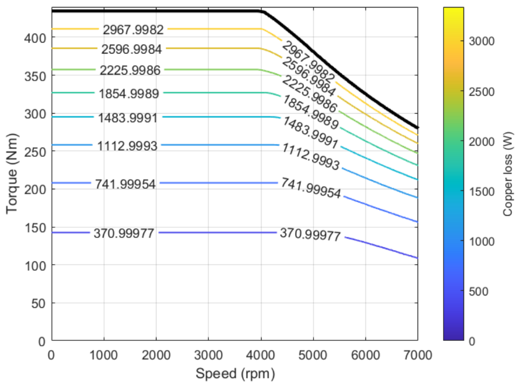

(a) Hybrid PMaSynRM

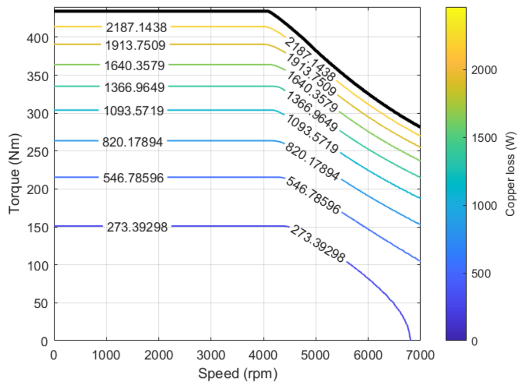

(b) NdFeB VPMSM

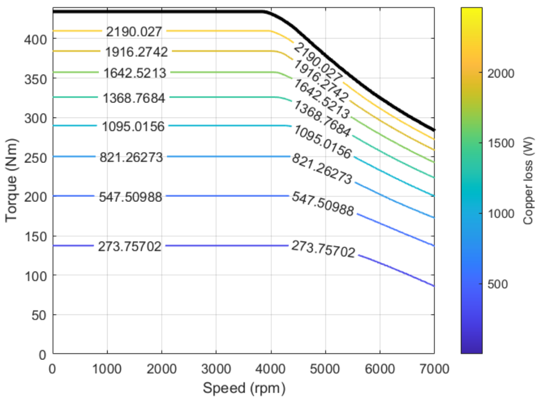

(c) Ferrite spoke PMSM

Figure 4.17: Copper loss maps of the three optimized machines.

From Figure 4.17 it can be observed that the hybrid magnet PMaSynRM has the highest copper loss among the three machines. The maximum copper loss is approximately 3 kW for the PMaSynRM whereas the maximum copper losses of the NdFeB VPMSM and the ferrite spoke PMSM are both close to 2.2 kW. So although the PMaSynRM reduces the use of NdFeB magnet material, it requires a higher current loading to achieve comparable torque. Since copper loss increases with the square of current even a moderate increase in current demand can lead to an increase in copper loss.

The higher copper loss of the PMaSynRM is mostly due to its long axial length. The PMaSynRM also relies more strongly on reluctance torque and uses a reduced amount of NdFeB magnet material compared with the VPMSM. So a larger current is required to generate the same torque level in regions where both negative i_d and positive i_q currents are needed. This increases the RMS current and therefore increases the winding losses.

The NdFeB VPMSM shows lower copper loss because its strong NdFeB magnet provides high torque per ampere and it has shorter axial length. Hence for the same torque demand, less stator current is required compared with the PMaSynRM.

The ferrite spoke PMSM gives copper losses close to the NdFeB VPMSM even though it uses ferrite magnets. This is mainly because the spoke type rotor provides flux concentration which improves the effective use of the ferrite magnets. In addition the ferrite spoke PMSM has a larger stator inner diameter which increases the torque arm and helps produce torque with a lower current loading.

4.7.2 Hysteresis Loss

The hysteresis loss maps of the three optimized machines are shown in Figure 4.18. The hysteresis loss is part of the iron loss and is due to the repeated magnetization and demagnetization of the laminated stator and rotor cores. Hysteresis loss is strongly dependent on magnetic flux density, electric frequency and the amount of active iron exposed to alternating flux.

In this thesis the hysteresis loss results include a build factor of 2.

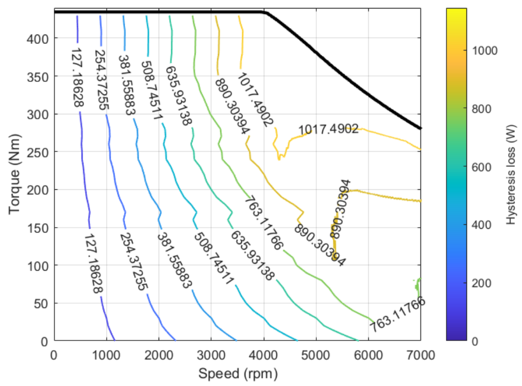

(a) Hybrid PMaSynRM

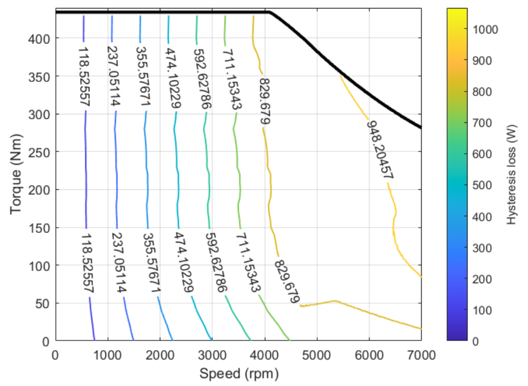

(b) NdFeB VPMSM

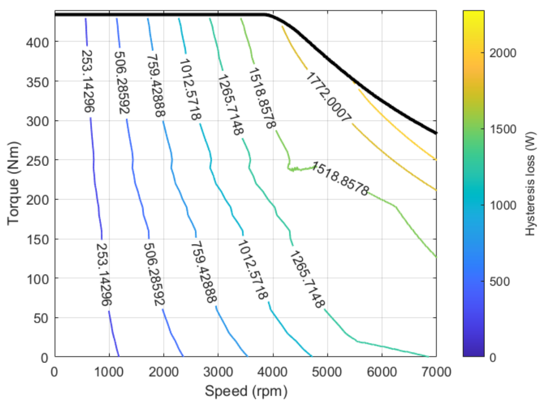

(c) Ferrite spoke PMSM

Figure 4.18: Hysteresis loss maps of the three optimized machines.

From Figure 4.18 it can be observed that the ferrite spoke PMSM has the highest hysteresis loss among the three machines. The maximum hysteresis loss of the spoke PMSM is approximately 2.1-2.2 kW, whereas the maximum hysteresis losses of the PMaSynRM and NdFeB VPMSM are closer to approximately 1.1 kW. Therefore the spoke PMSM shows a clear hysteresis loss penalty compared with the other two machines.

The higher hysteresis loss of the ferrite spoke PMSM is mainly caused by its larger active diameter, larger iron volume and flux-concentrating rotor structure. The spoke-type topology is useful for ferrite magnets because it concentrates the magnet flux through the rotor iron and increases the effective air-gap flux density. However this also means that parts of the rotor and stator iron are exposed to stronger alternating flux. As a result, the hysteresis loss increases. Also the ferrite spoke PMSM has a larger stator inner diameter and a long axial length which increases the amount of active iron contributing to the total hysteresis loss.

The PMaSynRM has slightly higher hysteresis loss than the NdFeB VPMSM. This is because the PMaSynRM has a longer axial length than the VPMSM and contains flux barriers that create a more complex flux path in the rotor which increase local flux density variations and therefore increase iron loss. However the PMaSynRM uses less NdFeB magnet material than the VPMSM, so the lower permanent-magnet flux partly compensates for the increased active length and rotor complexity.

The contour shapes also show that the hysteresis loss is strongly dependent on speed. In the low-speed region, the hysteresis loss remains relatively low. As the speed increases, the electrical frequency increases and the hysteresis loss rises as they are more dependent on speed than torque. Torque still affects the hysteresis loss because the stator current changes the local flux density distribution especially in saturated regions but the dominant trend is the increase in loss with speed.

4.7.3 Eddy Current Loss Maps

The eddy current loss maps of the three optimized machines are shown in Figure 4.19. Eddy current loss is a component of the iron loss and is produced by circulating currents induced in the laminated magnetic core due to time-varying magnetic flux. Compared with hysteresis loss, eddy current loss is more strongly influenced by the electrical frequency.

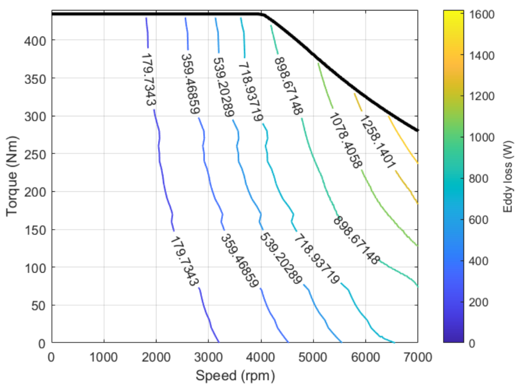

(a) Hybrid PMaSynRM

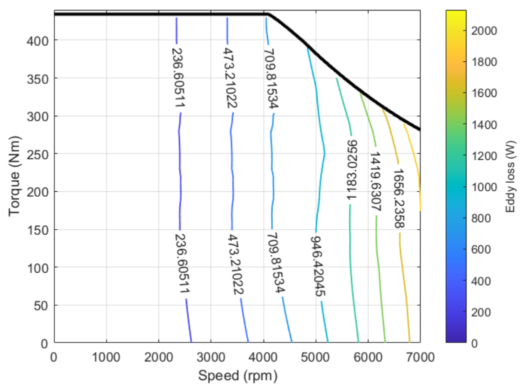

(b) NdFeB VPMSM

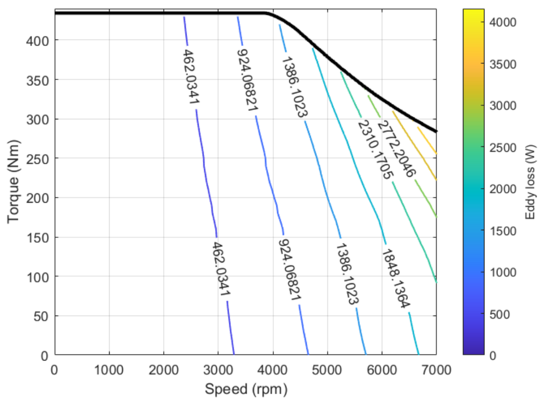

(c) Ferrite spoke PMSM

Figure 4.19: Eddy current loss maps of the three optimized machines.

From Figure 4.19 it can be observed that the ferrite spoke PMSM has the highest eddy-current loss among the three machines. The maximum eddy-current loss of the spoke PMSM reaches approximately 4 kW while the maximum eddy current losses of the PMaSynRM and NdFeB VPMSM are much lower. The NdFeB VPMSM reaches approximately 2 kW whereas the PMaSynRM is closer to approximately 1.5-1.6 kW. Therefore, the eddy current loss penalty of the ferrite spoke PMSM is significantly larger than that of the other two designs.

The high eddy-current loss of the ferrite spoke PMSM is mainly caused by its larger active diameter, larger iron volume and flux-concentrating rotor structure. The flux-concentrating effect increases the flux-density variation in parts of the rotor and stator iron. The larger diameter and spoke-type rotor paths expose a larger amount of iron to alternating flux. Since eddy current loss is strongly affected by electrical frequency and flux density variation, this leads to higher eddy-current loss especially at high speeds.

The NdFeB VPMSM has a moderate eddy-current loss level. Although it has the shortest axial length among the three machines, the strong NdFeB magnets produce a high magnetic loading. This can increase the flux-density variation in the stator and rotor iron particularly at high speed. As a result, the VPMSM shows higher eddy current loss than the PMaSynRM in some parts of the high-speed region.

The PMaSynRM shows the lowest or nearly the lowest eddy-current loss among the three machines. This is surprising because the PMaSynRM has a longer axial length than the VPMSM. However the PMaSynRM uses reduced NdFeB magnet volume and contains flux barriers, which can reduce the permanent magnet flux density compared with the NdFeB VPMSM. Therefore, despite its longer stack length the lower magnet flux and flux-barrier structure help limit the eddy current loss.

The contour shapes show that the eddy current loss is primarily speed dependent. At low speeds the eddy-current loss remains relatively small. As speed increases, the electrical frequency increases and the eddy-current loss rises rapidly. This is why the loss contours are mainly aligned with speed. Torque also influences the eddy current loss to a small extent because higher torque requires higher current which modifies the flux distribution.

4.7.4 Total Losses

The total loss maps of the three optimized machines are shown in Figure 4.20. The total loss is defined as the sum of copper loss and core loss,

$$P_{\text{loss,total}} = P_{\text{cu}} + P_{\text{hyst}} + P_{\text{eddy}}. \tag{4.3}$$

The mechanical losses, inverter losses and other auxiliary losses are not included in these maps. Therefore the total loss shown here represents the main electromagnetic loss components considered in Ansys Maxwell 2D.

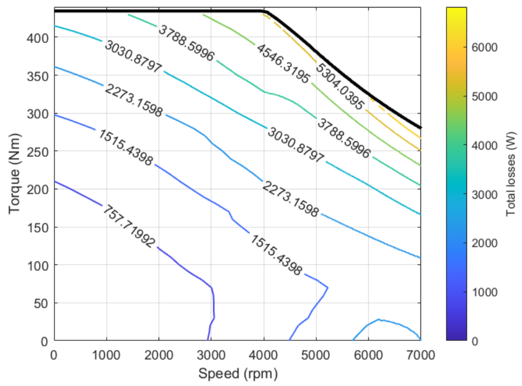

(a) Hybrid PMaSynRM

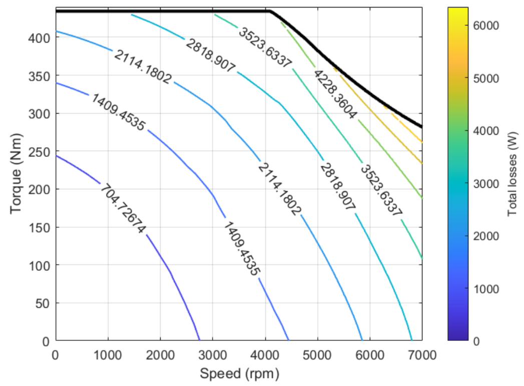

(b) NdFeB VPMSM

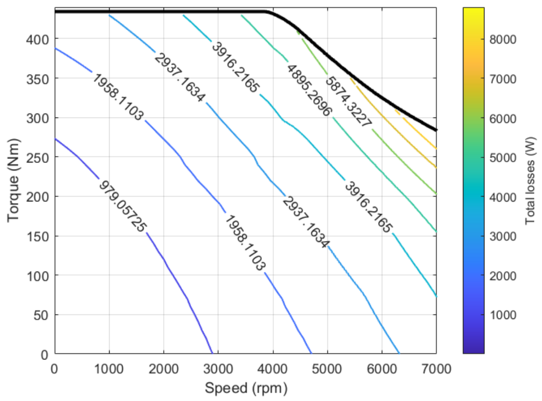

(c) Ferrite spoke PMSM

Figure 4.20: Total loss maps of the three optimized machines.

From Figure 4.20 it can be observed that the ferrite spoke PMSM has the highest total loss among the three machines especially in the high speed and high torque region. This is mainly due to the higher core losses of the spoke topology particularly the eddy current loss which becomes large at high speed because of the larger active diameter and flux-concentrating rotor structure.

The PMaSynRM and the NdFeB VPMSM have lower total losses than the ferrite spoke PMSM. But overall, NdFeB VPMSM on average has the lowest total loss due to the lowest copper loss compared to PMaSynRM and moderate core losses.

4.7.5 Efficiency Maps

The efficiency maps of the three optimized machines are shown in Figure 4.21. The efficiency was calculated using the electromagnetic losses considered in this thesis namely copper loss and core loss. A build factor of 2 was considered for core losses. Mechanical losses, inverter losses and auxiliary losses are not included. Therefore the efficiencies shown in these maps should be interpreted as electromagnetic motor efficiencies.

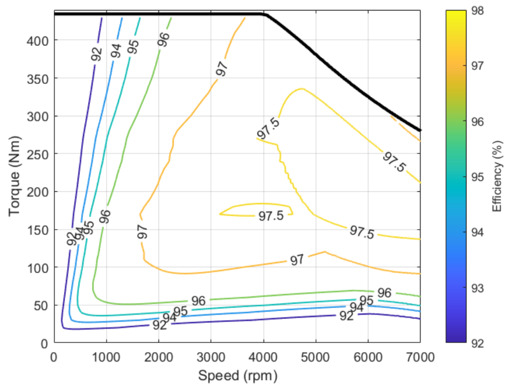

(a) Hybrid PMaSynRM

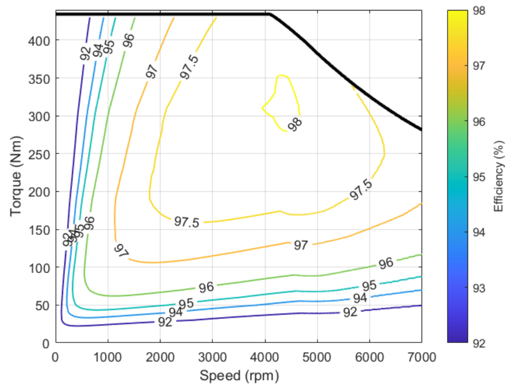

(b) NdFeB VPMSM

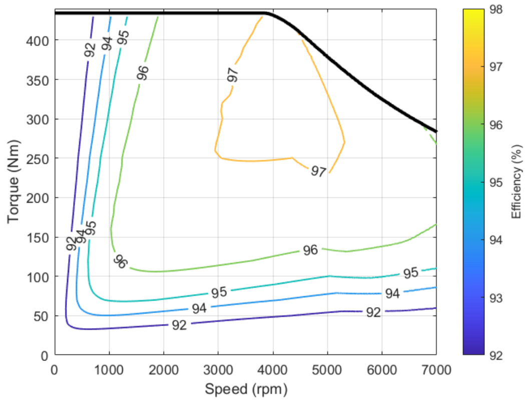

(c) Ferrite spoke PMSM

Figure 4.21: Efficiency maps of the three optimized machines.

From Figure 4.21 it can be observed that all three machines achieve a high maximum electromagnetic efficiency close to 98%. This is because the maps include only the main electromagnetic losses and exclude mechanical and inverter losses.

The NdFeB VPMSM and the hybrid magnet PMaSynRM both show a wide high-efficiency region over the medium-speed and medium-to-high torque range. The ferrite spoke PMSM also reaches high efficiency but its high-efficiency region is more limited at medium-speed and high-torque range because of its larger core losses especially eddy current loss.

At low torque and low speed, the efficiency of all three machines decreases. This is because the mechanical output power is small in this region, so even moderate losses can cause a noticeable reduction in efficiency.

Table 4.9 summarizes the relative loss behaviour of the three optimized machines.

Table 4.9: Comparison of electromagnetic losses for the three optimized machines.

Loss component	**Hybrid PMaSynRM**	**Ferrite Spoke PMSM**	**NdFeB VPMSM**
Copper loss	High	Low	Low
Hysteresis loss	Moderate	High	Low
Eddy current loss	Low	High	Moderate
Total loss	Moderate	High	Low

4.8 Demagnetization Studies

In this thesis, demagnetization studies were performed for the magnets of all three motor designs: the hybrid-magnet PMaSynRM, the ferrite spoke PMSM, and the NdFeB VPMSM reference machine. The analysis was carried out in Ansys Maxwell 2D at three magnet temperatures: $-40°\text{C}$, $20°\text{C}$ and $120°\text{C}$. These temperatures were selected in order to evaluate the magnet robustness over a wide operating-temperature range. Since the demagnetization characteristics of permanent magnets are strongly dependent on temperature the same fault condition can lead to different demagnetization behaviour at different temperatures.

The demagnetization condition considered in this thesis is a three-phase short circuit initiated from the MTPA operating point at maximum torque and base speed just before the machine enters the field-weakening region. This operating point was selected because it represents a severe demagnetization case and in previous work [4], it has been identified as the point where maximum i_d current is generated during short circuit which plays a prominent role in producing demagnetizing fields. A short circuit current plot for PMaSynRM is shown in Figure A.3 of Appendix A.

The demagnetization behaviour was evaluated using the *Demag Coef* quantity available in Ansys Maxwell 2D. The demagnetization coefficient is a measure of the remaining magnet strength after the demagnetizing event. It can be interpreted as

$$\text{Demag Coef} = \frac{B_{r,\text{after}}}{B_{r,\text{initial}}}, \tag{4.4}$$

Here, $B_{r,\text{initial}}$ is the original remanent flux density of the magnet, and $B_{r,\text{after}}$ is the remaining remanent flux density after the demagnetizing condition. A demagnetization coefficient close to unity indicates that the magnet has not suffered significant demagnetization. A lower value indicates that part of the magnet has lost remanence.

The simulation was continued for a sufficiently long time after the short-circuit event so that the final demagnetized state of the magnets could be observed. This is important because the most critical magnet regions may not be identified correctly if the result is evaluated too early during the transient.

The following subsections present the demagnetization results for each motor topology.

4.8.1 Demagnetization Study of the NdFeB VPMSM

The demagnetization coefficient results for the NdFeB VPMSM are shown in Figures 4.22 - 4.24.

Figure 4.22: Demagnetization coefficient distribution of the NdFeB VPMSM after the three-phase short-circuit demagnetization study at $-40°C$.

Figure 4.23: Demagnetization coefficient distribution of the NdFeB VPMSM after the three-phase short-circuit demagnetization study at $20°C$.

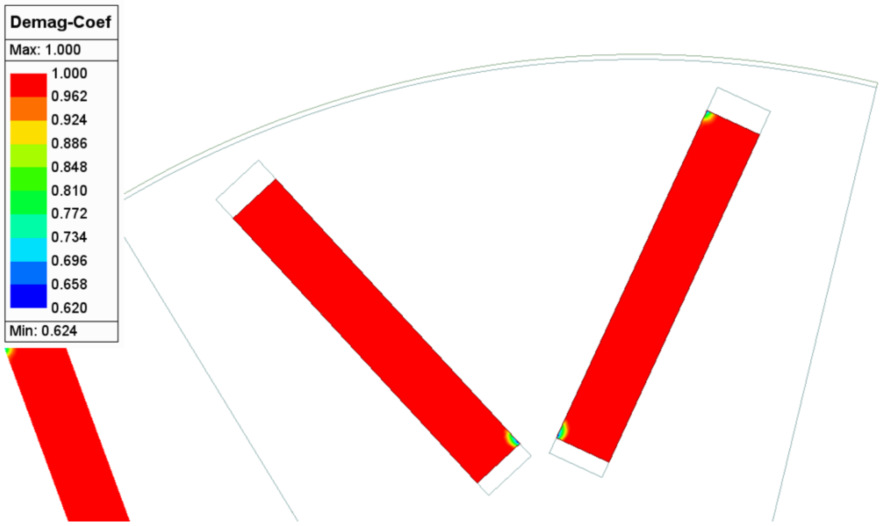

Figure 4.24: Demagnetization coefficient distribution of the NdFeB VPMSM after the three-phase short-circuit demagnetization study at 120°C.

At −40°C, the minimum demagnetization coefficient is approximately 0.973, while most of the magnet region remains close to unity. This indicates that the NdFeB magnets are not significantly demagnetized at low temperature.

At 20°C, the minimum demagnetization coefficient is approximately 0.976. The result is very similar to the −40°C case and the magnets remain almost completely undemagnetized. Only small local regions near the magnet edges show a slight reduction in the demagnetization coefficient.

The most critical result is obtained at 120°C. In this case, the minimum demagnetization coefficient decreases to approximately 0.624. Although most of the magnet body still remains close to unity, small localized regions near the magnet corners show a clear reduction in the demagnetization coefficient. This indicates that partial irreversible demagnetization occurs at high temperature under the short-circuit condition.

Therefore the NdFeB VPMSM is safe at low and room temperature for the short circuit condition but high-temperature short-circuit represents the critical demagnetization case for this design.

4.8.2 Demagnetization Study of the Hybrid-Magnet PMaSynRM

The hybrid PMaSynRM contains two different magnet materials. The magnets in the inner flux-barrier layer are made of NdFeB, while the magnets in the two outer flux-barrier layers are made of ferrite. Therefore, the demagnetization study is important because the two magnet materials have different temperature-dependent demagnetization characteristics.

Figures 4.25–4.27 show the demagnetization coefficient distribution of the hybrid

PMaSynRM at the three temperatures.

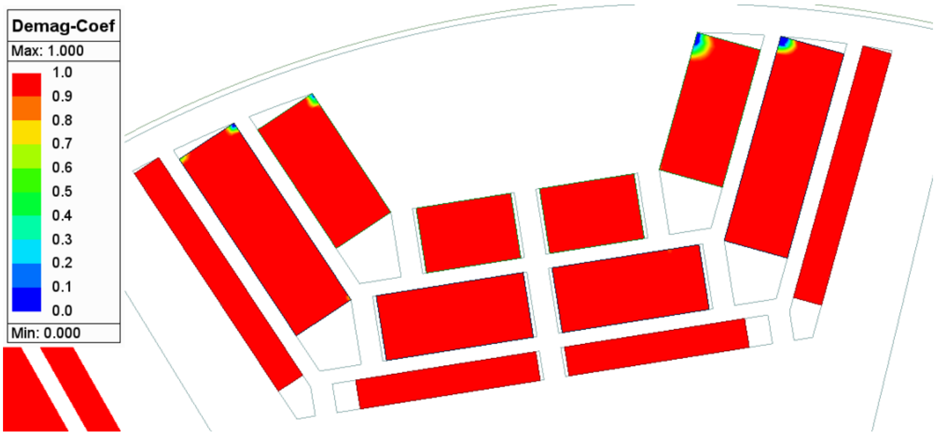

Figure 4.25: Demagnetization coefficient distribution of the hybrid-magnet PMaSynRM after the three-phase short-circuit demagnetization study at −40°C.

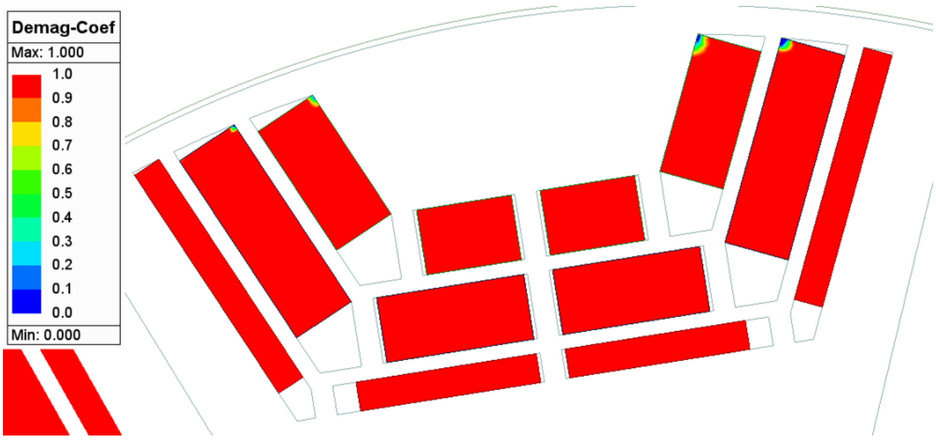

Figure 4.26: Demagnetization coefficient distribution of the hybrid-magnet PMaSynRM after the three-phase short-circuit demagnetization study at 20°C.

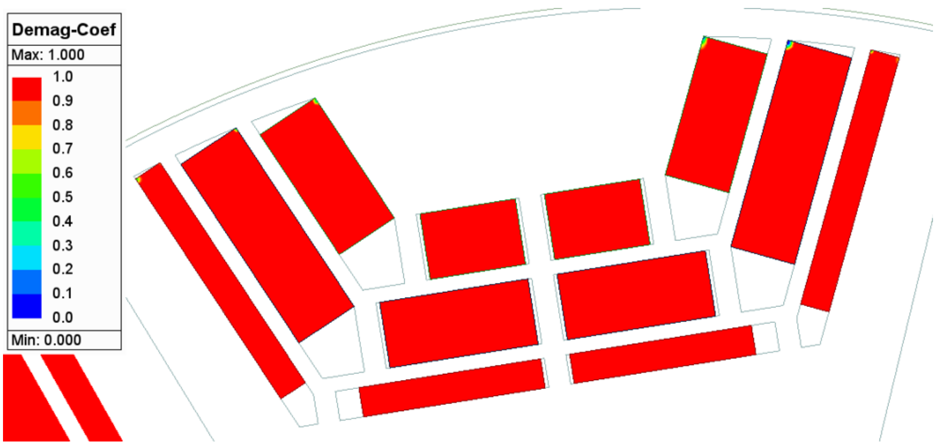

Figure 4.27: Demagnetization coefficient distribution of the hybrid-magnet PMaSynRM after the three-phase short-circuit demagnetization study at 120°C.

From Figures 4.25–4.27, it can be observed that most of the magnet regions remain close to a demagnetization coefficient of unity. This means that the majority of both the NdFeB and ferrite magnets retain their original remanence after the short-circuit event.

At $-40°$C, the localized demagnetized regions are more visible near the outer ferrite magnet corners. This behaviour is reasonable for ferrite magnets since ferrite intrinsic coercivity decreases at lower temperature.

At 20°C, the demagnetization pattern is similar, but the affected regions remain very localized. The main magnet bodies remain almost fully magnetized and only small corner regions show a reduction in the demagnetization coefficient.

At 120°C, the ferrite magnets remain largely safe because the intrinsic coercivity of ferrite magnets generally improves with increasing temperature. Although NdFeB magnets are usually more vulnerable at elevated temperature due to the reduction in intrinsic coercivity, the inner NdFeB magnets in this design remain close to a demagnetization coefficient of unity. This suggests that the inner NdFeB layer is sufficiently protected from the worst demagnetizing field by the Ferrite Magnets.

Therefore, the demagnetization performance of the hybrid PMaSynRM is acceptable, although the outer ferrite magnet corners should be considered critical regions for future designs. The most critical regions are located near the corners and edges of the outer ferrite magnets. Also, the outer ferrite magnets are located closer to the air-gap region and are therefore more directly exposed to the armature-reaction field.

4.8.3 Demagnetization Study of the Ferrite Spoke PMSM

Ferrite magnets are more vulnerable to demagnetization at low temperature because their intrinsic coercivity decreases as temperature is reduced. Figures 4.28-4.30 show the demagnetization coefficient distribution of the ferrite spoke PMSM at the three temperatures.

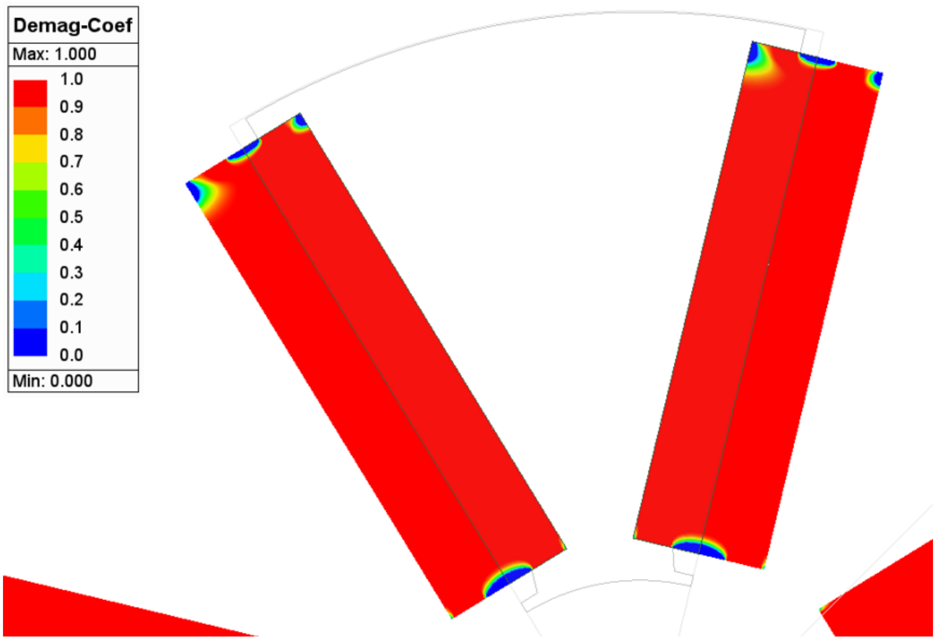

Figure 4.28: Demagnetization coefficient distribution of the ferrite spoke PMSM after the three-phase short-circuit demagnetization study at −40°C.

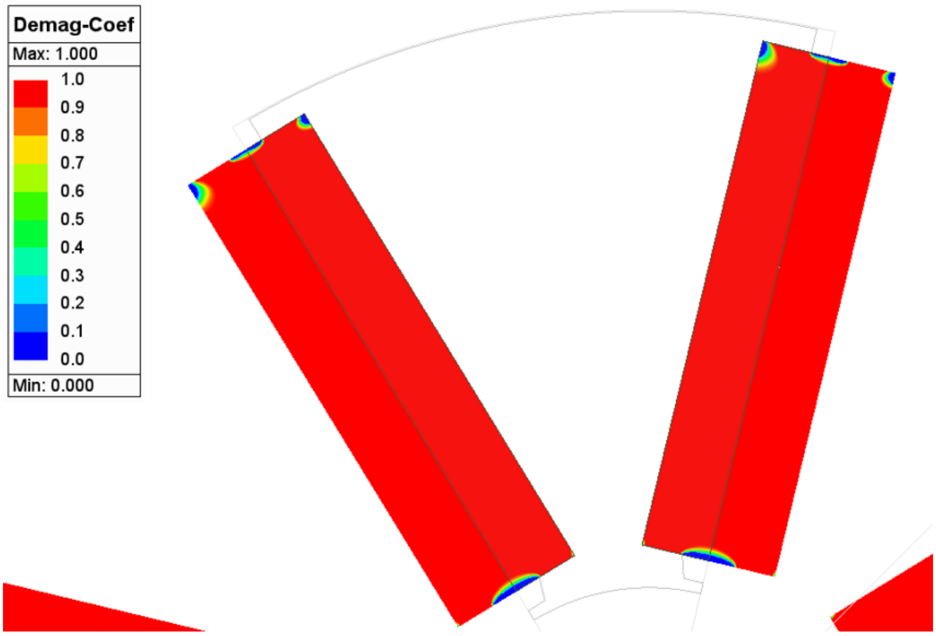

Figure 4.29: Demagnetization coefficient distribution of the ferrite spoke PMSM after the three-phase short-circuit demagnetization study at 20°C.

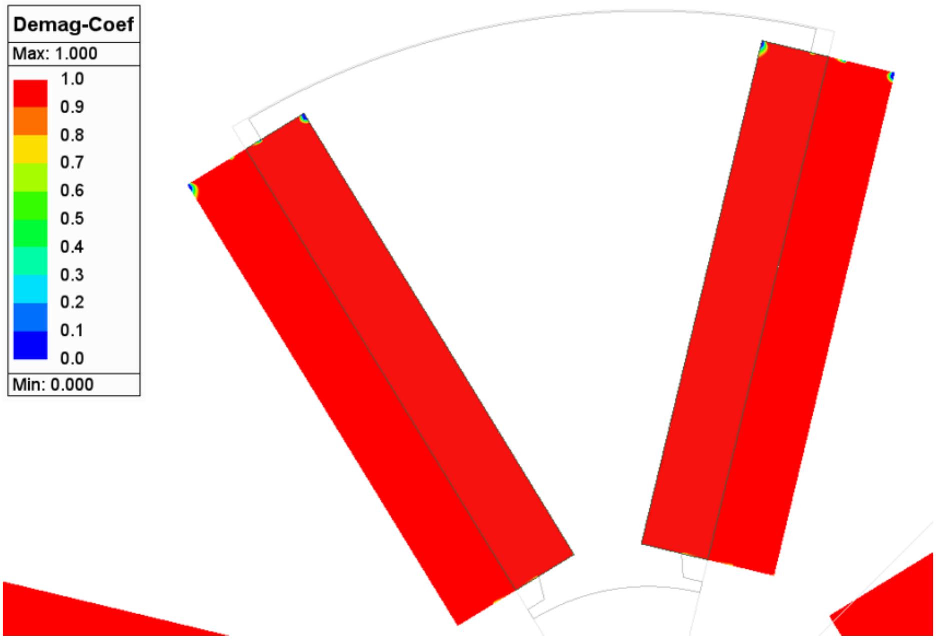

Figure 4.30: Demagnetization coefficient distribution of the ferrite spoke PMSM after the three-phase short-circuit demagnetization study at 120°C.

It can be observed that most of the ferrite magnet volume remains close to a demagnetization coefficient of unity. This means that the main body of the ferrite magnets retains its original remanence after the short-circuit event. However localized demagnetized regions appear near the magnet corners and edges.

The most severe demagnetization occurs at −40°C. At this temperature the demagnetized regions near the magnet edges are larger and more pronounced. This behaviour is expected for ferrite magnets because their intrinsic coercivity decreases at low temperature making them more susceptible to irreversible demagnetization. Therefore the cold-temperature condition is the most critical demagnetization case for the ferrite spoke PMSM.

At 20°C, the demagnetization is still visible, but the affected regions remain localized mainly near the magnet tips and corners. The bulk of the magnet remains almost fully magnetized.

At 120°C, the demagnetized regions are smaller compared with the low-temperature case. This is because ferrite magnets generally have higher intrinsic coercivity at elevated temperature.

Therefore, the ferrite spoke PMSM can be considered acceptable but the low-temperature corner demagnetization should be treated as the critical case for this topology. Future designs could focus on reducing the local demagnetizing field at the magnet tips by modifying the magnet corner geometry, bridge shape or local flux path around the spoke magnets.

4.9 Magnetic Flux Density at Peak Load

The magnetic flux-density distributions of the three optimized machines at peak torque and base speed are shown in Figure 4.31. This operating point represents the peak-load condition of the traction machine where both the current and magnetic flux are high. The flux-density plots are useful for identifying regions of local saturation in the stator teeth, stator yoke, rotor bridges, ribs and magnet neighbouring regions.

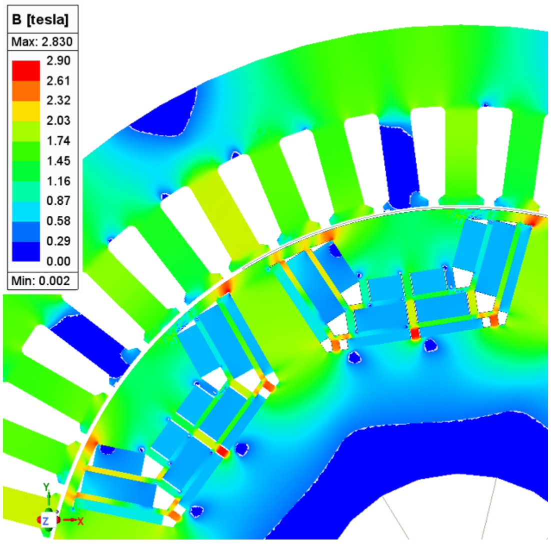

(a) Hybrid PMaSynRM

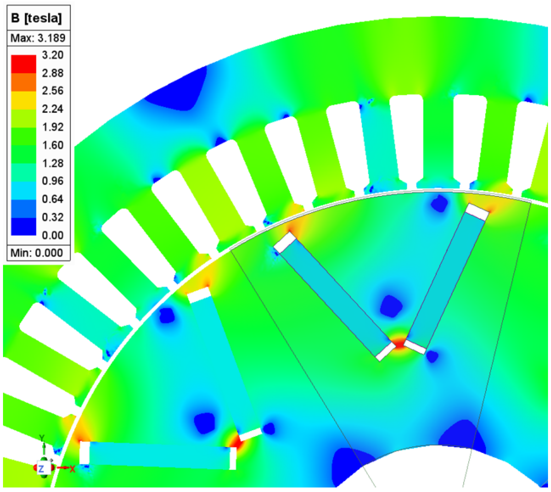

(b) NdFeB VPMSM

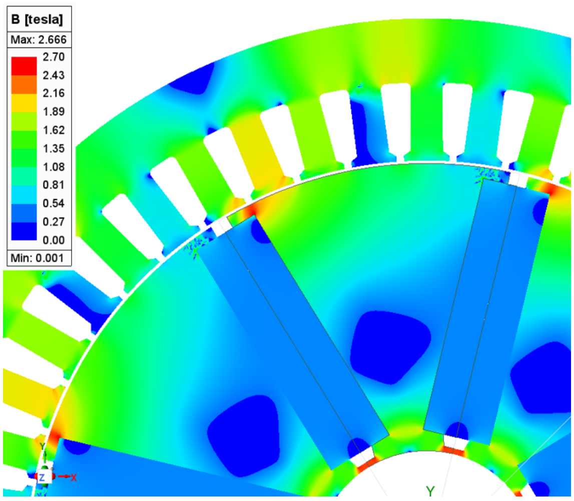

(c) Ferrite spoke PMSM

Figure 4.31: Magnetic flux-density distribution of the three optimized machines at peak torque and base speed.

The maximum local flux-density values observed from the plots are given in Table 4.10.

Table 4.10: Maximum local magnetic flux density at peak torque and base speed.

Machine	**Maximum local flux density $B_{\max}$ (T)**
Ferrite spoke PMSM	2.67
Hybrid PMaSynRM	2.83
NdFeB VPMSM	3.19

From Figure 4.31 and Table 4.10, the highest local flux density is observed in the NdFeB VPMSM, followed by the hybrid PMaSynRM and then the ferrite spoke PMSM.

The NdFeB VPMSM shows the highest local flux density, with a maximum value of approximately 3.19 T. This is expected because the VPMSM uses strong NdFeB magnets and has a relatively small active length. The strong permanent magnet increases the magnetic flux while the rotor structure concentrates the flux through the rotor bridges and stator tooth regions. Therefore theere is localized saturation near magnet tips, rotor bridges and stator tooth-tip areas.

The hybrid PMaSynRM has a maximum local flux density of approximately 2.83 T. The flux-density distribution shows localized high-flux regions around the flux barriers, magnet ends and narrow rotor iron paths. This is expected because the PMaSynRM uses flux barriers and these barriers guide the flux through selected iron paths which can become locally saturated under peak-load operation. However the high-flux regions are mostly localized while the rest of the rotor and stator remain less severely saturated.

The ferrite spoke PMSM shows the lowest maximum local flux density among the three machines with a peak value of approximately 2.67 T. Although the spoke topology is a flux-concentrating structure the machine has a larger active diameter which helps distribute the magnetic flux. This reduces the maximum local flux density compared with the more compact NdFeB VPMSM. Local saturation is still visible near the magnet ends, air-gap side and stator tooth regions but the peak value is lower than in the other two machines.

4.10 Driving Cycle Analysis

4.10.1 City Driving Cycle

The city driving cycle results are presented in this subsection. Since the same driving cycle is applied to all three machines, the required torque and mechanical shaft power profiles are nearly identical for the hybrid PMaSynRM, ferrite spoke PMSM and NdFeB VPMSM. Therefore only one representative torque and power profile is shown in Figure 4.32. The topology-dependent differences are then evaluated using the torque-speed operating trajectories and the drive-cycle loss results.

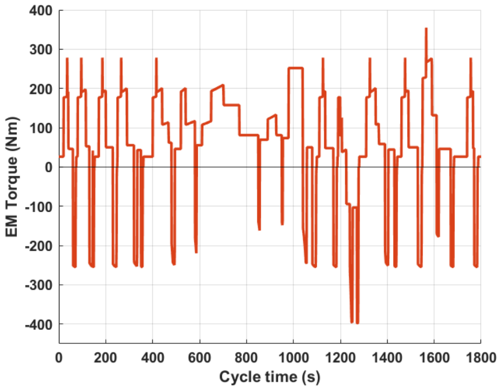

(a) EM torque demand

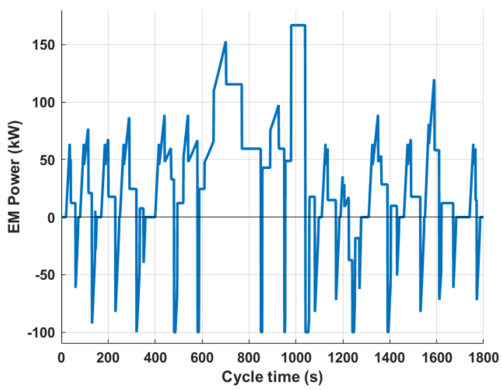

(b) EM power demand

Figure 4.32: Torque and mechanical shaft power profiles during the city driving cycle.

As shown in Figure 4.32, the torque profile contains repeated positive and negative torque events which indicate frequent acceleration and regenerative braking. The power profile also shows several positive power peaks during traction operation and negative power regions during regenerative operation.

The operating trajectories of the three machines on their corresponding torque-speed maps are shown in Figure 4.33.

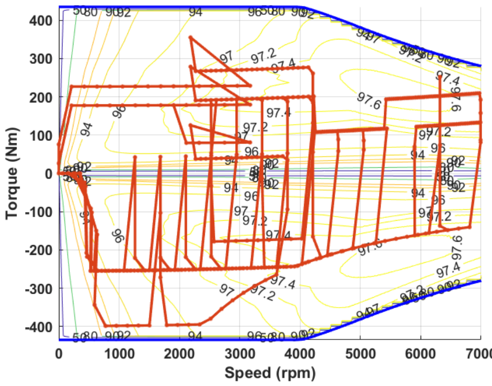

(a) Hybrid PMaSynRM

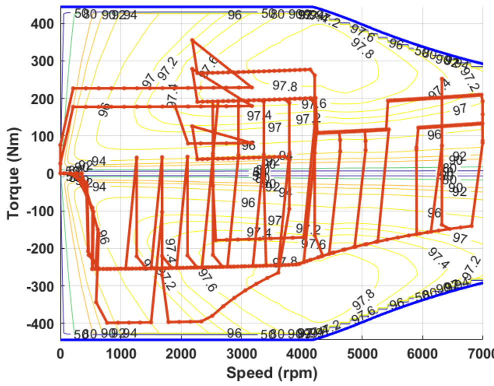

(b) NdFeB VPMSM

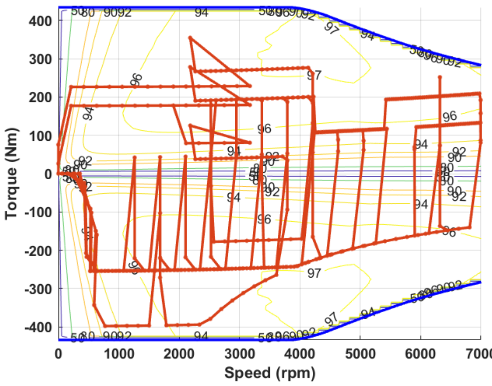

(c) Ferrite spoke PMSM

Figure 4.33: City driving cycle operating trajectories plotted on the torque-speed maps of the three optimized machines.

From Figure 4.33, it can be observed that the city cycle uses a wide range of torque and speed values. Many operating points occur at low and medium speeds which is expected for urban operation.

The energy losses accumulated over the city driving cycle are shown in Figure 4.34. The ferrite spoke PMSM has the highest total energy loss, equal to approximately 1052 Wh. The NdFeB VPMSM has a lower total loss of approximately 801.8 Wh, while the hybrid PMaSynRM gives the lowest total loss of approximately 727.5 Wh.

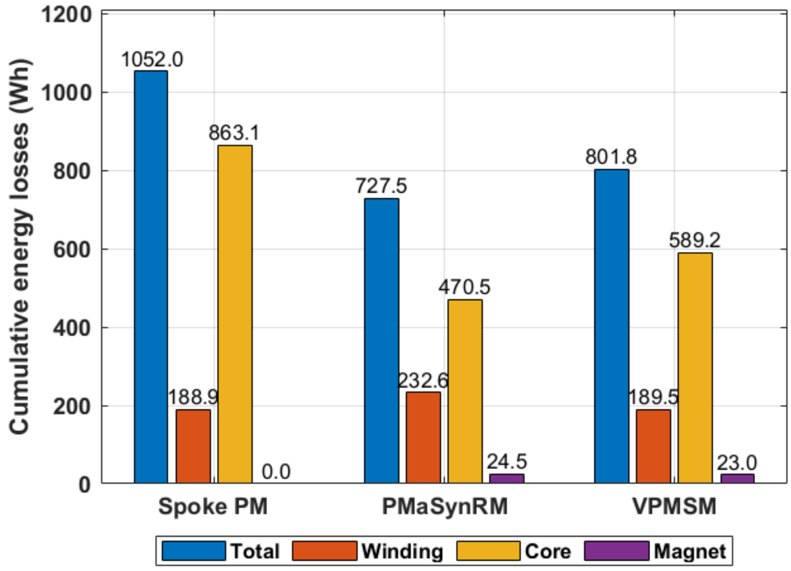

Figure 4.34: Cumulative energy losses of the three optimized machines during the city driving cycle.

The loss breakdown shows that the ferrite spoke PMSM is dominated by core loss. Its core loss is approximately 863.1 Wh, which is much higher than its winding loss of 188.9 Wh.

Although the PMaSynRM has the highest winding loss among the three machines, approximately 232.6 Wh, its core loss is significantly lower than that of the other two machines. This results in the lowest total drive-cycle loss for the city cycle.

The NdFeB VPMSM has a winding loss which is close to that of the spoke PMSM, but its core loss is higher than that of the PMaSynRM. Therefore, even though the VPMSM has strong permanent-magnet torque and favourable copper loss behaviour its city-cycle total loss is slightly higher than that of the PMaSynRM.

The percentage distribution of the city-cycle losses is shown in Figure 4.35.

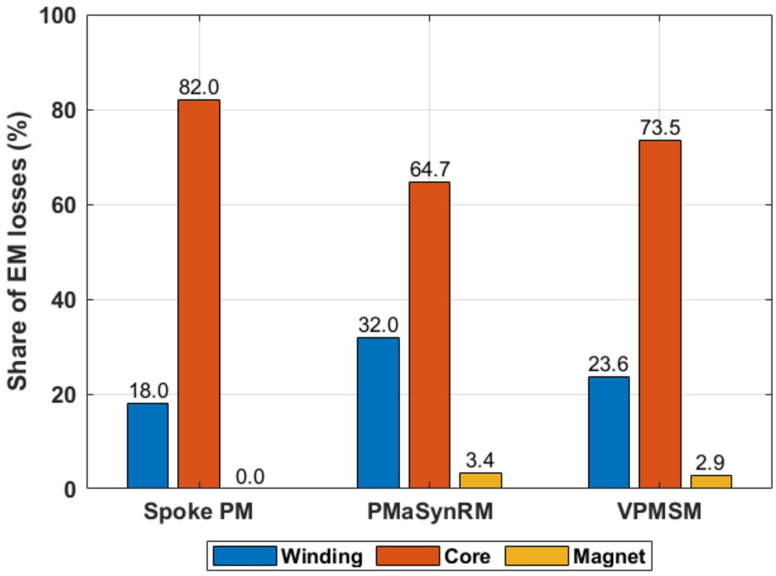

Figure 4.35: Percentage distribution of energy losses during the city driving cycle.

For the ferrite spoke PMSM, about 82% of the total electromagnetic loss comes from core loss, while winding loss contributes approximately 18%. This means that the spoke machine is mainly limited by core losses in the city cycle. The PMaSynRM has a more balanced loss distribution, with approximately 32% winding loss, 64.7% core loss, and 3.4% magnet loss. The NdFeB VPMSM has approximately 23.6% winding loss, 73.5% core loss, and 2.9% magnet loss.

4.10.2 Highway Driving Cycle

The highway driving cycle results are presented in this subsection. As in the city driving cycle case, the same driving cycle is applied to all three machines, so the torque and mechanical shaft power profiles are nearly identical for the hybrid PMaSynRM, ferrite spoke PMSM and NdFeB VPMSM. For this reason, only one torque and power profile is shown in Figure 4.36. The topology-dependent differences are then evaluated using the torque-speed operating trajectories and the drive-cycle loss results.

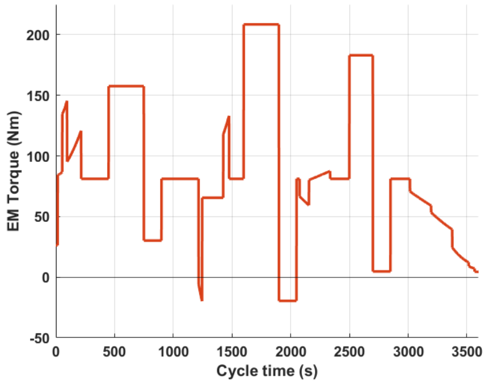

(a) EM torque demand

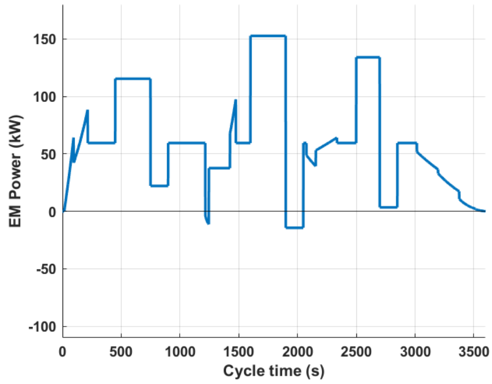

(b) EM power demand

Figure 4.36: Torque and mechanical shaft power profiles during the highway driving cycle.

From Figure 4.36, compared with the city cycle, the highway cycle contains longer periods of positive torque and fewer regenerative braking events. The power demand also contains longer high-power intervals.

The operating trajectories of the three machines on their corresponding torque-speed maps are shown in Figure 4.37.

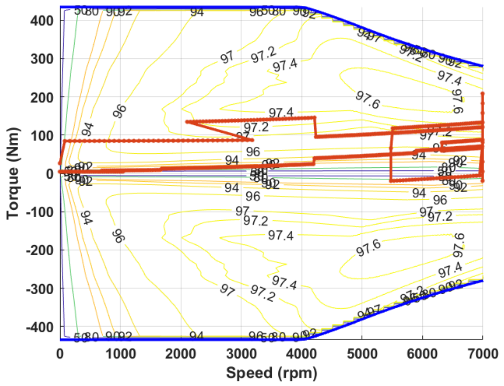

(a) Hybrid PMaSynRM

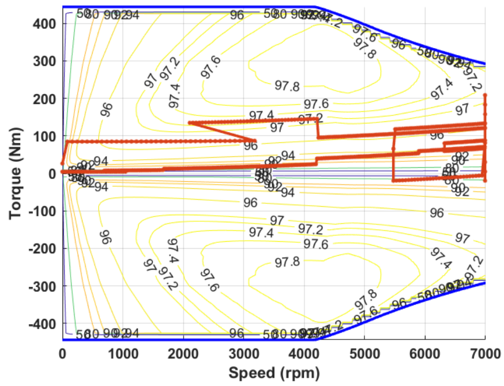

(b) NdFeB VPMSM

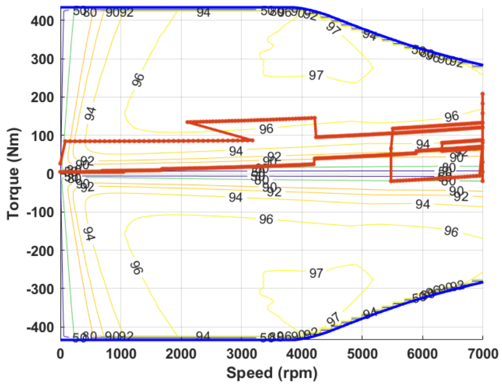

(c) Ferrite spoke PMSM

Figure 4.37: Highway driving cycle operating trajectories plotted on the torque-speed maps of the three optimized machines.

From Figure 4.37, it can be observed that most of the operating points are concentrated in the positive torque region with several operating points at higher motor speeds. This operating pattern makes the highway cycle more sensitive to core losses especially hysteresis and eddy-current losses because these losses increase strongly with motor speed.

The cumulative energy losses over the highway driving cycle are shown in Figure 4.38.

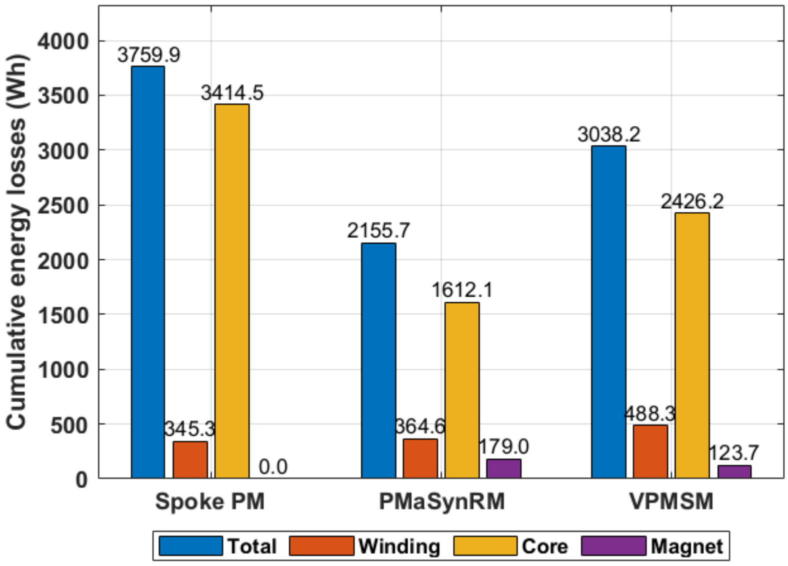

Figure 4.38: Cumulative energy losses of the three optimized machines during the highway driving cycle.

The ferrite spoke PMSM has the highest total energy loss, equal to approximately 3759.9 Wh. The NdFeB VPMSM has a lower total loss of approximately 3038.2 Wh while the hybrid PMaSynRM gives the lowest total loss of approximately 2155.7 Wh. Therefore the PMaSynRM has the lowest total drive-cycle loss followed by the NdFeB VPMSM while the ferrite spoke PMSM has the highest total loss.

The loss breakdown shows that the ferrite spoke PMSM is strongly dominated by core loss. Its core loss is approximately 3414.5 Wh, while its winding loss is only approximately 345.3 Wh.

For PMaSynRM, its winding loss is approximately 364.6 Wh which is close to that of the spoke PMSM, but its core loss is much lower at approximately 1612.1 Wh. The PMaSynRM also has a magnet loss of approximately 179.0 Wh. Even with this magnet loss contribution the lower core loss makes the PMaSynRM the most favourable machine for the highway cycle.

For NdFeB VPMSM, its winding loss is approximately 488.3 Wh and its core loss is approximately 2426.2 Wh. The magnet loss is approximately 123.7 Wh. Although the VPMSM has good torque-per-ampere capability its core loss in the highway cycle is higher than that of the PMaSynRM which increases its total accumulated loss.

The percentage distribution of the highway-cycle losses is shown in Figure 4.39.

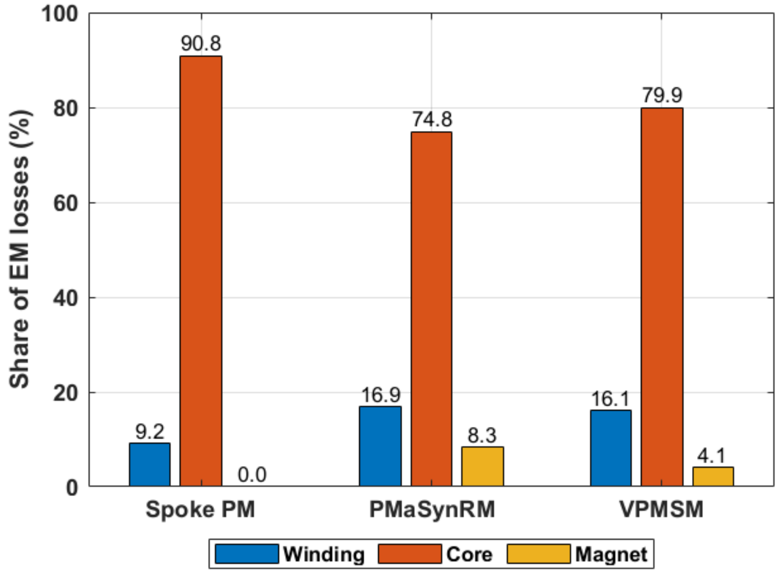

Figure 4.39: Percentage distribution of energy losses during the highway driving cycle.

For the ferrite spoke PMSM, approximately 90.8% of the total electromagnetic loss comes from core loss while winding loss contributes only approximately 9.2%. This shows that the spoke PMSM is strongly core-loss dominated during highway operation. For the PMaSynRM the core loss contributes approximately 74.8%, the winding loss contributes approximately 16.9% and the magnet loss contributes approximately 8.3%. For the NdFeB VPMSM the core loss contributes approximately 79.9%, the winding loss contributes approximately 16.1% and the magnet loss contributes approximately 4.1%.

Table 4.11 compares the average electromagnetic efficiency of the three optimized machines over the two driving cycles.

Table 4.11: Average electromagnetic efficiency of the three machines over the city and highway driving cycles.

Machine	**City driving cycle**	**Highway driving cycle**
Ferrite Spoke PMSM	92.69%	91.63%
Hybrid PMaSynRM	94.11%	93.86%
NdFeB VPMSM	93.67%	92.62%

The hybrid PMaSynRM gives the highest average efficiency in both the city and highway driving cycles. The NdFeB VPMSM gives the second highest average efficiency while the ferrite spoke PMSM gives the lowest average efficiency. The lower average efficiency of the ferrite spoke PMSM is mainly due to its higher core-loss contribution especially during highway operation.

4.11 Comparative Material Cost, Carbon Footprint, and Critical-Material Sustainability Assessment

This section compares the three developed motor topologies from the viewpoint of active material requirement, magnet dependency, raw-material cost, embodied carbon contribution and sustainability. The compared topologies are Spoke type PMSM, VPMSM and PMaSynRM. The material inventory is obtained from the developed ANSYS motor geometries, while the updated cost calculation uses the active-material cost basis reported in [25].

4.11.1 Active material inventory

The active material mass of each component was calculated from the two-dimensional cross-sectional area obtained from the motor geometry and the corresponding stack length. The component volume was first calculated and then multiplied by the material density, as shown in Equation (4.5)

$$V_i = A_i \times L_{\mathrm{stk}} \quad \text{and} \quad m_i = V_i \times \rho_i \tag{4.5}$$

where A_i is the cross-sectional area of material i, L_{stk} is the stack length, V_i is the active volume, ρ_i is the material density, and m_i is the calculated material mass. Table 4.12 shows the detailed mass calculation for each active material in the three motor topologies. The table includes the extracted area, stack length, calculated volume, material density, and resulting mass for rotor steel, stator steel, copper winding, NdFeB magnets, and ferrite magnets.

Table 4.12: Material properties and mass distribution for different motor types

Motor type	Component	Area (cm^2)	L_{Stack} (m)	Volume (cm^3)	Density (kg/m^3)	Mass (kg)
Spoke PMSM	Rotor steel	232.980	0.235	5475.03	7650	41.88
	Stator steel	246.862	0.235	5801.26	7650	44.38
	Copper winding	25.805	0.235	606.42	8933	5.42
	Ferrite magnet	105.012	0.235	2467.78	5000	12.34
VPMSM	Rotor steel	161.05	0.165	2657.33	7650	20.33
	Stator steel	174.022	0.165	2871.36	7650	21.97
	Copper winding	20.542	0.165	338.94	8933	3.03
	NdFeB magnet	21.931	0.165	361.86	7500	2.71
PMaSynRM	Rotor steel	173.697	0.250	4342.43	7650	33.22
	Stator steel	139.321	0.250	3483.03	7650	26.65
	Copper winding	20.542	0.250	513.55	8933	4.59
	NdFeB magnet	9.727	0.250	243.18	7500	1.82
	Ferrite magnet	29.569	0.250	739.23	5000	3.70

The component masses calculated in Table 4.12 are then grouped by motor topology in Figure 4.40 to provide a direct comparison of the active material distribution. In this summary, rotor and stator steel are also combined as the total electrical steel mass, and the total active mass is calculated by summing all active components. Based on the mass calculation, the Spoke PMSM has the highest total active mass of 104.02 kg followed by the PMaSynRM with 69.98 kg, while the VPMSM has the lowest total active mass of 48.04 kg. The lower mass of the VPMSM is mainly due to its compact NdFeB-based rotor structure. In contrast, the Spoke PMSM has a higher active mass because of its larger electrical steel, copper winding and ferrite magnet content. Although the Spoke PMSM uses the highest total magnet mass of 12.34 kg, its magnet is completely ferrite-based. Therefore, it avoids NdFeB-related rare-earth dependency. The VPMSM uses the lowest total magnet mass of 2.71 kg, but the complete magnet mass is NdFeB, giving it the highest critical-material dependency. The PMaSynRM uses both NdFeB and ferrite magnets, with 1.82 kg of NdFeB and 3.70 kg of ferrite. Compared with the VPMSM, the PMaSynRM reduces NdFeB usage from 2.71 kg to 1.82 kg, corresponding to approximately 32.8% reduction in NdFeB mass. Therefore the PMaSynRM provides a compromise between compactness, performance and rare-earth reduction.

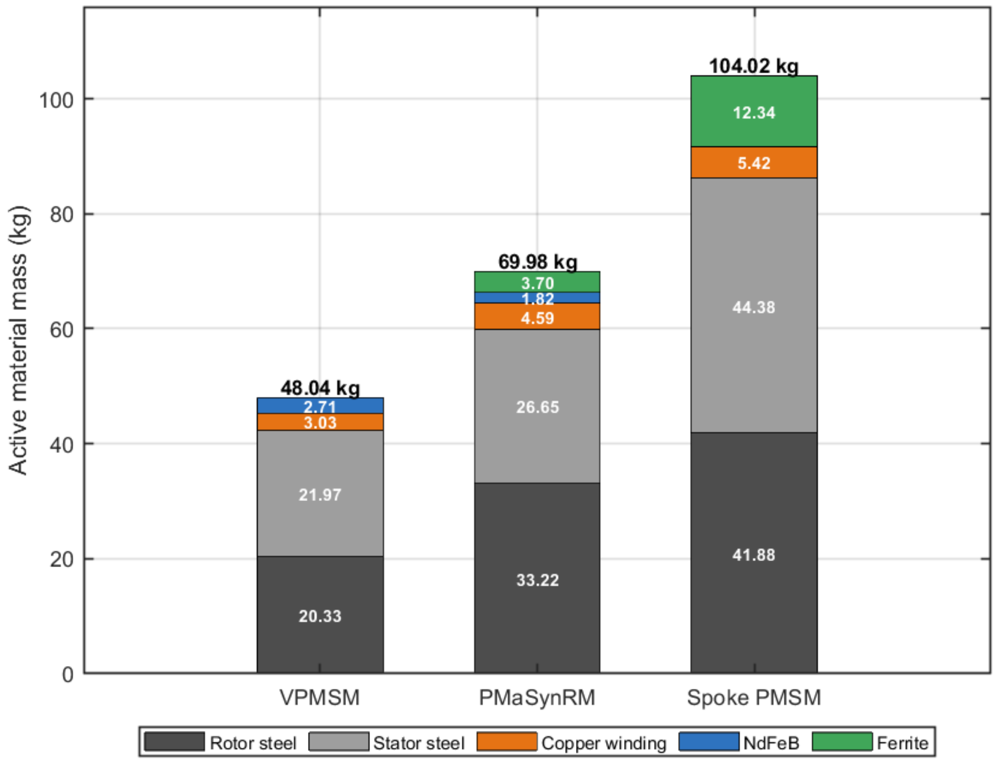

Figure 4.40: Active material mass comparison of the studied motor topologies showing rotor steel, stator steel, copper winding, NdFeB magnet and ferrite magnet contributions.

4.11.2 Raw-material cost comparison

The raw-material cost was calculated using the component masses from Table 4.12 and the unit cost values derived from [25]. The cost of each material was calculated as

$$C_i = m_i \times c_i, \tag{4.6}$$

where C_i is the material cost, m_i is the material mass, and c_i is the unit cost of the material. Using Equation (4.6), the raw-material cost of each topology was calculated as shown in Table 4.13.

Table 4.13: Material cost comparison for different motor types

Motor type	**Electrical steel cost (€)**	**Copper cost (€)**	**NdFeB cost (€)**	**Ferrite cost (€)**	**Total cost (€)**
Spoke PMSM	43.13	30.89	0.00	150.79	224.82
VPMSM	21.15	17.27	428.18	0.00	466.60
PMaSynRM	29.94	26.16	287.56	45.21	388.87

The Spoke PMSM has the lowest total raw-material cost because it avoids NdFeB magnets completely. The VPMSM has the lowest active material mass, but it becomes the most expensive topology due to the high cost contribution of NdFeB magnets. The PMaSynRM has a higher total active mass than the VPMSM, but its reduced NdFeB content lowers the total cost compared with the VPMSM.

4.11.3 Embodied carbon emission

The embodied carbon emission was estimated to compare the manufacturing-stage environmental burden associated with the active materials used in the three motor topologies. This calculation is important because a motor with lower mass does not always have the lowest sustainability impact and the result also depends on the type of material used, especially when rare-earth magnets are involved. Therefore, electrical steel, copper winding, NdFeB magnets, and ferrite magnets are all included in the embodied CO_2e calculation. The carbon emission of each material is calculated as follows

$$CE_i = m_i \times CF_i \tag{4.7}$$

where CE_i is the carbon emission of material i, m_i is the material mass in kg, and CF_i is the carbon-emission factor in kg of CO_2e/kg. The emission factors for the materials are considered as follows: electrical steel has an emission factor of 3.12 kg of CO_2e/kg, copper winding has 6.70 kg of CO_2e/kg, NdFeB magnet has 23.40 kg of CO_2e/kg, and ferrite magnet has 4.10 kg of CO_2e/kg [26] [27] [28]. Using these factors together with the material masses calculated earlier, the embodied CO_2e values for the three motors are summarized in Table 4.14

Motor type	**Steel CO_2e (kg)**	**Copper CO_2e (kg)**	**NdFeB CO_2e (kg)**	**Ferrite CO_2e (kg)**	**Total CO_2e (kg)**	**kg CO_2e/ kg active mass**
Spoke PMSM	269.13	36.31	0.00	50.59	356.04	3.42
VPMSM	131.98	20.30	63.41	0.00	215.69	4.49
PMaSynRM	186.79	30.75	42.59	15.17	275.31	3.93

Table 4.14: CO_2e emissions for different motor types

The VPMSM gives the lowest total embodied CO_2e, mainly because it has the lowest total active material mass. However, it also has the highest kg of CO_2e per kg of active mass because its magnet is fully NdFeB-based. The Spoke PMSM has the highest total embodied CO_2e due to its larger electrical steel and ferrite mass, but it avoids NdFeB completely and therefore has lower rare-earth dependency. The PMaSynRM gives an intermediate result, reducing NdFeB mass compared with the VPMSM while retaining partial rare-earth magnet excitation. Therefore, the embodied carbon result should be interpreted together with raw-material cost, magnet dependency, and supply-chain risk rather than used as the only sustainability indicator.

The emission factors used in this work are literature-based cradle-to-gate estimates. Since reported carbon-emission factors vary with production route, geographical energy mix, recycled content and database assumptions, the calculated values should be interpreted as approximate embodied CO_2e indicators rather than exact manufacturing emissions. The selected factors are, however, within the range of values reported for electrical machine materials in recent LCA studies.

4.11.4 Rare-earth dependency and global supply-chain dominance

In addition to the material mass, cost and embodied carbon emission, the rare-earth dependency of each topology is an important sustainability indicator. This is because NdFeB magnets depend on rare-earth elements and are therefore more exposed to critical-material availability, price fluctuation, and geopolitical supply-chain risk. The magnet inventory of the three machines is summarized in Figure 4.41

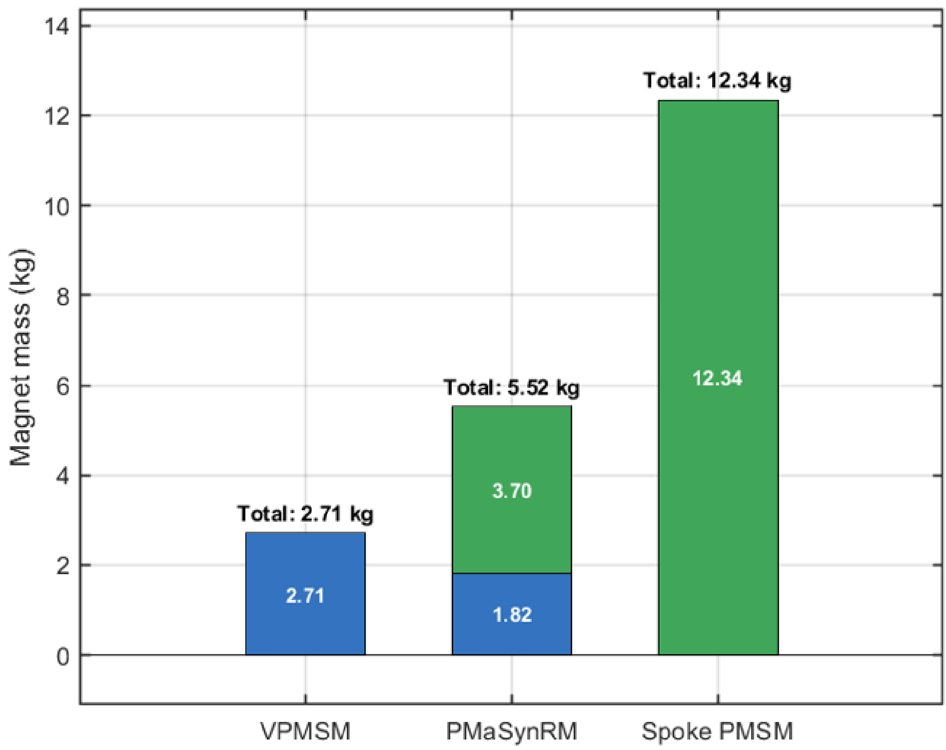

Figure 4.41: NdFeB and ferrite magnet mass comparison of the studied motor topologies.

The Spoke PMSM uses the highest total magnet mass, but it is completely ferrite-based and therefore avoids NdFeB-related rare-earth dependency. The VPMSM uses the lowest total magnet mass, but the entire magnet mass is NdFeB, making it the most critical-material-sensitive topology. The PMaSynRM reduces the NdFeB mass from 2.71 kg in the VPMSM to 1.82 kg, corresponding to approximately 32.8% reduction in NdFeB usage. Therefore, the PMaSynRM provides a compromise between rare-earth reduction and performance.

The motor-level NdFeB usage can be linked to both rare-earth reserve distribution and supply-chain concentration. Figure 4.42 shows that rare-earth reserves are distributed across several countries, with China holding the largest share, followed by Brazil, India, Australia, Russia, and others. However, Figure 4.43 shows that the magnet rare-earth supply chain is much more concentrated than the reserve base. In 2024, China dominated light rare-earth mining, rare-earth refining, and permanent magnet manufacturing, with particularly high shares in refining and magnet production.

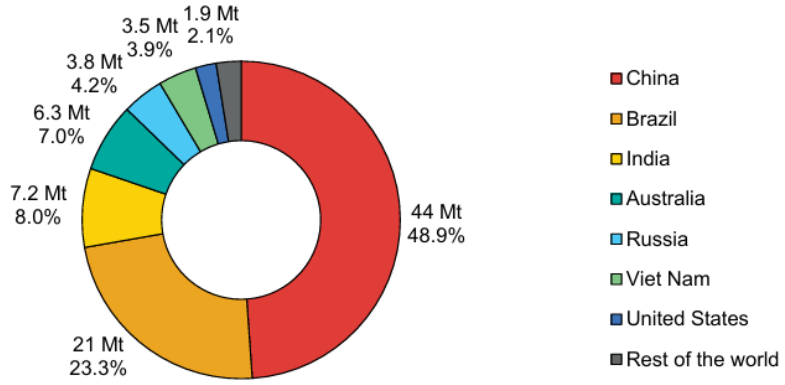

Figure 4.42: Geographical distribution of rare earth reserves, 2026 [29]

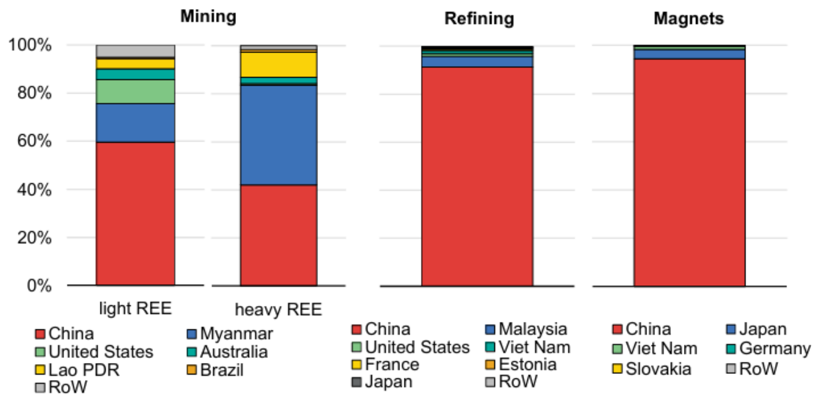

Figure 4.43: Share of global supply of magnet rare earths and magnet manufacturing, 2024 [29]

Therefore, the VPMSM and PMaSynRM are exposed not only to NdFeB material dependency, but also to a concentrated global processing and magnet-manufacturing chain. In contrast, the Spoke PMSM avoids NdFeB completely and is less sensitive to rare-earth supply disruption, price volatility, and geopolitical risk.

4.11.5 Use phase performance

The material-based sustainability comparison presented above gives useful information about active material mass, raw-material cost, embodied CO_2e , and rare-earth dependency, but the final sustainability position of a traction motor also depends on its use-phase performance. For EV truck applications, even small differences in motor efficiency can accumulate over repeated city and highway operation, so the drive-cycle efficiency results from Section 4.10 are included in the sustainability interpretation. A representative mission profile is considered by weighting the city and highway efficiencies according to the selected use condition, for example 30% city and 70% highway operation, using $\eta_{\mathrm{w}} = 0.3\eta_{\mathrm{city}} + 0.7\eta_{\mathrm{highway}}$. Based on this use-phase weighting, the PMaSynRM gives the highest weighted drive-cycle efficiency, while the VPMSM remains the most compact topology with the lowest active-material embodied CO_2e, and the Spoke PMSM remains the lowest-cost and rare-earth-free option. However, the Spoke PMSM also has the highest active material mass and the lowest use-phase efficiency, making it less favourable for high-utilization EV-truck operation. Therefore, when use-phase efficiency is considered together with material mass, embodied CO_2e, cost, and NdFeB dependency, the PMaSynRM provides the most balanced sustainability position for the considered EV-truck use case. The VPMSM is preferable when compactness and low material-side CO_2e are prioritized, whereas the Spoke PMSM is preferable when low cost and complete rare-earth independence are the dominant requirements.

4.11.6 Final sustainability implication

The final sustainability comparison is based on active material mass, raw-material cost, embodied CO_2e, NdFeB dependency, supply-chain risk, and use-phase drive-cycle performance. The material-side trade-offs are summarized in Figure 4.44, where the x-axis represents active mass, the y-axis represents cost, the bubble size represents embodied CO_2e, and the colour indicates NdFeB magnet mass. Figure 4.44 shows that the VPMSM has the lowest active mass and the lowest active-material CO_2e, but it has the highest raw-material cost and the highest NdFeB dependency. The Spoke PMSM has the highest active mass and embodied CO_2e, but it has the lowest raw-material cost and completely avoids NdFeB magnets, making it the strongest option from the viewpoint of rare-earth independence and supply-chain resilience. The PMaSynRM lies between the two material-side extremes by reducing NdFeB usage and cost compared with the VPMSM while retaining partial rare-earth magnet assistance.

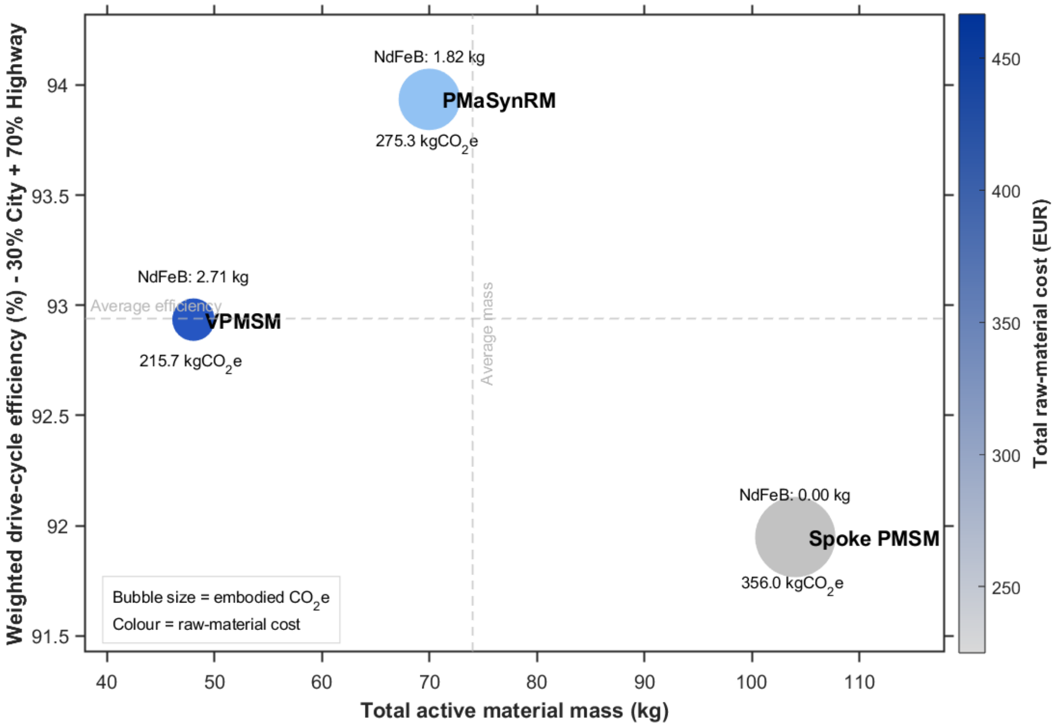

Figure 4.44: Sustainability positioning of the studied motor topologies based on active material mass, raw-material cost, embodied CO_2e and NdFeB dependency. Bubble size represents total embodied CO_2e, and the right-side scale indicates raw material cost

However, the sustainability positioning changes when the use phase is included. For EV truck applications, the motor operates repeatedly over city and highway driving conditions, so drive-cycle efficiency becomes an important sustainability indicator. The use-phase comparison shows that the PMaSynRM gives the highest weighted drive-cycle efficiency, whereas the Spoke PMSM gives the lowest efficiency because of its higher active material mass and higher drive-cycle losses. Therefore, the Spoke PMSM should not be considered the overall most sustainable topology for high-utilization EV truck operation, even though it is the most favourable option in terms of cost and rare-earth independence. Instead, the Spoke PMSM is most suitable when low cost, material availability, and complete avoidance of NdFeB magnets are prioritized. The VPMSM is favourable when compactness and low active-material CO_2e are the dominant requirements, but it has the highest raw-material cost and supply-chain risk due to its NdFeB content. The PMaSynRM provides the best overall compromise for the considered EV truck use case because it combines the highest use-phase efficiency with moderate active mass, moderate embodied CO_2e, reduced NdFeB usage compared with the VPMSM, and lower cost than the VPMSM. Therefore, when both material-side and use-phase indicators are considered, the PMaSynRM is the most balanced sustainability option among the studied topologies.

5

Controller Design and Implementation

5.1 Electric Machine Plant Setup

5.1.1 Electric Machine Plant Implementation

The modeling and control framework was implemented in MATLAB/Simulink using data from ANSYS Maxwell 2D Simulation setup as reduced order model (ROM). The data files of phase currents, phase voltages, phase flux linkages, rotor position, and torque were available for a discrete operating grid. In the implementation, the main operating points selected are i) Id = -100A, Iq = 200A and ii) Id = -350A, Iq = 100A. Other operating points near the main operating points were also considered, since currents do not remain constant. The rotor angle sweeps over $0 < \theta_e < 2\pi$ for a total of 200 Electrical Cycles for i) and 400 Electrical Cycles for ii) . For the studied operating point, the mechanical speed was set to 1000 rpm and 6000 rpm. The imported abc-frame quantities were transformed into the synchronous dq-frame using the Park transformation. For example, the implemented expressions for current are

$$i_d = \frac{2}{3}\Big(i_a \cos\theta_e + i_b \cos\Big(\theta_e - \frac{2\pi}{3}\Big) + i_c \cos\Big(\theta_e + \frac{2\pi}{3}\Big)\Big) \tag{5.1}$$

$$i_q = -\frac{2}{3}\Big(i_a \sin\theta_e + i_b \sin\Big(\theta_e - \frac{2\pi}{3}\Big) + i_c \sin\Big(\theta_e + \frac{2\pi}{3}\Big)\Big) \tag{5.2}$$

and similar transformation is done for ψ_d, ψ_q, vd and vq. After interpolation over the rotor-angle grid, the ROM maps for ψ_d, ψ_q, T_e were stored in mat file. Also, $\frac{\partial\psi_d}{\partial i_d}$, $\frac{\partial\psi_d}{\partial i_q}$, $\frac{\partial\psi_d}{\partial\theta_e}$, $\frac{\partial\psi_q}{\partial i_d}$, $\frac{\partial\psi_q}{\partial i_q}$ and $\frac{\partial\psi_q}{\partial\theta_e}$ were computed using numerical gradients.

5.1.1.1 Plant Model used in Simulink

The standard PMSM voltage equations in the rotating dq frame are

$$v_d = R_s i_d + \frac{d\psi_d}{dt} - \omega_e \psi_q \tag{5.3}$$

$$v_q = R_s i_q + \frac{d\psi_q}{dt} + \omega_e \psi_d \tag{5.4}$$

where the flux linkages ψ_d and ψ_q are treated as nonlinear functions of current and electrical angle

$$\psi_d = \psi_d(i_d, i_q, \theta_e) \tag{5.5}$$

$$\psi_q = \psi_q(i_d, i_q, \theta_e) \tag{5.6}$$

Since ψ_d and ψ_q are functions of i_d, i_q, and θ_e their time derivatives must be computed using the chain rule given by

$$\frac{d\psi_d}{dt} = \frac{\partial\psi_d}{\partial i_d}\dot{i}_d + \frac{\partial\psi_d}{\partial i_q}\dot{i}_q + \omega_e\frac{\partial\psi_d}{\partial\theta_e} \tag{5.7}$$

Similarly

$$\frac{d\psi_q}{dt} = \frac{\partial\psi_q}{\partial i_d}\dot{i}_d + \frac{\partial\psi_q}{\partial i_q}\dot{i}_q + \omega_e\frac{\partial\psi_q}{\partial\theta_e} \tag{5.8}$$

Substituting (5.7) into (5.3) gives

$$v_d = R_s i_d + \frac{\partial \psi_d}{\partial i_d}\dot{i}_d + \frac{\partial \psi_d}{\partial i_q}\dot{i}_q + \omega_e \frac{\partial \psi_d}{\partial \theta_e} - \omega_e \psi_q \tag{5.9}$$

Rearranging gives

$$\frac{\partial \psi_d}{\partial i_d}\dot{i}_d + \frac{\partial \psi_d}{\partial i_q}\dot{i}_q = v_d - R_s i_d + \omega_e \psi_q - \omega_e \frac{\partial \psi_d}{\partial \theta_e} \tag{5.10}$$

Now substituting (5.8) into (5.4) gives

$$v_q = R_s i_q + \frac{\partial \psi_q}{\partial i_d}\dot{i}_d + \frac{\partial \psi_q}{\partial i_q}\dot{i}_q + \omega_e \frac{\partial \psi_q}{\partial \theta_e} + \omega_e \psi_d \tag{5.11}$$

Rearranging gives

$$\frac{\partial \psi_q}{\partial i_d}\dot{i}_d + \frac{\partial \psi_q}{\partial i_q}\dot{i}_q = v_q - R_s i_q - \omega_e \psi_d - \omega_e \frac{\partial \psi_q}{\partial \theta_e} \tag{5.12}$$

Equations (5.10) and (5.12) can be written in matrix form as

$$\underbrace{\begin{bmatrix} \frac{\partial \psi_d}{\partial i_d} & \frac{\partial \psi_d}{\partial i_q} \\ \frac{\partial \psi_q}{\partial i_d} & \frac{\partial \psi_q}{\partial i_q} \end{bmatrix}}_{\mathbf{M}} \begin{bmatrix} \dot{i}_d \\ \dot{i}_q \end{bmatrix} = \begin{bmatrix} v_d - R_s i_d + \omega_e \psi_q - \omega_e \frac{\partial \psi_d}{\partial \theta_e} \\ v_q - R_s i_q - \omega_e \psi_d - \omega_e \frac{\partial \psi_q}{\partial \theta_e} \end{bmatrix} \tag{5.13}$$

Therefore

$$\begin{bmatrix} \dot{i}_d \\ \dot{i}_q \end{bmatrix} = \mathbf{M}^{-1} \begin{bmatrix} v_d - R_s i_d + \omega_e \psi_q - \omega_e \frac{\partial \psi_d}{\partial \theta_e} \\ v_q - R_s i_q - \omega_e \psi_d - \omega_e \frac{\partial \psi_q}{\partial \theta_e} \end{bmatrix} \tag{5.14}$$

Equation(5.14) is used as our Plant Model in Simulink

5.1.1.2 Linearisation

A nonlinear model describes the motor accurately but it is difficult to use it directly in controllers such as LQR or LQI that require a linear state-space model. So to make it work, instead of studying the whole nonlinear system everywhere, we study how the system behaves very close to one particular operating point. Near that operating point a nonlinear system can often be approximated by a linear one [30]. If the motor operates at the following point

$$i_d = i_{d0}, \qquad i_q = i_{q0},$$

with corresponding input voltages

$$v_d = v_{d0}, \qquad v_q = v_{q0}$$

then since the motor is angle dependent the operating point must also include the electrical angle

$$\theta_e = \theta_{e0}$$

So the full operating point is

$$(x_0, u_0, \theta_{e0})$$

where

$$x_0 = \begin{bmatrix} i_{d0} \\ i_{q0} \end{bmatrix} \qquad u_0 = \begin{bmatrix} v_{d0} \\ v_{q0} \end{bmatrix}$$

This operating point is the one around which the system will be approximated. After that, the actual states and inputs are written as the operating point values plus small deviations

$$x = x_0 + \delta x \tag{5.15}$$

$$u = u_0 + \delta u \tag{5.16}$$

Here,

$$\delta x = \begin{bmatrix} \delta i_d \\ \delta i_q \end{bmatrix}$$

represents small changes in the currents, and

$$\delta u = \begin{bmatrix} \delta v_d \\ \delta v_q \end{bmatrix}$$

represents small changes in the voltages.
Linearisation assumes that these deviations are not large.

Now the nonlinear system is given by

$$\dot{x} = f(x, u, \theta_e)$$

Now if we substitute

$$x = x_0 + \delta x \qquad u = u_0 + \delta u$$

Then we get

$$\dot{x} = f(x_0 + \delta x,\ u_0 + \delta u,\ \theta_{e0})$$

Now we approximate this non linear function near the operating point. The main idea of linearisation is that a smooth nonlinear function can be approximated near one point by its first-order taylor series expansion [30].

So near the operating point we can get a linear form of the non linear model given by

$$f(x_0 + \delta x,\ u_0 + \delta u,\ \theta_{e0}) \approx f(x_0, u_0, \theta_{e0}) + A\,\delta x + B\,\delta u \tag{5.17}$$

where A and B represent the matrices containing the first order taylor series expansion terms, also called as Jacobians. These matrices tells us how the state derivative changes when the states or inputs are changed slightly around the operating point.

So from (5.17) the linearised model becomes

$$\delta\dot{x} = A\,\delta x + B\,\delta u \tag{5.18}$$

where the matrix A is the Jacobian of the nonlinear function f with respect to the state vector x and the matrix B is the Jacobian of the nonlinear function f with respect to the input vector u evaluated at the operating point:

$$A = \left.\frac{\partial f}{\partial x}\right|_{(x_0,u_0,\theta_{e0})} \tag{5.19}$$

$$B = \left.\frac{\partial f}{\partial u}\right|_{(x_0,u_0,\theta_{e0})} \tag{5.20}$$

If

$$x = \begin{bmatrix} x_1 \\ x_2 \\ \vdots \\ x_n \end{bmatrix}, \qquad f(x,u,\theta_{e0}) = \begin{bmatrix} f_1(x,u,\theta_{e0}) \\ f_2(x,u,\theta_{e0}) \\ \vdots \\ f_n(x,u,\theta_{e0}) \end{bmatrix}$$

then

$$A = \begin{bmatrix} \frac{\partial f_1}{\partial x_1} & \frac{\partial f_1}{\partial x_2} & \cdots & \frac{\partial f_1}{\partial x_n} \\ \frac{\partial f_2}{\partial x_1} & \frac{\partial f_2}{\partial x_2} & \cdots & \frac{\partial f_2}{\partial x_n} \\ \vdots & \vdots & \ddots & \vdots \\ \frac{\partial f_n}{\partial x_1} & \frac{\partial f_n}{\partial x_2} & \cdots & \frac{\partial f_n}{\partial x_n} \end{bmatrix}_{(x_0,u_0,\theta_{e0})} \tag{5.21}$$

and

$$B = \begin{bmatrix} \frac{\partial f_1}{\partial u_1} & \frac{\partial f_1}{\partial u_2} & \cdots & \frac{\partial f_1}{\partial u_n} \\ \frac{\partial f_2}{\partial u_1} & \frac{\partial f_2}{\partial u_2} & \cdots & \frac{\partial f_2}{\partial u_n} \\ \vdots & \vdots & \ddots & \vdots \\ \frac{\partial f_n}{\partial u_1} & \frac{\partial f_n}{\partial u_2} & \cdots & \frac{\partial f_n}{\partial u_n} \end{bmatrix}_{(x_0,u_0,\theta_{e0})} \tag{5.22}$$

We can see from the above matrices that the entries of A can be found directly by taking the partial derivative of the nonlinear function f with respect to the states. Now we find each entry by using the central differencing scheme.

For a scalar function $f(x)$, the derivative at x_0 can be approximated by

$$f'(x_0) \approx \frac{f(x_0+h) - f(x_0-h)}{2h} \tag{5.23}$$

where h is a small perturbation.

The same idea extends to vector functions as well. The first column of A is obtained by perturbing only i_d while keeping the other variables fixed

$$A_{(:,1)} \approx \frac{f(i_{d0}+h,\ i_{q0},\ v_{d0},\ v_{q0},\ \theta_{e0}) - f(i_{d0}-h,\ i_{q0},\ v_{d0},\ v_{q0},\ \theta_{e0})}{2h} \tag{5.24}$$

Similarly, the second column of A is obtained by perturbing only i_q

$$A_{(:,2)} \approx \frac{f(i_{d0},\ i_{q0}+h,\ v_{d0},\ v_{q0},\ \theta_{e0}) - f(i_{d0},\ i_{q0}-h,\ v_{d0},\ v_{q0},\ \theta_{e0})}{2h} \tag{5.25}$$

These can be substituted into our A matrix and we get,

$$A \approx \begin{bmatrix} \dfrac{\dot{i}_d(i_d+h,i_q) - \dot{i}_d(i_d-h,i_q)}{2h} & \dfrac{\dot{i}_d(i_d,i_q+h) - \dot{i}_d(i_d,i_q-h)}{2h} \\ \dfrac{\dot{i}_q(i_d+h,i_q) - \dot{i}_q(i_d-h,i_q)}{2h} & \dfrac{\dot{i}_q(i_d,i_q+h) - \dot{i}_q(i_d,i_q-h)}{2h} \end{bmatrix}_{(x_0,u_0,\theta_{e0})} \tag{5.26}$$

or

$$A = \begin{bmatrix} \dfrac{\partial f_1}{\partial i_d} & \dfrac{\partial f_1}{\partial i_q} \\ \dfrac{\partial f_2}{\partial i_d} & \dfrac{\partial f_2}{\partial i_q} \end{bmatrix}_{(x_0,u_0,\theta_{e0})} \tag{5.27}$$

where $f_1 = \dot{i}_d$ and $f_2 = \dot{i}_q$

Now to get B, we first simplify Eq(5.14)

$$\begin{bmatrix} \dot{i}_d \\ \dot{i}_q \end{bmatrix} = M^{-1} \left(\begin{bmatrix} v_d \\ v_q \end{bmatrix} + \begin{bmatrix} -R_s i_d + \omega_e \psi_q - \omega_e \dfrac{\partial \psi_d}{\partial \theta_e} \\ -R_s i_q - \omega_e \psi_d - \omega_e \dfrac{\partial \psi_q}{\partial \theta_e} \end{bmatrix} \right) \tag{5.28}$$

We can see from Eq(5.28) that

$$u = \begin{bmatrix} v_d \\ v_q \end{bmatrix}$$

appears directly inside the brackets multiplied by M^{-1}

Therefore, when the derivative of the state equation is taken with respect to the input vector u we directly get

$$B = M^{-1} \tag{5.29}$$

So at operating point we get

$$B = \left(\begin{bmatrix} \dfrac{\partial \psi_d}{\partial i_d} & \dfrac{\partial \psi_d}{\partial i_q} \\ \dfrac{\partial \psi_q}{\partial i_d} & \dfrac{\partial \psi_q}{\partial i_q} \end{bmatrix} \right)^{-1}_{(x_0,u_0,\theta_{e0})} \tag{5.30}$$

Now, the PMSM model depends on electrical angle θ_e. This means the local linear model changes with angle. So the linearisation was not carried out at one angle only, instead it was repeated over all angles

$$\theta_{e1},\ \theta_{e2},\ \ldots,\ \theta_{eN}$$

At each angle, a local linear model was obtained

$$\delta\dot{x} = A(\theta_{ek})\,\delta x + B(\theta_{ek})\,\delta u$$

So, many local linear models were obtained along the electrical cycle over the electrical angles.

Since controller design is easier with one constant linear model than many, the angle-dependent matrices were averaged

$$A_{\text{avg}} = \frac{1}{N}\sum_{k=1}^{N} A(\theta_{ek}) \tag{5.31}$$

$$B_{\text{avg}} = \frac{1}{N}\sum_{k=1}^{N} B(\theta_{ek}) \tag{5.32}$$

This gives us one final linear approximation

$$\delta\dot{x} = A_{\text{avg}}\,\delta x + B_{\text{avg}}\,\delta u \tag{5.33}$$

This average model represents the motor behavior near the chosen operating point over all angles. And it was found that a particular linearised model for any one specific operating point worked well for a range of other operating points around the chosen operating point.

5.1.1.3 Role of Feedforward Voltages

The feedforward voltages are used to compensate for the known voltage requirements of the motor at the operating point. These voltage requirements are

- the stator resistance drops $R_s i_d$ and $R_s i_q$
- the cross coupling terms $-\omega_e\psi_q$ and $+\omega_e\psi_d$
- the angle-dependent flux variation terms like $\omega_e\frac{\partial\psi_d}{\partial\theta_e}$

If these terms are not provided directly then the feedback controller would have to generate them by itself. Using LQI and PI controllers without any feedforward terms would make the currents oscillate about the chosen operating point because the LQI and PI controllers cannot generate all the required voltages. So the currents will no longer be stable and will not be able to track the reference currents.

By using feedforward voltages the predictable part of the required voltage is supplied directly while the feedback controller only needs to generate the additional correction required to remove small errors. So the total applied voltage is written as

$$v_d = v_{d,\text{ff}} + u_d \tag{5.34}$$
$$v_q = v_{q,\text{ff}} + u_q \tag{5.35}$$

where u_d and u_q are the outputs of the feedback controller.

To derive the feedforward voltages the motor is assumed to be at the chosen operating point so that the current derivatives are zero

$$\dot{i}_d = 0 \qquad \dot{i}_q = 0$$

Substituting it into (5.9) and (5.11) which are the general (partial derivative terms included) dq axis voltage equations gives the feedforward voltages

$$v_{d,\text{ff}} = R_s i_d + \omega_e \frac{\partial \psi_d}{\partial \theta_e} - \omega_e \psi_q \tag{5.36}$$
$$v_{q,\text{ff}} = R_s i_q + \omega_e \frac{\partial \psi_q}{\partial \theta_e} + \omega_e \psi_d \tag{5.37}$$

5.2 Design of Components of the Field Oriented Controller

5.2.1 Sampling and Delays

The LQI controller and the Kalman Filter was implemented in discrete time with a sampling frequency of 10 kHz. Since the controller and estimator are digital, the control signal is updated only at discrete sampling instants and is held constant between the sampling instants. So a zero-order hold (ZOH) model was used at the controller input and the estimator input.

In addition a delay of T_s was included in the controller output path as well as the feedforward output path. This was done to represent the effective delay introduced by PWM Update and computation effects in a digital drive system.

5.2.2 LQI Controller

The current controller was implemented as a discrete-time linear quadratic integral (LQI) regulator based on the averaged linearized PMSM current model. The controller is designed to regulate the d and q axis currents around the chosen operating point while reducing steady-state tracking error or bias.

Starting from the averaged continuous-time model

$$\dot{x}(t) = A_{\text{avg}} x(t) + B_{\text{avg}} u(t) \tag{5.38}$$

with

$$x = \begin{bmatrix} \delta i_d \\ \delta i_q \end{bmatrix}, \qquad u = \begin{bmatrix} \delta v_d \\ \delta v_q \end{bmatrix}$$

the model was converted to discrete time using zero-order hold (ZOH) with controller sampling period T_s. This gives us the discrete plant

$$x[k+1] = A_d x[k] + B_d u[k] \tag{5.39}$$

In order to reduce steady-state tracking error in both d and q currents the system was augmented with integral states corresponding to the current tracking errors. The current error vector is given as

$$e[k] = \begin{bmatrix} i_d[k] - i_{d,\text{ref}}[k] \\ i_q[k] - i_{q,\text{ref}}[k] \end{bmatrix} \tag{5.40}$$

and the integral states are given as

$$\xi[k+1] = \xi[k] + T_s e[k] \tag{5.41}$$

So the augmented state vector becomes

$$x_{\text{aug}}[k] = \begin{bmatrix} x[k] \\ \xi[k] \end{bmatrix} \tag{5.42}$$

Now if our outputs are the states themselves (not the integral state) then the output matrix is simply given by

$$C = I,$$

Then augmented discrete-time system using Eq(5.39) and Eq(5.41) is

$$x_{\text{aug}}[k+1] = \begin{bmatrix} A_d & 0 \\ T_s C & I \end{bmatrix} x_{\text{aug}}[k] + \begin{bmatrix} B_d \\ 0 \end{bmatrix} u[k] \tag{5.43}$$

where

$$A_{aug} = \begin{bmatrix} A_d & 0 \\ T_s C & I \end{bmatrix}, \quad B_{aug} = \begin{bmatrix} B_d \\ 0 \end{bmatrix}$$

The discrete LQI gain was obtained by solving the infinite-horizon discrete-time quadratic optimal control problem for the augmented system. For the cost function [30]

$$J = \sum_{k=0}^{\infty} \left(x_{\text{aug}}[k]^T Q x_{\text{aug}}[k] + u[k]^T R u[k] \right) \tag{5.44}$$

the optimal state-feedback gain [30] is given by

$$K_{\text{aug}} = \left(R + B_{\text{aug}}^T P B_{\text{aug}} \right)^{-1} B_{\text{aug}}^T P A_{\text{aug}} \tag{5.45}$$

where P is the positive semi-definite solution of the discrete algebraic Riccati equation

$$P = A_{\text{aug}}^T P A_{\text{aug}} - A_{\text{aug}}^T P B_{\text{aug}} \left(R + B_{\text{aug}}^T P B_{\text{aug}} \right)^{-1} B_{\text{aug}}^T P A_{\text{aug}} + Q \tag{5.46}$$

and Q and R are the matrices which represent weights/penalties on states and inputs respectively [30]. If Q is increased relative to R the controller gives more importance to reduce state deviations than to limit control effort. So the controller reacts more aggressively and generates larger input commands in order to drive the states to their desired values more quickly. Alternatively if R is increased relative to Q the controller gives more importance to limit the control effort. So in that case the controller becomes less aggressive resulting in smaller input commands and slower convergence of the states.

The resulting gain matrix is given by

$$K_{\text{aug}} = \begin{bmatrix} K_x & K_i \end{bmatrix} \tag{5.47}$$

where K_x acts on the current error and K_i acts on the integral states.

So the discrete LQI control law becomes

$$\Delta u[k] = -K_x e[k] - K_i \xi[k] \tag{5.48}$$

The LQI controller was however not used alone. It was combined with the feedforward voltages obtained from the ROM based PMSM model. The total commanded voltage is then given by

$$\begin{bmatrix} v_d[k] \\ v_q[k] \end{bmatrix} = \begin{bmatrix} v_{d,\text{ff}}[k] \\ v_{q,\text{ff}}[k] \end{bmatrix} + \Delta u[k] \tag{5.49}$$

Voltage saturation and anti-windup Since the inverter can only supply a limited voltage magnitude, saturation was introduced on the commanded dq voltage magnitude. The voltage magnitude was constrained such that its magnitude does not exceed the maximum allowable voltage.

In addition anti-windup was also included. This is necessary because, during saturation the controller may demand more voltage than can actually be applied. Without anti-windup the integral states would continue to grow even though the actuator is saturated which may lead to poor transient response or overshoot once the saturation is removed. So an anti-windup term was included in the integrator update. This term is based on the difference between the saturated and unsaturated voltage commands and it acts to reduce the growth of the integral states during saturation.

5.2.3 Cycle to Cycle Torque Ripple Optimizer

In this thesis, a cycle to cycle torque ripple optimizer was implemented for reduction of torque ripple in Electric Machines according to user's demands. The optimizer injects specific current harmonics into the d and q current references to cancel out the machine's natural harmonics (mainly the ripple created due to flux harmonics in the air gap) that give rise to the torque ripple. The main current harmonics that the optimizer generates are 12^{th} harmonics in d-axis, 12^{th} harmonics in q-axis, 6^{th} harmonics in d-axis and 6^{th} harmonics in q-axis. It was found that for both PMaSynRM and Spoke Type PMSMs, the 12^{th} order harmonics dominated the torque ripple and 6^{th} harmonics only played a minor role. Higher order harmonics like 18^{th} or 24^{th} had smaller amplitude and it was decided not to deal with them as firstly they had low contribution to torque ripple and secondly inverter switching frequencies will not allow current harmonics (which are injected) to be generated at such high frequencies especially at high rotor speeds (this problem exacerbates with higher number of pole pairs).

5.2.3.1 One Cycle Delay Structure

In this thesis, since sampling delays were considered, it was important to consider the fact that measurement, computation and generation of harmonics does not happen instantly unlike in cases of previous theses where sampling delays and discrete systems were not considered. In an ideal case the following takes place: when k_{th} cycle ends and $(k+1)_{th}$ cycle just begins, the ripple parameters from the k_{th} cycle are computed, then it is determined if the ripple has decreased or not and then the optimizer decides and generates (through inverter) new harmonics all in one instant with zero delay. Unfortunately, the digital controllers or processors have delays and cannot complete these tasks instantly. This is why it was decided to add one complete cycle delay in order to account for measurement, computation and generation delays as shown in Fig 5.1.

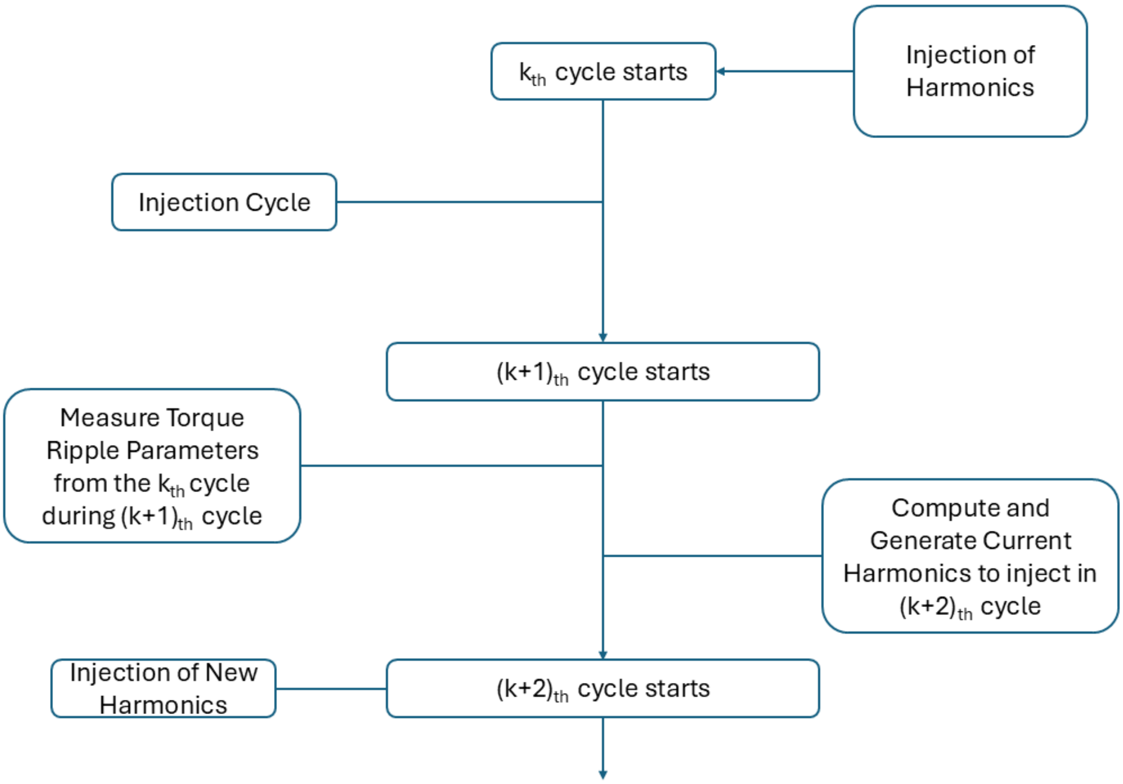

Figure 5.1: One Cycle Delay Structure in the Cycle to Cycle Torque Ripple Optimizer

The one cycle delay structure as shown in Fig 5.1 is as follows:

1.Measure cycle: the currently active coefficients of the harmonics are applied to the machine.

2.Compute/Hold cycle: during the following cycle, the previous coefficient set is held constant while the ripple metrics from the earlier cycle are processed and a new candidate coefficient vector of the harmonics is selected.

3.Injection: the newly selected coefficients are injected only at the next cycle boundary.

Now it could be asked why the optimizer is waiting for a whole cycle before injecting harmonics, or why it is not possible to inject harmonics immediately after the small delay instead of waiting for one cycle. The answer is that if the harmonics are injected midway during the cycle, then the measured torque ripple parameters could be slightly wrong. It is recommended that injected harmonics act over a full cycle rather than arbitrarily acting midway during the cycle. Otherwise, this could lead to a slightly wrong phase of the injected harmonics which can reinforce the torque ripple instead of reducing it.

5.2.3.2 Optimization Search Strategy

The cycle-to-cycle optimizer minimizes the following cost function:

$$J(k) = T_{\mathrm{rms}}(k) + \omega(T_{\mathrm{mean}}(k) - T_{\mathrm{mean,baseline}}) \tag{5.50}$$

where ω is the penalty weight, T_{mean} is the average torque after injection of harmonics, $T_{\mathrm{mean,baseline}}$ is the average torque for the case when no harmonics are injected, T_{rms} is the RMS value of Torque Ripple.

The injected d and q current references including their harmonics can be written as:

$$i_q(k) = i_{q0} + a_{q12}\cos\Big(12\theta_e(k)\Big) + b_{q12}\sin\Big(12\theta_e(k)\Big) + a_{q6}\cos\Big(6\theta_e(k)\Big) + b_{q6}\sin\Big(6\theta_e(k)\Big) \tag{5.51}$$

$$i_d(k) = i_{d0} + a_{d12}\cos\Big(12\theta_e(k)\Big) + b_{d12}\sin\Big(12\theta_e(k)\Big) + +a_{d6}\cos\Big(6\theta_e(k)\Big) + b_{d6}\sin\Big(6\theta_e(k)\Big) \tag{5.52}$$

The optimization method is a constrained coordinate wise search where it performs coordinate wise directional search on the harmonic coefficient vector given by:

$$c = \Big[a_{q12} \quad b_{q12} \quad a_{d12} \quad b_{d12} \quad a_{q6} \quad b_{q6} \quad a_{d6} \quad b_{d6}\Big]^T \tag{5.53}$$

and updates one coefficient at a time.

The 12^{th} and 6^{th} harmonic amplitude and phase for both d and q axes can be found from the above coefficients as follows (an example of q axis 6th harmonic only, the rest follow the same equations but with their own variables):

$$A_{q6} = \sqrt{a_{q6}^2 + b_{q6}^2}$$

$$\phi_{q6} = \mathrm{atan2}(-b_{q6},\ a_{q6})$$

The Optimization basically starts from zero coefficients (zero harmonics) and gradually builds up harmonics to reduce torque ripple as shown in Fig 5.2. This has the advantage that it does not require any pre-computed Harmonic LUTs to aid it. As a result, this optimizer can work with any kind of delays, temperature changes, different operating points, and even different PMSM machines if pole pair information is provided.

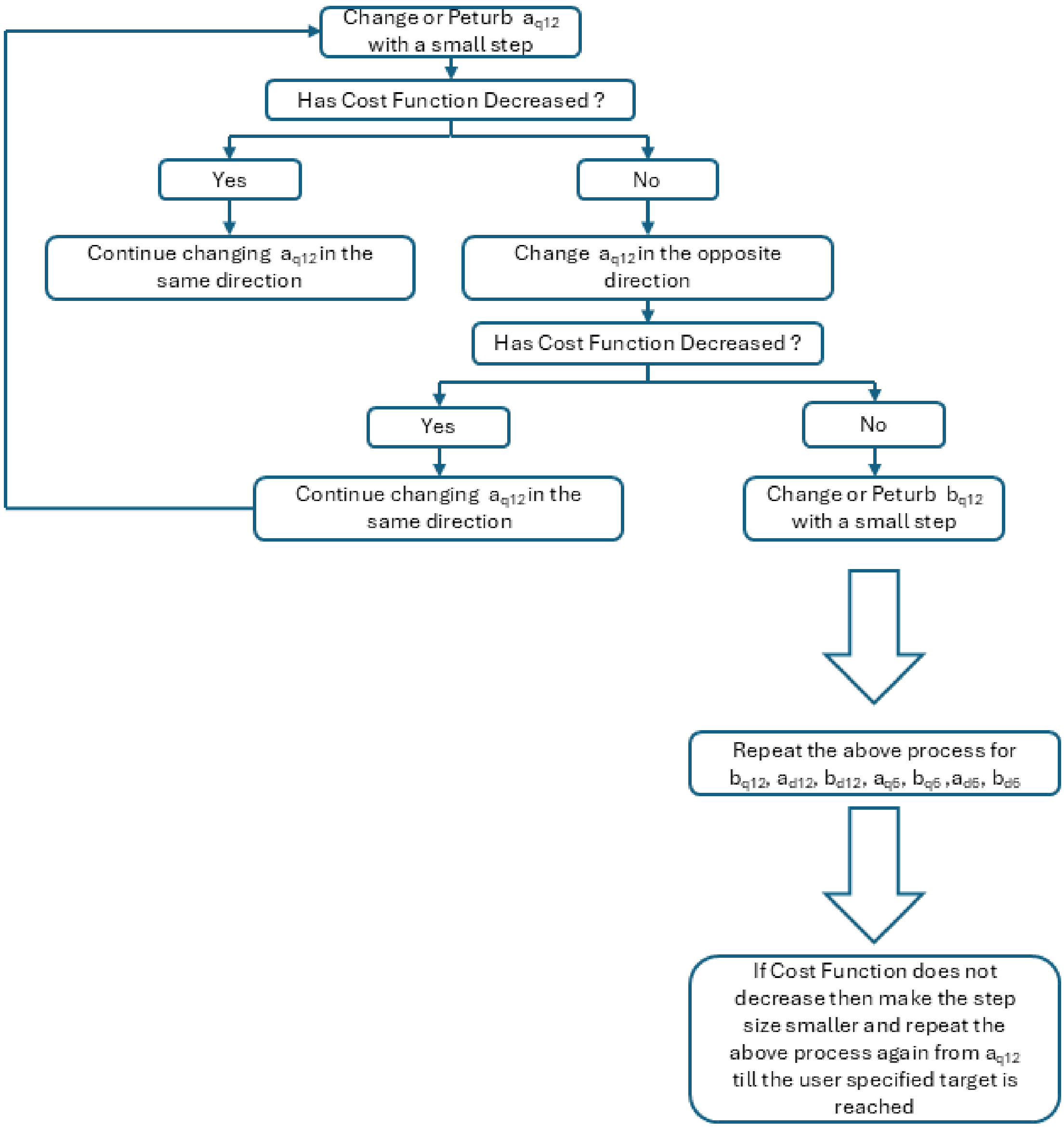

Figure 5.2: Optimization Algorithm Flow

The Optimization Process can be understood from the flowchart shown in Fig 5.2. At first, the optimizer peturbs a_{q12} in one direction. If cost function decreases, the optimizer keeps moving in the same direction. If the cost function increases, the optimizer moves in the opposite direction. If cost function increases in both directions, then optimizer works with b_{q12} and follows the same process as it did for a_{q12}. This process is then repeated for a_{d12}, b_{d12}, a_{q6}, b_{q6}, a_{d6}, b_{d6}. At the end of the full coordinate pass, if the target ripple reduction is still not reached then it decreases the step size to get optimum coefficients for minimum cost function until the target ripple reduction is reached.

The Optimizer also considers the inverter limits. The inverter is assumed to have a switching frequency of $f_{sw} = 25000$ Hz. By the rule of thumb, the maximum current harmonic frequency should not exceed $f_{sw}/10 = 2500$ Hz as it will have exactly

10 samples per harmonic cycle and if it has less than 10 samples, then it becomes difficult for the controller to reconstruct the harmonic wave and there could be a loss of control. Also, Nyquist limit could be reached if the number of samples is too small. During analysis of the electric machines it is found that the 12^{th} harmonics could be injected only upto 3125 RPM and 6^{th} harmonics could be injected only upto 6250 RPM for 4 pole pairs.

5.2.4 Flux Estimation using a time varying linear KF and Torque Dilemma in Steady State

The dq voltage equations for a general PMSM are given by:

$$\dot{\psi}_d = v_d - R_s i_d + \omega_e \psi_q \tag{5.54}$$

$$\dot{\psi}_q = v_q - R_s i_q - \omega_e \psi_d \tag{5.55}$$

where R_s is the DC resistance of the Stator Winding, ψ_d and ψ_q are the flux linkages in d and q coordinates, v_d,v_q and i_d,i_q are the voltages and currents in d and q coordinates.

It is considered that voltages, currents and rotor speed (and rotor position by integrating rotor speed) are measured using sensors, so they are known quantities. Since only ψ_d, ψ_q and R_s are unknown, the voltage-flux equations still remain linear in nature. Since there is no non-linearity, it was decided to use a discrete time linear time varying Kalman Filter instead of an Extended Kalman Filter.

The linear time-varying Kalman filter was initially designed to estimate the augmented state

$$x = \begin{bmatrix} \psi_d & \psi_q & R_s \end{bmatrix}^T \tag{5.56}$$

However at a steady operating point with constant i_d, i_q and constant nonzero ω_e, the augmented state is not uniquely identifiable from (5.54) and (5.55).

We show why the quantities ψ_d, ψ_q, and R_s cannot be uniquely separated at a fixed operating point as follows:

Consider two candidate solutions of the dq voltage-flux equations:

$$(\psi_d, \psi_q, R_s) \qquad \text{and} \qquad (\tilde{\psi}_d, \tilde{\psi}_q, \tilde{R}_s)$$

Now the errors between these 2 solutions are given by

$$\delta\psi_d = \tilde{\psi}_d - \psi_d \qquad \delta\psi_q = \tilde{\psi}_q - \psi_q \qquad \delta R_s = \tilde{R}_s - R_s \tag{5.57}$$

For each candidate solution, we get 2 dq voltage equations. So we subtract the dq voltage equations of one candidate with another to get:

$$\delta\dot{\psi}_d = -i_d\, \delta R_s + \omega_e\, \delta\psi_q \tag{5.58}$$

$$\delta\dot{\psi}_q = -i_q\, \delta R_s - \omega_e\, \delta\psi_d \tag{5.59}$$

We now consider the case when the errors defined above are constant. Since the errors are constant, their derivatives will be zero if the operating point (i_d. i_q, ω_e) is fixed:

$$\delta\dot{\psi}_d = 0 \qquad \delta\dot{\psi}_q = 0 \tag{5.60}$$

Substituting (5.60) in (5.58) and (5.59) gives,

$$0 = -i_d\,\delta R_s + \omega_e\,\delta\psi_q \quad \Rightarrow \quad \delta\psi_q = \frac{i_d}{\omega_e}\,\delta R_s \tag{5.61}$$

$$0 = -i_q\,\delta R_s - \omega_e\,\delta\psi_d \quad \Rightarrow \quad \delta\psi_d = -\frac{i_q}{\omega_e}\,\delta R_s \tag{5.62}$$

Therefore, for any resistance error δR_s there exists a corresponding constant flux error

$$\delta\psi_d = -\frac{i_q}{\omega_e}\,\delta R_s \qquad \delta\psi_q = \frac{i_d}{\omega_e}\,\delta R_s \tag{5.63}$$

that produces exactly the same electrical dynamics. This proves that at a fixed operating point, the effect of an error in R_s can be exactly compensated by constant errors in ψ_d and ψ_q. So the three quantities cannot be uniquely identified from the voltage-flux equations alone. Adding current harmonics does not necessarily solve the problem because the flux states can absorb part of the additional excitation instead of forcing R_s to its true value. So it was considered that R_s is known through a previous transient state of the motor.

As a general information to the reader or whoever wants to extend this thesis further: R_s is usually identified accurately at standstill using self commisioning methods. At standstill, just when the driver starts the EV, the inverter gives a strong DC pulse or injection to the stator windings whereby R_s is identified accurately and this value is used further to estimate R_s when the operating conditions change. During transient period, it becomes possible to identify R_s and this value is used during the steady state. However, if temperature changes during steady state, then this R_s is adjusted using a thermal model of resistance. If at all it is needed to estimate R_s without any initial condition in steady state, then 2 operating points are run at the same time (can be done in simulation) to remove the ambiguity of R_s. In transient conditions, it is necessary to add the mechanical dynamics equation to the Kalman Filter to be able to identify R_s [31].

5.2.4.1 Torque Ripple in Steady State

In the present work, the only available signals are v_d, v_q, i_d, i_q, ω_e and the stator resistance R_s is assumed known. The machine is analyzed at an imposed constant speed, and no direct torque sensor, torque map, flux map, or finite-element torque model is used inside the Kalman Filter.

Electromagnetic torque in this thesis is computed using

$$T_e = \frac{3}{2}p\left(\psi_d i_q - \psi_q i_d\right). \tag{5.64}$$

where p is the number of pole pairs

However, the total electromagnetic torque is more generally given by

$$T_{\mathrm{actual}} = T_e + T_{\mathrm{res}} \tag{5.65}$$

where, T_{res} consists of contribution cogging torque and other non-linearities

The measured signals together with R_s do not uniquely reveal the residual term T_{res} in (5.65). Hence, in the present case, the estimator can reconstruct only the torque ripple contained in the dq flux harmonics.

This limitation mainly arises because the rotor speed is imposed and kept constant (steady state). So the mechanical dynamics

$$J\dot{\omega} = T_e - T_L - B\omega \tag{5.66}$$

do not provide additional information for identifying full torque ripple. If the speed were free to vary then torque ripple can affect the mechanical response and this response can provide extra information.

So even when the estimated fluxes and their harmonics match well, the reconstructed torque ripple from (5.64) may still underestimate the true torque ripple and may not reproduce its phase exactly.

The Torque Ripple identified during transient period is also not fully accurate. This might seem trivial at first but even small errors in the phase of estimated torque ripple can reduce the effectiveness of the Torque Ripple Optimizer. This is why it was preferred in this thesis to use the Torque Ripple Information from an LUT for use in the Torque Ripple Optimizer.

5.2.4.2 Kalman Filter Design

A discrete-time Kalman filter is a recursive state estimator [30] for systems of the form

$$x_{k+1} = A_k x_k + B_k u_k + w_k \tag{5.67}$$

$$y_k = C_k x_k + D_k u_k + v_k \tag{5.68}$$

where x_k is the state vector, u_k is the known input, y_k is the measured output, w_k is the process noise, v_k is the measurement noise and w_k, v_k are uncorrelated

The filter consists of two steps.

5.2.4.2.1 Prediction step

$$\hat{x}_{k|k-1} = A_{k-1}\hat{x}_{k-1|k-1} + B_{k-1}u_{k-1} \tag{5.69}$$

$$P_{k|k-1} = A_{k-1}P_{k-1|k-1}A_{k-1}^T + Q_{k-1} \tag{5.70}$$

Here, the state for time step k is predicted at time step k-1. P is the error covariance matrix which is also predicted (tells us how error is propagated) for time step k at time step k -1. Note that in this prediction step, we are still in k-1 time step and not reached time step k.

5.2.4.2.2 Correction step The innovation is

$$\nu_k = y_k - \hat{y}_k, \tag{5.71}$$

where

$$\hat{y}_k = C_k \hat{x}_{k|k-1} + D_k u_k \tag{5.72}$$

The innovation indicates how much the true measurements y_k vary from $\hat{y}_k$ which are estimates [30].

The innovation covariance is

$$S_k = C_k P_{k|k-1} C_k^T + R_k \tag{5.73}$$

This shows how the error is propagated through the measurements

and the Kalman gain [30] is

$$K_k = P_{k|k-1} C_k^T S_k^{-1} \tag{5.74}$$

Then the corrected state estimate [30] is given by

$$\hat{x}_{k|k} = \hat{x}_{k|k-1} + K_k \nu_k \tag{5.75}$$

Now, once we get the state estimate at current time step k using the Kalman Gain, we need to update the covariance error matrix which is done using

$$P_{k|k} = (I - K_k C_k) P_{k|k-1} \tag{5.76}$$

5.2.4.2.3 Chosen States and Process Model In this thesis, it was decided to use the Kalman Filter to estimate the mean, 6^{th} order harmonics and 12^{th} order harmonics of the fluxes and then combine them to reconstruct the flux estimate rather than trying to estimate the fluxes directly as it did not give good results. It was possible to estimate even the 18^{th} or 24^{th} order harmonics but analysis of the fluxes showed that the mean, 6^{th} and 12^{th} order harmonics were the most dominant in the electric machines.

The state vector used in the Kalman Filter is given by

$$x_k = \begin{bmatrix} \psi_{d0} & \psi_{q0} & a_{d6} & b_{d6} & a_{q6} & b_{q6} & a_{d12} & b_{d12} & a_{q12} & b_{q12} \end{bmatrix}^T \tag{5.77}$$

The quantities ψ_{d0} and ψ_{q0} represent the mean flux components, while the remaining coefficients define the 6th- and 12th-order harmonic content which are used to reconstruct the flux estimates given by:

$$\hat{\psi}_d(k) = \psi_{d0} + a_{d6}\cos\Big(6\theta_e(k)\Big) + b_{d6}\sin\Big(6\theta_e(k)\Big) + a_{d12}\cos\Big(12\theta_e(k)\Big) + b_{d12}\sin\Big(12\theta_e(k)\Big) \tag{5.78}$$

$$\hat{\psi}_q(k) = \psi_{q0} + a_{q6}\cos\Big(6\theta_e(k)\Big) + b_{q6}\sin\Big(6\theta_e(k)\Big) + a_{q12}\cos\Big(12\theta_e(k)\Big) + b_{q12}\sin\Big(12\theta_e(k)\Big) \tag{5.79}$$

Note that R_s is known here

In this thesis, it was decided to go with a random walk state model as the process model. Unlike other states like stator currents or rotor speed, the chosen states do not have a simple deterministic state evolution model of the form

$$x_{k+1} = f(x_k, u_k) \tag{5.80}$$

There is no simple physical model available that tells us exactly how each harmonic coefficient should change from one time step to the next.

For this reason, a random-walk state model is used. In a random-walk model, the prediction of the next state is simply the current state plus a small random change:

$$x_{k+1} = x_k + w_k \tag{5.81}$$

where w_k is the process noise. This means that the states are assumed to vary only slowly from one sample to another, but deviations are allowed. Since deviations are allowed, this makes our estimator more robust if the operating point or the operating conditions change.

In standard state space form, this can be written as

$$x_{k+1} = Ax_k + w_k, \qquad A = I \tag{5.82}$$

where I is the identity matrix.

The mean and harmonic flux coefficients remain close to their previous values over one sample. However, they are not perfectly constant. Any small variation or modeling mismatch is absorbed into the process noise term w_k.

This choice of random walk model is good for our thesis because it avoids a complicated deterministic state evolution model. If an inaccurate dynamic state model was considered for the harmonic coefficients, then the Kalman filter would give incorrect estimates. The random walk model is therefore a good and robust choice. It does not know the exact state dynamics but it still allows the states to move gradually if the measurements tell that they should.

Another important advantage is that it is computationally cheap. Since the state transition matrix A is just the identity matrix, the prediction step becomes very simple as can be seen below:

$$\hat{x}_{k+1|k} = \hat{x}_{k|k} \tag{5.83}$$

$$P_{k+1|k} = P_{k|k} + Q_k \tag{5.84}$$

where Q_k is the process-noise covariance matrix.

Since the equations for prediction are so simple, it is computationally faster and cheap. The process-noise covariance matrix Q_d determines how freely each state is allowed to vary.

5.2.4.2.4 Measurement Model The measured outputs available to the Kalman Filter are the dq voltages

$$y_k = \begin{bmatrix} v_d(k) \\ v_q(k) \end{bmatrix} \tag{5.85}$$

The corresponding predicted output is

$$\hat{y}_k = \begin{bmatrix} \hat{v}_d(k) \\ \hat{v}_q(k) \end{bmatrix} \tag{5.86}$$

where $\hat{v}_d$ and $\hat{v}_q$ are voltages obtained by using the state estimates

Since the stator resistance R_s is considered as known, and the currents i_d and i_q are measured, the resistive voltage drops $R_s i_d$, $R_s i_q$ are also known at each sample. So we can move these known terms to the left hand side of the dq voltage equations. This does not change the physics but it only simplifies the measurement equation by removing known quantities. So instead of working directly with y_k, a modified measurement vector is introduced

$$\tilde{y}_k = \begin{bmatrix} v_d(k) - R_s i_d(k) \\ v_q(k) - R_s i_q(k) \end{bmatrix} \tag{5.87}$$

From the PMSM dq voltage equations,

$$v_d = R_s i_d + \dot{\psi}_d - \omega_e \psi_q \tag{5.88}$$

$$v_q = R_s i_q + \dot{\psi}_q + \omega_e \psi_d \tag{5.89}$$

the modified equations becomes

$$v_d - R_s i_d = \dot{\psi}_d - \omega_e \psi_q \tag{5.90}$$

$$v_q - R_s i_q = \dot{\psi}_q + \omega_e \psi_d \tag{5.91}$$

To make things simple and easy to read we define

$$c_6 = \cos\Big(6\theta_e(k)\Big) \quad s_6 = \sin\Big(6\theta_e(k)\Big) \quad c_{12} = \cos\Big(12\theta_e(k)\Big) \quad s_{12} = \sin\Big(12\theta_e(k)\Big) \tag{5.92}$$

Then the reconstructed flux estimate equations can be written as

$$\hat{\psi}_d(k) = \psi_{d0} + a_{d6}c_6 + b_{d6}s_6 + a_{d12}c_{12} + b_{d12}s_{12} \tag{5.93}$$

$$\hat{\psi}_q(k) = \psi_{q0} + a_{q6}c_6 + b_{q6}s_6 + a_{q12}c_{12} + b_{q12}s_{12} \tag{5.94}$$

Taking the derivatives of the above equations gives

$$\dot{\hat{\psi}}_d(k) = -6\omega_e a_{d6}s_6 + 6\omega_e b_{d6}c_6 - 12\omega_e a_{d12}s_{12} + 12\omega_e b_{d12}c_{12} \tag{5.95}$$

$$\dot{\hat{\psi}}_q(k) = -6\omega_e a_{q6}s_6 + 6\omega_e b_{q6}c_6 - 12\omega_e a_{q12}s_{12} + 12\omega_e b_{q12}c_{12} \tag{5.96}$$

Substituting these expressions (5.95) and (5.96) into the modified voltage equations (5.90) and (5.91) gives us the measurement equations

$$\begin{aligned} v_d - R_s i_d = 0 \cdot \psi_{d0} - \omega_e\psi_{q0} - 6\omega_e s_6\, a_{d6} + 6\omega_e c_6\, b_{d6} - \omega_e c_6\, a_{q6} - \omega_e s_6\, b_{q6} \\ - 12\omega_e s_{12}\, a_{d12} + 12\omega_e c_{12}\, b_{d12} - \omega_e c_{12}\, a_{q12} - \omega_e s_{12}\, b_{q12} \end{aligned} \tag{5.97}$$

and

$$\begin{aligned} v_q - R_s i_q = \omega_e\psi_{d0} + 0 \cdot \psi_{q0} + \omega_e c_6\, a_{d6} + \omega_e s_6\, b_{d6} - 6\omega_e s_6\, a_{q6} + 6\omega_e c_6\, b_{q6} \\ + \omega_e c_{12}\, a_{d12} + \omega_e s_{12}\, b_{d12} - 12\omega_e s_{12}\, a_{q12} + 12\omega_e c_{12}\, b_{q12} \end{aligned} \tag{5.98}$$

Now we know that the state vector is

$$x_k = \begin{bmatrix} \psi_{d0} & \psi_{q0} & a_{d6} & b_{d6} & a_{q6} & b_{q6} & a_{d12} & b_{d12} & a_{q12} & b_{q12} \end{bmatrix}^T \tag{5.99}$$

Then combining Eq(5.97), Eq(5.98) and Eq(5.99) gives us the following Kalman Filter Measurement Equation

$$\tilde{y}_k = C_k x_k + v_k \tag{5.100}$$

where

$$C_k = \begin{bmatrix} 0 & -\omega_e & -6\omega_e s_6 & 6\omega_e c_6 & -\omega_e c_6 & -\omega_e s_6 & -12\omega_e s_{12} & 12\omega_e c_{12} & -\omega_e c_{12} & -\omega_e s_{12} \\ \omega_e & 0 & \omega_e c_6 & \omega_e s_6 & -6\omega_e s_6 & 6\omega_e c_6 & \omega_e c_{12} & \omega_e s_{12} & -12\omega_e s_{12} & 12\omega_e c_{12} \end{bmatrix} \tag{5.101}$$

So, the predicted measurement that we use in innovation is

$$\hat{\tilde{y}}_k = C_k \hat{x}_k \tag{5.102}$$

The innovation used in the Kalman filter is therefore

$$\nu_k = \tilde{y}_k - \hat{\tilde{y}}_k \tag{5.103}$$

5.2.4.3 Leaky dq Voltage Flux Observer Design

In addition to the Kalman filter, a simpler flux estimator was also implemented in the form of a leaky *dq* voltage-model flux observer. The purpose of this observer is to estimate the instantaneous dq flux linkages directly from the measured voltages and currents when the stator resistance is known.

5.2.4.3.1 Equations used: We use the dq voltage equation of PMSM:

$$\dot{\psi}_d = v_d - R_s i_d + \omega_e \psi_q \tag{5.104}$$

$$\dot{\psi}_q = v_q - R_s i_q - \omega_e \psi_d \tag{5.105}$$

These equations show that if v_d, v_q, i_d, i_q, ω_e, and R_s are known, then the fluxes can be found out by integrating the flux derivatives.

5.2.4.3.2 Pure voltage model observer A direct observer can be written as

$$\dot{\hat{\psi}}_d = v_d - R_s i_d + \omega_e \hat{\psi}_q \tag{5.106}$$

$$\dot{\hat{\psi}}_q = v_q - R_s i_q - \omega_e \hat{\psi}_d \tag{5.107}$$

This is called a voltage-model observer because it is obtained directly from the voltage equations. However the pure voltage-model observer is sensitive to small errors. Since the observer integrates the flux derivatives over time even a small persistent error can accumulate and cause drift in the estimated fluxes.

5.2.4.3.3 Leaky Observer To reduce this drift, a leakage term is added. In the implemented observer, the estimated fluxes are pulled toward trusted initial flux values. The observer equations used in this thesis are

$$\dot{\hat{\psi}}_d = v_d - R_s i_d + \omega_e \hat{\psi}_q - \lambda\Big(\hat{\psi}_d - \psi_{d,\text{init}}\Big) \tag{5.108}$$

$$\dot{\hat{\psi}}_q = v_q - R_s i_q - \omega_e \hat{\psi}_d - \lambda\Big(\hat{\psi}_q - \psi_{q,\text{init}}\Big) \tag{5.109}$$

where $\psi_{d,\text{init}}$ and $\psi_{q,\text{init}}$ are the initial flux values and λ is the leakage term.

The purpose of the leakage term is only to suppress drift. If the estimated flux drifts too far away the leakage term pulls it back. Because of this reason the observer is called a leaky voltage model observer.

5.2.4.3.4 Forward Euler discretization Although the observer equations are written in continuous time, the implementation is in discrete time. To dicretise the observer equations, forward euler discretisation is used.

For a simple differential equation

$$\dot{x}(t) = f(x(t), u(t)) \tag{5.110}$$

Forward Euler Discretistaion gives the discrete time form

$$x[k+1] = x[k] + T_s f(x[k], u[k]) \tag{5.111}$$

where T_s is the sampling time.

Applying this to the leaky flux observer gives

$$\hat{\psi}_d[k+1] = \hat{\psi}_d[k] + T_s\Big(v_d[k] - R_s i_d[k] + \omega_e[k]\hat{\psi}_q[k] - \lambda(\hat{\psi}_d[k] - \psi_{d,\text{init}})\Big) \quad (5.112)$$

$$\hat{\psi}_q[k+1] = \hat{\psi}_q[k] + T_s\Big(v_q[k] - R_s i_q[k] - \omega_e[k]\hat{\psi}_d[k] - \lambda(\hat{\psi}_q[k] - \psi_{q,\text{init}})\Big) \quad (5.113)$$

The main disadvantage of this leaky observer is that the leakage term introduces a bias toward the initial flux values. So the observer will work well only when the operating point is fixed and when the initial flux values are chosen accurately. The leakage term is necessary because without it, the flux waveforms do not match. The leakage term depends on the operating point and changes with it which is another disadvantage.

5.2.5 Overall control framework

The overall control framework has LQI Current Controller, Torque Ripple Optimizer, linear time-varying Kalman Filter, Feedforward Compensation and the Map-Based ROM Plant in a single unit structure as shown in Fig 5.3.

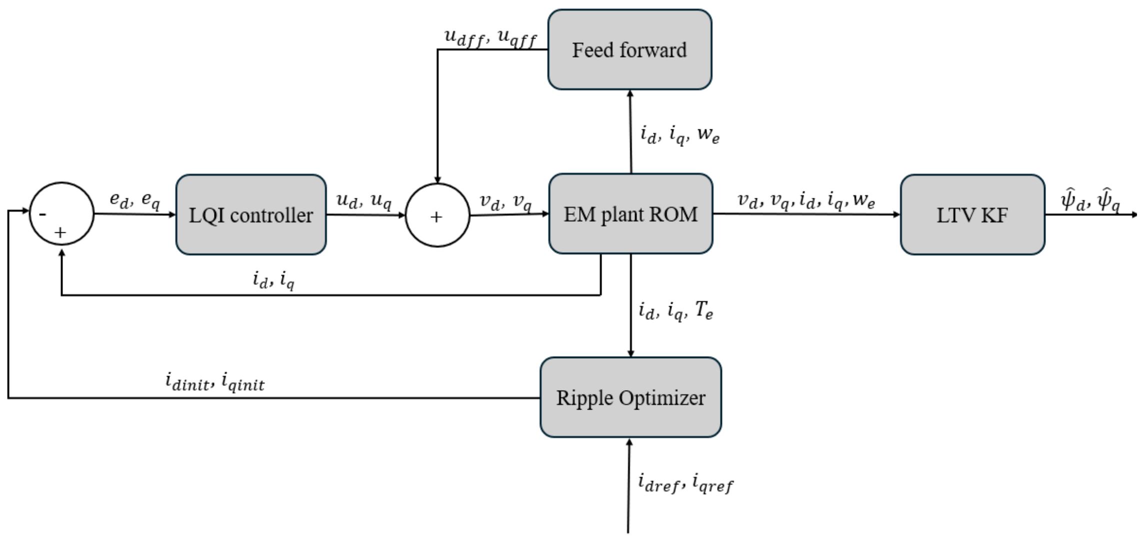

Figure 5.3: Overall control framework with LQI current control, feedforward compensation, ripple control, and linear KF-based estimation

Reference currents i_d^{ref} and i_q^{ref} with ripple compensation terms generates the current commands which is processed by LQI controller to generate the feedback voltage command. In parallel, feedforward block gives model-based voltage compensation to improve current tracking and eliminate the coupling effect. Feedback and feedforward voltages are summed and applied (after undergoing a sampling delay) to the electromagnetic plant ROM, which is a non linear model. Based on the output torque, torque ripple optimizer generates current harmonics to suppress the dominant torque ripple harmonics. To maintain the accuracy for flux estimation, a discrete time linear time varying Kalman Filter is implemented. In this way, the overall framework supports accurate current regulation, reduction of torque ripple, and robustness over the operating range.

5.3 Results of the Control System and Torque Optimizer

This section presents the performance of the current controller and torque ripple optimizer at two selected operating conditions. The results are evaluated at two motor speeds, namely 1000 rpm and 6000 rpm, and at two corresponding current operating points: $(i_d, i_q) = (-100\ \text{A}, 200\ \text{A})$ and $(i_d, i_q) = (-350\ \text{A}, 100\ \text{A})$. The 1000 rpm case is evaluated only at $(-100\ \text{A}, 200\ \text{A})$, while the 6000 rpm case is evaluated only at $(-350\ \text{A}, 100\ \text{A})$.

The current controller and harmonic-based torque ripple optimizer are applied to the hybrid-magnet PMaSynRM and the ferrite Spoke PMSM only. The operating point $(-100\ \text{A}, 200\ \text{A})$ was selected for the low-speed case because it represents an intermediate loaded condition suitable for torque ripple analysis. At 6000 rpm, however, this current point is no longer feasible because the voltage ellipse becomes significantly smaller at high speed, causing the point to fall outside the voltage limit. Therefore, the field-weakening operating point $(-350\ \text{A}, 100\ \text{A})$ was selected for the high-speed evaluation.

In order to represent the behaviour of a practical digital current controller, the simulations include a one-sample computational delay and zero-order hold (ZOH) effects. These effects are included when evaluating the tracking performance of the current controller as well as the torque ripple reduction achieved by the harmonic optimizer.

5.3.1 Current Control and Torque Ripple Optimization at 1000 rpm

This section presents the current controller and torque ripple optimizer results for the electric machines at 1000 rpm. The selected operating point is $(i_d, i_q) = (-100\ \text{A}, 200\ \text{A})$. First, the controller and observer performance are evaluated without harmonic injection. Then, the effect of the harmonic current injection on current tracking and torque ripple reduction is presented.

5.3.1.1 PMaSynRM Behaviour

Figure 5.4 shows the d and q-axis currents before harmonic injection.

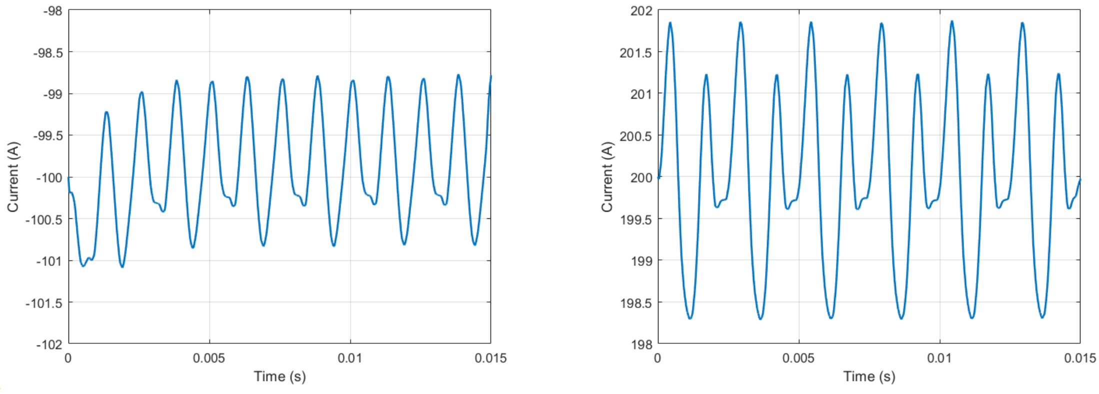

(a) d-axis current (b) q-axis current

Figure 5.4: Current response of the PMaSynRM at 1000 rpm before harmonic injection.

The controller is able to regulate the currents close to their reference values. Only small periodic oscillations are visible around the commanded operating point, which are mainly caused by the discrete-time control implementation which include delays and ZOH. This confirms that the current controller provides a suitable baseline operating condition before the torque ripple optimizer is activated.

The flux estimation performance before harmonic injection is shown in Fig. 5.5.

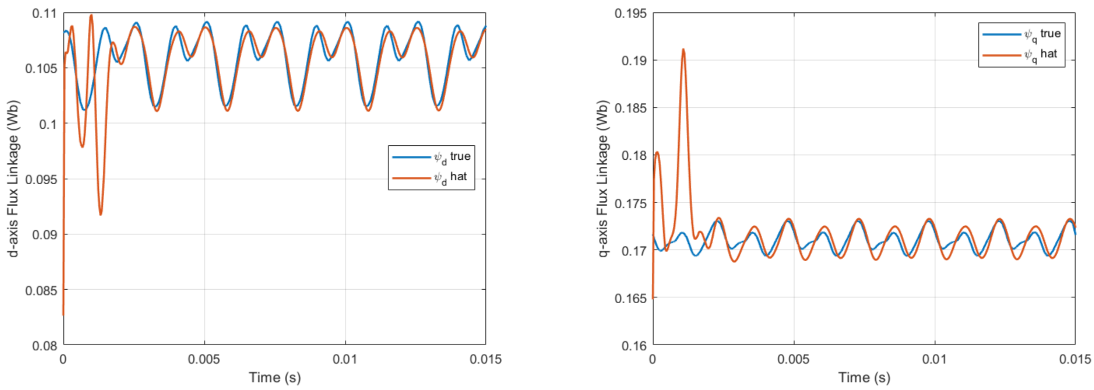

(a) d-axis flux linkage (b) q-axis flux linkage

Figure 5.5: Comparison between true and estimated flux linkages for the PMaSynRM at 1000 rpm before harmonic injection.

The true and estimated d-axis flux linkages show good agreement after the initial transient. A similar behaviour is observed for the q-axis flux linkage. This indicates that the Kalman Filter is able to reconstruct the flux behaviour at this operating point.

Figure 5.6 compares the true torque and the estimated torque before harmonic injection.

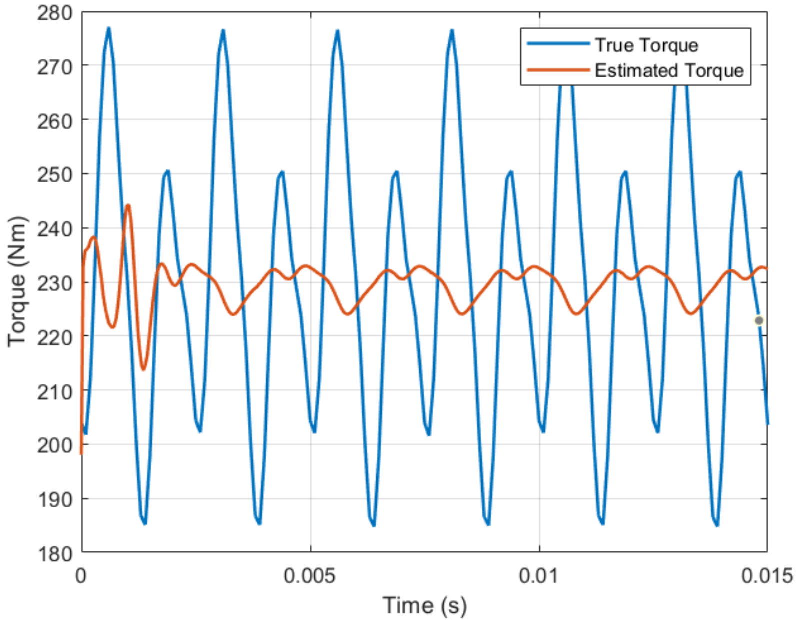

Figure 5.6: Comparison between true and estimated torque for the PMaSynRM at 1000 rpm before harmonic injection.

The true torque contains a significant periodic ripple component, while the estimated torque mainly follows the mean torque level and captures only a reduced part of the torque oscillation. This is expected because the estimated torque is reconstructed from the estimated flux linkages and currents, and does not fully include all torque ripple contributions such as slotting, cogging, and other spatial harmonic effects.

After the baseline case is evaluated, harmonic current injection is applied to reduce the torque ripple. The resulting d and q-axis currents are shown in Fig. 5.7.

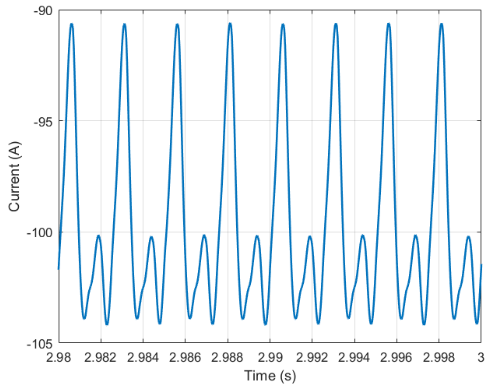

(a) d-axis current

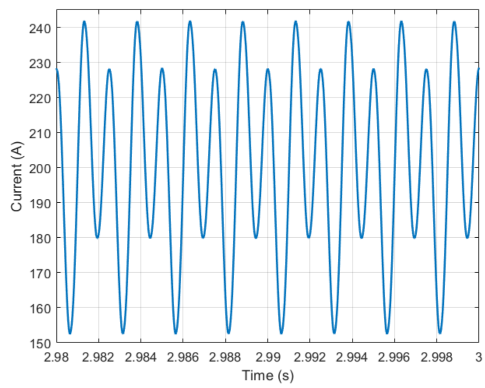

(b) q-axis current

Figure 5.7: Current response of the PMaSynRM at 1000 rpm after harmonic injection.

Compared with the no-injection case, clear harmonic components are now visible in both current components. These current harmonics are intentionally introduced by the optimizer in order to counteract the dominant torque ripple components. The q-axis current shows a larger harmonic variation than the d-axis current, indicating that the optimizer mainly uses the torque-producing current component for ripple compensation at this operating point.

The convergence of the torque ripple optimizer is shown in Fig. 5.8.

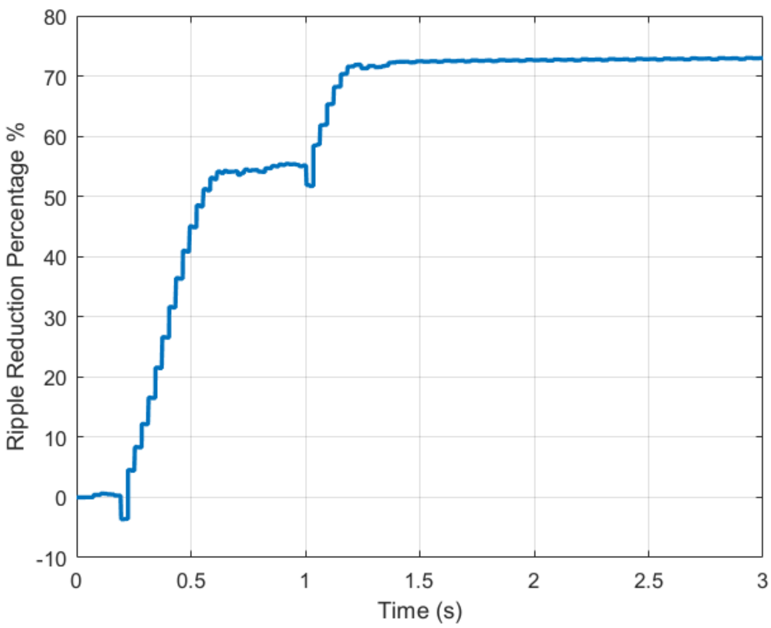

Figure 5.8: Torque ripple reduction percentage for the PMaSynRM at 1000 rpm.

The ripple reduction initially increases rapidly as the harmonic injection terms are updated. After the initial convergence period, the reduction settles to approximately 73%. This shows that the selected harmonic injection method is effective for this operating condition.

The final torque comparison before and after harmonic injection is shown in Fig. 5.9.

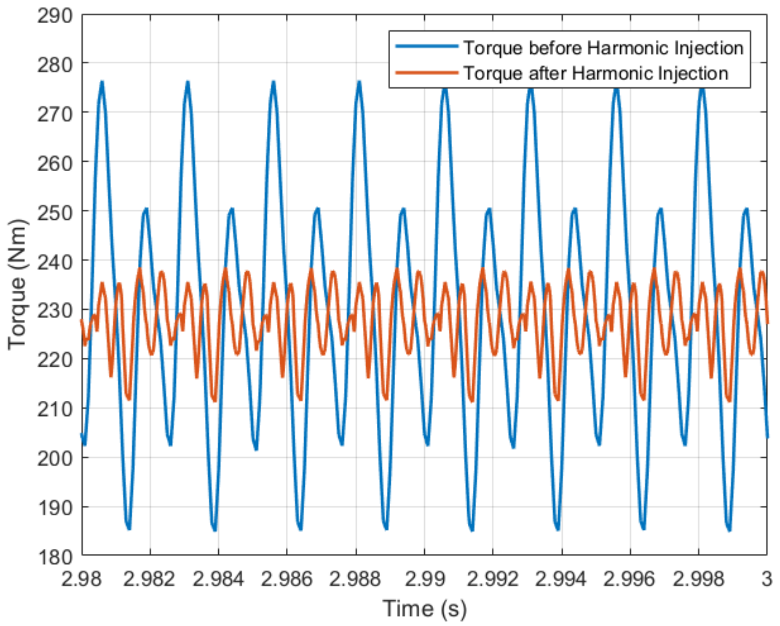

Figure 5.9: Torque response of the PMaSynRM at 1000 rpm before and after harmonic injection.

The original torque contains a large periodic ripple around the mean torque value. After harmonic injection, the torque ripple amplitude is significantly reduced, while the mean torque level remains approximately in the same range. Therefore, injected current harmonics are able to reduce a large part of the torque ripple without causing a major change in the average torque production.

Figure 5.10 shows the torque harmonic amplitude spectrum before and after harmonic injection for the PMaSynRM at 1000 rpm. Before harmonic injection, the torque ripple is mainly dominated by the 12th torque harmonic, followed by the 6th and 24th harmonics. The 18th and 30th harmonics are almost negligible, while the 36th harmonic has only a small contribution.

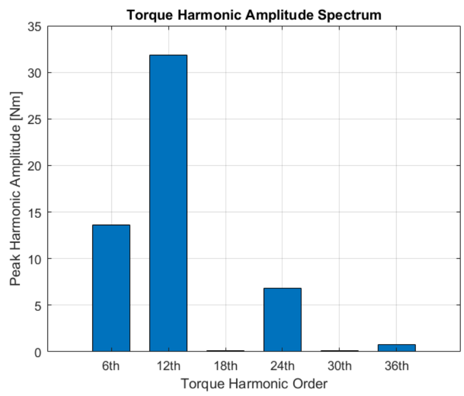

(a) Before harmonic injection

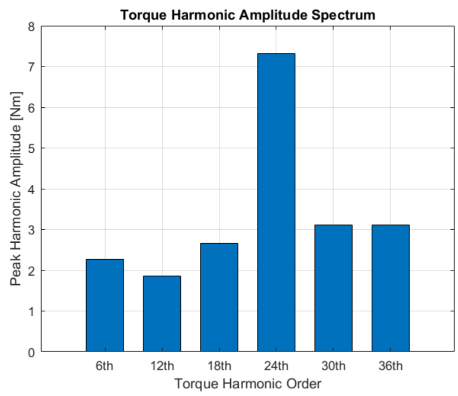

(b) After harmonic injection

Figure 5.10: Torque harmonic amplitude spectrum of the PMaSynRM at 1000 rpm before and after harmonic injection.

After harmonic injection, the amplitudes of the dominant 6th and 12th torque harmonics are significantly reduced. This confirms that the harmonic current injection is effective in suppressing the main torque ripple components. However, the 24th harmonic becomes the largest remaining component after injection. This indicates that although the dominant low-order harmonics are strongly reduced, some higher-order harmonic content remains in the torque waveform. Therefore, the total torque ripple is reduced considerably, but it is not completely eliminated.

The flux linkages and estimated torque are not plotted after harmonic injection because the final post-injection performance is evaluated using the true machine response. The Kalman Filter is mainly used to estimate the mean fluxes and mean torque as it is not able estimate the mean fluxes after current harmonic injection. The mean values of the relevant quantities are included in Table 5.1.

Table 5.1: Comparison of mean quantities and losses for the PMaSynRM at 1000 rpm before and after harmonic injection.

Quantity(Mean)	**Before Injection**	**After Injection**	**Unit**
i_d	-99.8	-100.6	A
i_q	200.1	198.2	A
T_e (Actual)	227.7	229.5	Nm
T_e (KF)	229	228.2	Nm
Copper loss	874.78	1003.65	W
Core loss	264.92	350.24	W

From Table 5.1, it can be observed that the harmonic injection does not significantly shift the mean operating point of the machine.

The mean actual torque increases slightly from 227.7 Nm to 229.5 Nm. The Kalman Filter torque estimate also remains close to the actual mean torque, although it does not fully reconstruct the instantaneous torque ripple waveform.

However, the improvement in torque ripple comes at the cost of increased losses. The copper loss increases from 874.78 W to 1003.65 W due to the additional harmonic current components. The core loss also increases from 264.92 W to 350.24 W, which is expected because harmonic injection introduces additional time-varying flux components in the machine. Therefore, for the PMaSynRM at 1000 rpm, the optimizer achieves torque ripple reduction while maintaining the mean operating point, but with a noticeable increase in copper and core losses.

5.3.1.2 Ferrite Spoke Behaviour

Since the same controller and optimizer structure is used as in the PMaSynRM case, the discussion is kept shorter and focuses mainly on the differences observed in the current response, flux estimation and torque ripple reduction.

Figure 5.11 shows the d and q-axis currents before harmonic injection.

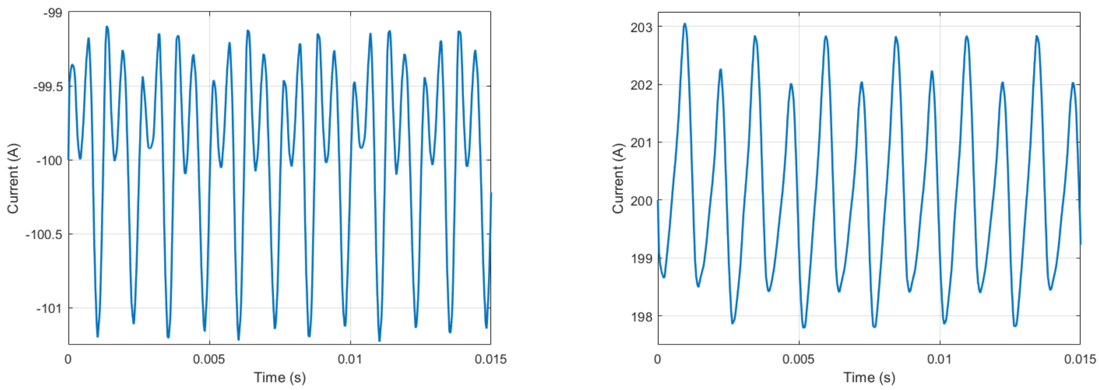

(a) d-axis current (b) q-axis current

Figure 5.11: Current response of the Ferrite Spoke PMSM at 1000 rpm before harmonic injection.

The currents remain close to their reference values, with only small periodic oscillations around the mean operating point.

The flux estimation results before harmonic injection are shown in Fig. 5.12.

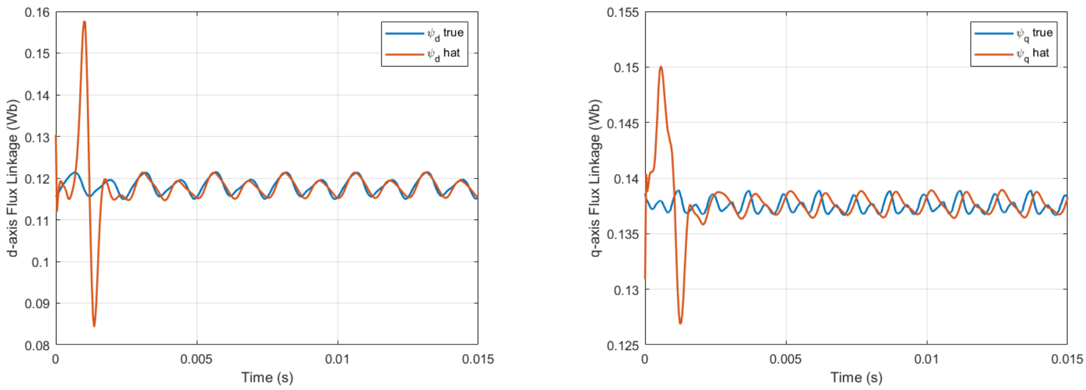

(a) *d*-axis flux linkage (b) *q*-axis flux linkage

Figure 5.12: Comparison between true and estimated flux linkages for the Ferrite Spoke PMSM at 1000 rpm before harmonic injection.

After a short initial transient, the estimated d and q-axis flux linkages follow the corresponding true flux linkages reasonably well.

Figure 5.13 compares the true and estimated torque before harmonic injection.

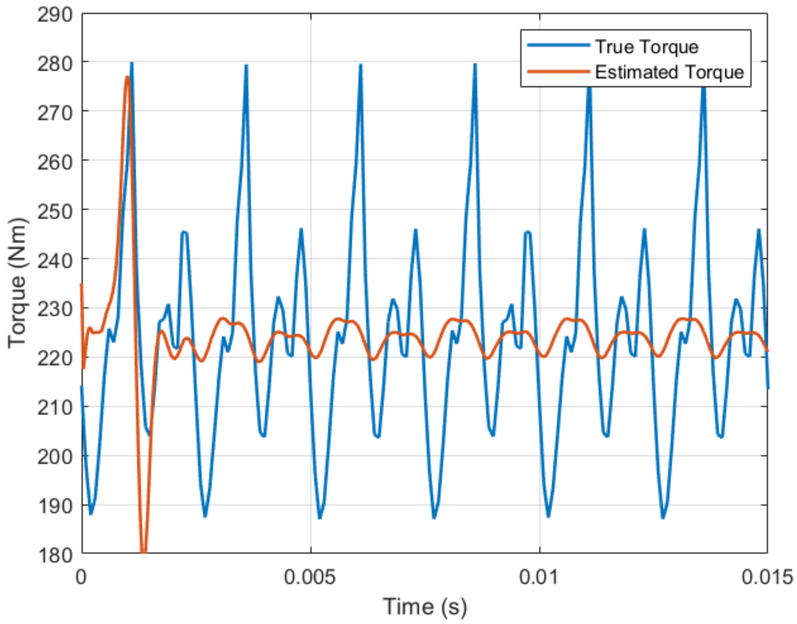

Figure 5.13: Comparison between true and estimated torque for the Ferrite Spoke PMSM at 1000 rpm before harmonic injection.

The true torque contains a significant ripple component, while the estimated torque mainly follows the mean torque level and captures only part of the oscillatory behaviour.

After harmonic injection, the resulting d and q-axis currents are shown in Fig. 5.14.

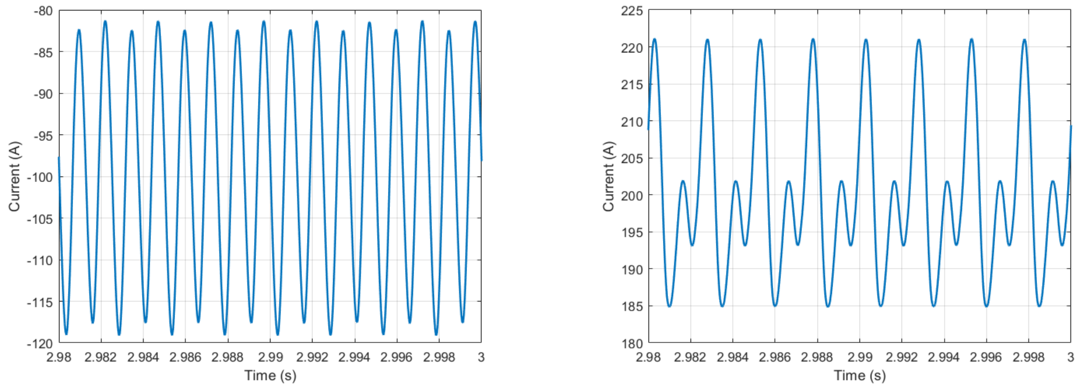

(a) d-axis current

(b) q-axis current

Figure 5.14: Current response of the Ferrite Spoke PMSM at 1000 rpm after harmonic injection.

The injected harmonic components are clearly visible in both current components. These additional current harmonics are introduced by the optimizer to compensate the dominant torque ripple components.

The evolution of the torque ripple reduction is shown in Fig. 5.15.

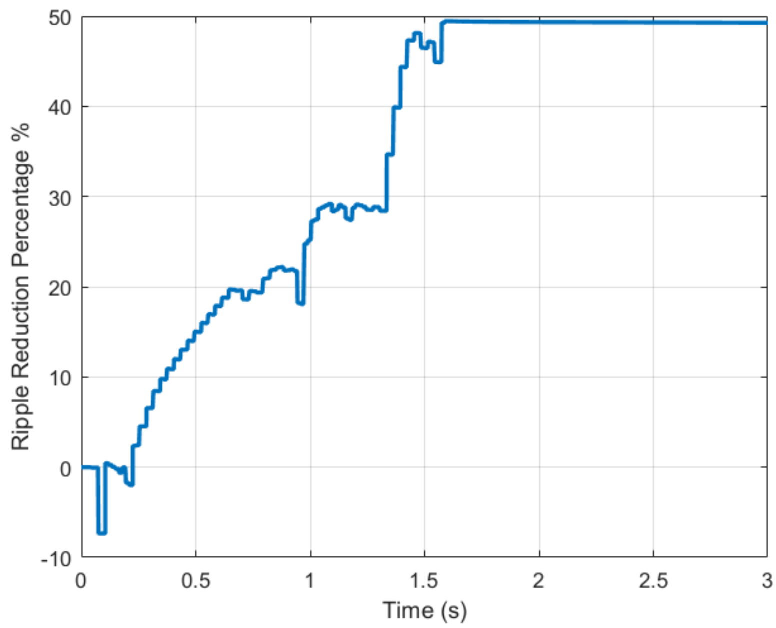

Figure 5.15: Torque ripple reduction percentage for the Ferrite Spoke PMSM at 1000 rpm.

The ripple reduction increases gradually during the optimization process and finally settles at approximately 50%. Compared with the PMaSynRM case, the final ripple reduction is lower, which indicates that the torque ripple components of the Spoke PMSM are more difficult to compensate using harmonic injection terms.

The torque response before and after harmonic injection is shown in Fig. 5.16.

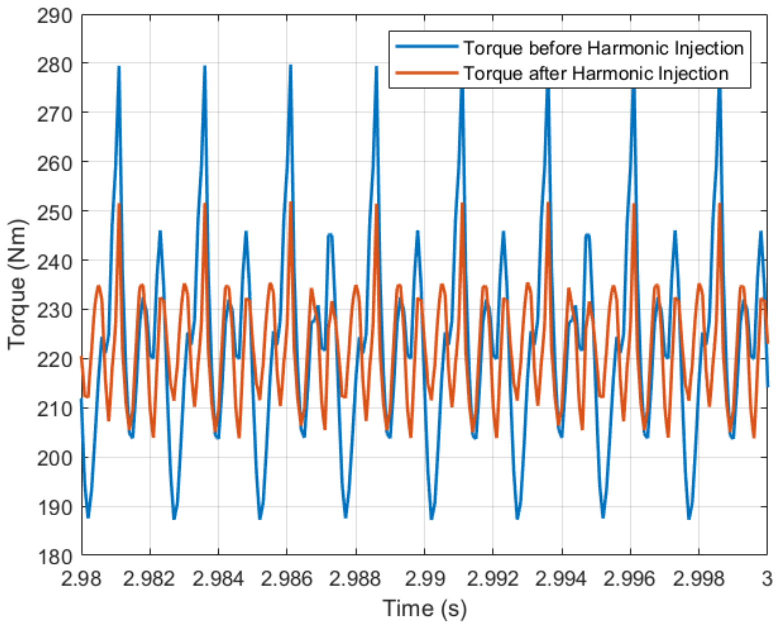

Figure 5.16: Torque response of the Ferrite Spoke PMSM at 1000 rpm before and after harmonic injection.

The original torque contains a large periodic ripple around the mean torque level. After harmonic injection, the torque ripple amplitude is reduced, although noticeable ripple remains in the optimized torque waveform.

Figure 5.17 shows the torque harmonic amplitude spectrum before and after harmonic injection for the Ferrite Spoke PMSM at 1000 rpm. Before harmonic injection, the torque ripple is mainly dominated by the 12th torque harmonic, followed by the 24th and 6th harmonics.

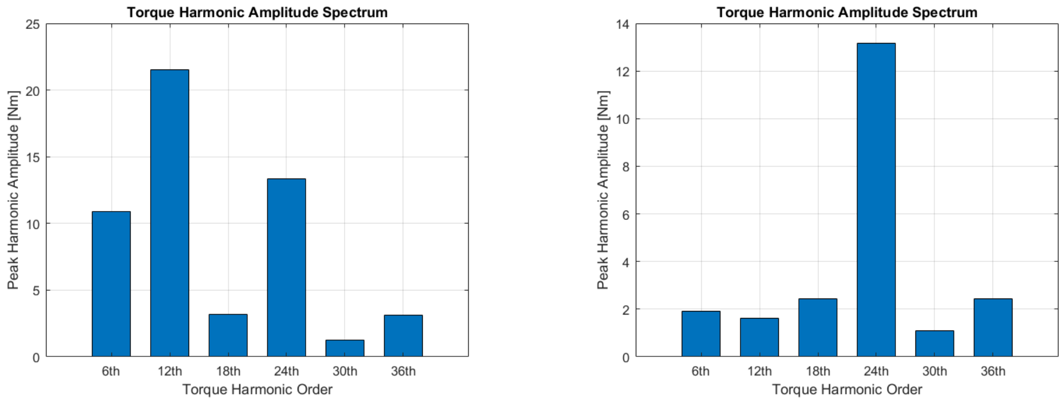

(a) Before harmonic injection

(b) After harmonic injection

Figure 5.17: Torque harmonic amplitude spectrum of the Ferrite Spoke PMSM at 1000 rpm before and after harmonic injection.

After harmonic injection, the 6th and 12th torque harmonics are strongly reduced. In particular, the 12th harmonic, which was the dominant component before injection, is significantly suppressed. However, the 24th harmonic remains relatively large and becomes the dominant remaining harmonic after injection. This explains why the total torque ripple is reduced, but not eliminated completely. The result also shows that the selected harmonic injection strategy is effective mainly for reducing the targeted lower-order harmonics, while higher-order torque harmonics still remain in the machine torque response.

As in the previous case, the post-injection flux linkages and estimated torque are not plotted separately. The final performance after harmonic injection is evaluated using the true machine torque response. The mean values of the relevant quantities are summarised in Table 5.2.

Table 5.2: Comparison of mean quantities and losses for the Ferrite Spoke PMSM at 1000 rpm before and after harmonic injection.

Quantity(Mean)	**Before Injection**	**After Injection**	**Unit**
i_d	-99.7	-100.1	A
i_q	200.1	199.6	A
T_e (Actual)	222	221.8	Nm
T_e (KF)	223.4	221.3	Nm
Copper loss	658.95	777.41	W
Core loss	402.03	440.60	W

From Table 5.2, it can be observed that the harmonic injection does not significantly change the mean current operating point of the Ferrite Spoke PMSM.

The mean actual torque remains almost unchanged, decreasing only slightly from 222 Nm to 221.8 Nm. This shows that the torque ripple reduction is achieved without causing a noticeable loss in average torque production.

The main penalty of harmonic injection is the increase in losses. The copper loss increases from 658.95 W to 777.41 W due to the additional harmonic current components. The core loss also increases from 402.03 W to 440.60 W, which indicates that the injected harmonics introduce additional flux dynamics in the machine.

5.3.2 Current Control and Torque Ripple Optimization at 6000 rpm

This section presents the current controller and torque ripple optimizer results for the electric machines at 6000 rpm. The selected operating point is $(i_d, i_q) = (-350\ \text{A}, 100\ \text{A})$. First, the controller and observer performance are evaluated without harmonic injection. Then, the effect of the harmonic current injection on current tracking and torque ripple reduction is presented.

5.3.2.1 PMaSynRM behaviour

At 6000 rpm, the available voltage margin is much smaller, and the controller has less freedom to track additional harmonic current components.

Figure 5.18 shows the d and q-axis currents before harmonic injection.

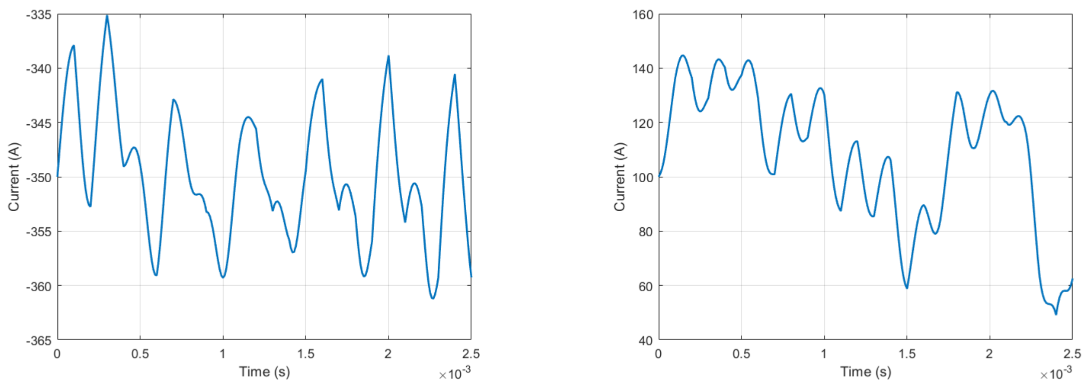

(a) d-axis current

(b) q-axis current

Figure 5.18: Current response of the PMaSynRM at 6000 rpm before harmonic injection.

The currents remain close to the intended high-speed operating region, although the waveforms contain noticeable oscillations. Compared with the 1000 rpm case, the current response is more affected by the high-speed operating condition and voltage limitation.

The flux estimation results before harmonic injection are shown in Fig. 5.19.

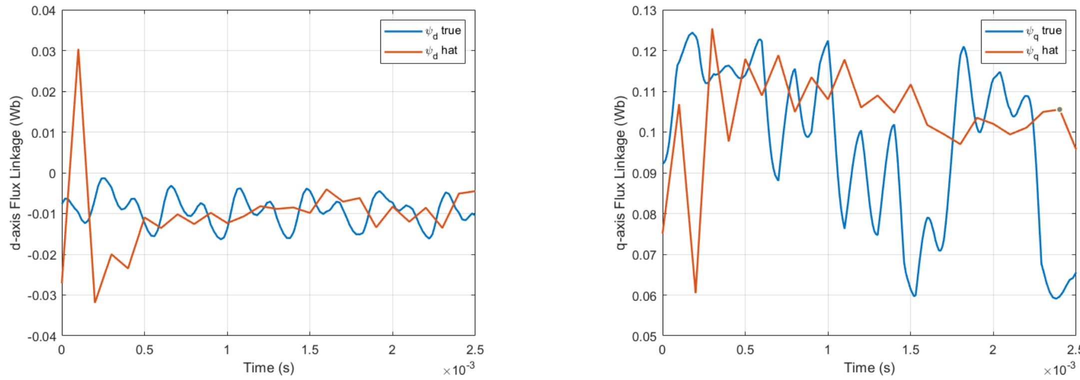

(a) *d*-axis flux linkage

(b) *q*-axis flux linkage

Figure 5.19: Comparison between true and estimated flux linkages for the PMaSynRM at 6000 rpm before harmonic injection.

The estimated flux linkages follow the general trend of the true flux linkages, but the agreement is not as close as in the 1000 rpm case. This is expected because the high-speed case contains stronger effects of delays and a more severe voltage-limited operating condition. The estimated fluxes still provide useful information about the flux variation before harmonic injection.

The flux estimation performance at 6000 rpm was also evaluated using a much smaller simulation sampling time. In the previous high-speed case, a sampling time of 1×10^{-4} s was used, whereas in this case the sampling time was reduced to 1×10^{-8} s. Figure 5.20 shows the comparison between the true and estimated d and q-axis flux linkages for the PMaSynRM at 6000 rpm for the new sampling time.

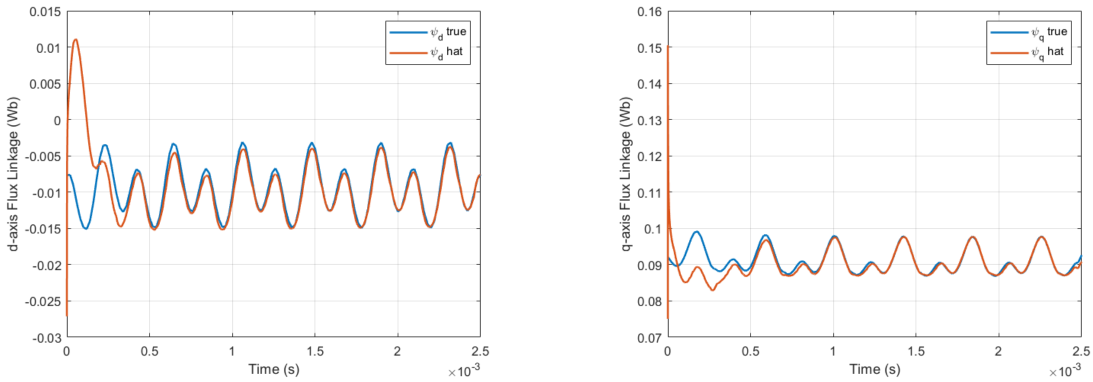

(a) d-axis flux linkage

(b) q-axis flux linkage

Figure 5.20: Comparison between true and estimated flux linkages for the PMaSynRM at 6000 rpm using a smaller simulation sampling time of 1×10^{-8} s.

Compared with the previous result, the agreement between the true and estimated flux linkages is significantly improved. After a short initial transient, the estimated flux linkages closely follow the true flux waveforms in both axes. This indicates that the mismatch observed previously was partly caused by the larger sampling time and the associated discretization effects.

The result therefore shows that the Kalman Filter is capable of accurately reconstructing the flux linkage harmonics when the sampling resolution is sufficiently high. However, in a practical digital controller, the achievable sampling frequency is limited by the computational capability of the controller hardware.

Figure 5.21 compares the true and estimated torque before harmonic injection.

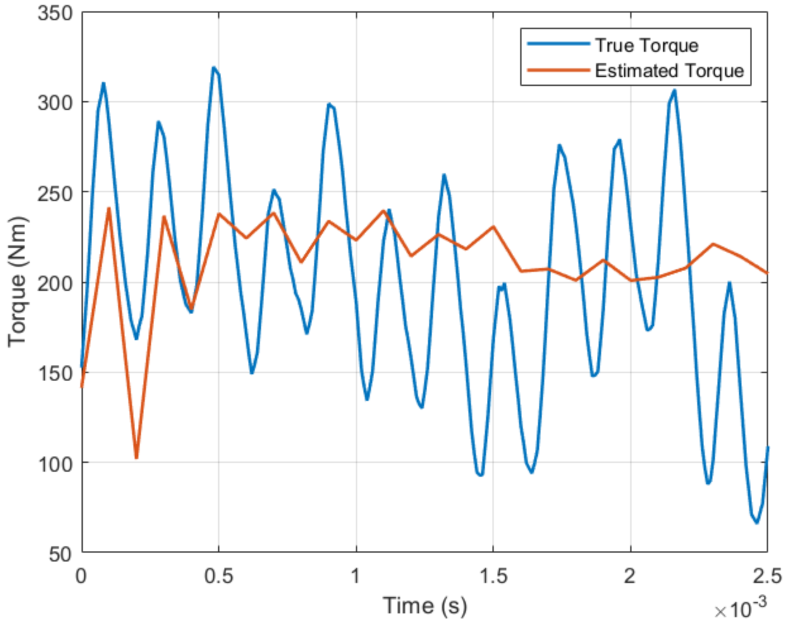

Figure 5.21: Comparison between true and estimated torque for the PMaSynRM at 6000 rpm before harmonic injection.

The true torque contains large high-frequency oscillations, while the estimated torque mainly follows the average torque trend and captures only a limited part of the ripple.

Figure 5.22 shows the d and q-axis currents after harmonic injection.

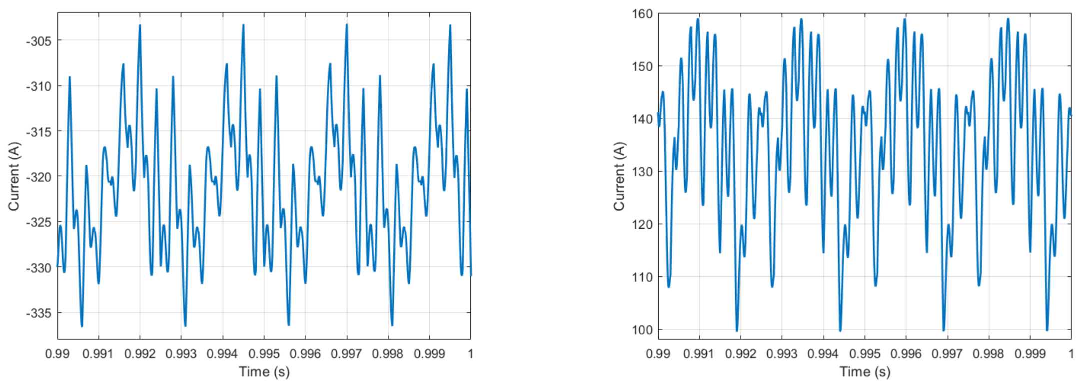

(a) d-axis current

(b) q-axis current

Figure 5.22: Current response of the PMaSynRM at 6000 rpm after harmonic injection.

Compared with the low-speed case, the mean current values and oscillatory components are more strongly affected. This is expected in field-weakening operation, where the available voltage margin for additional harmonic current tracking is limited.

In this high-speed case, an initial transient was observed in the torque response. Therefore, harmonic injection was not enabled from the beginning of the simulation. Instead, the optimizer was activated only after approximately 0.6 s, once the torque response had reached a more suitable steady-state condition. This avoids optimizing the harmonic currents based on transient torque behaviour.

The evolution of the torque ripple reduction is shown in Fig. 5.23.

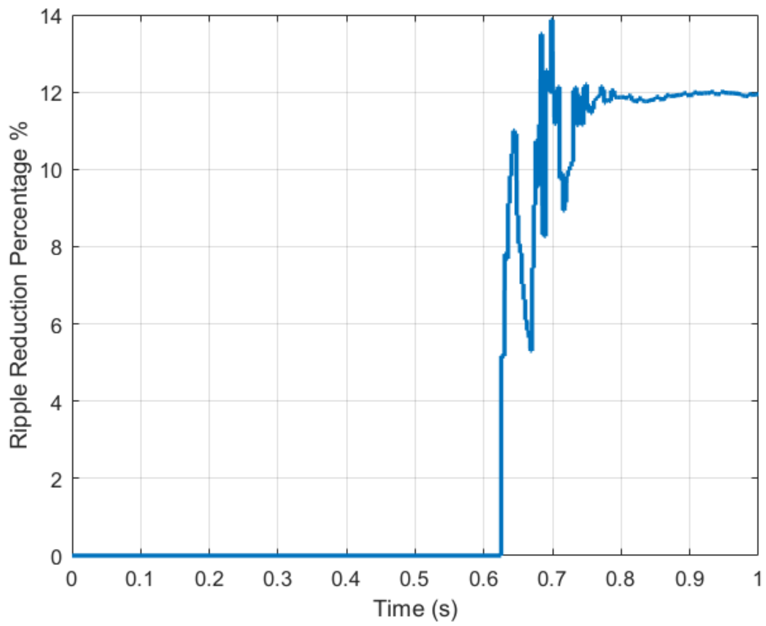

Figure 5.23: Torque ripple reduction percentage for the PMaSynRM at 6000 rpm.

The ripple reduction remains zero until the harmonic injection is activated after approximately 0.6 s. After activation, the optimizer initially shows some oscillatory behaviour before settling. The final ripple reduction is approximately 12%, which is considerably lower than the reduction achieved at 1000 rpm. This happens because the 12th harmonic currents could not be injected due to inverter switching limits.

The torque response before and after harmonic injection is shown in Fig. 5.24.

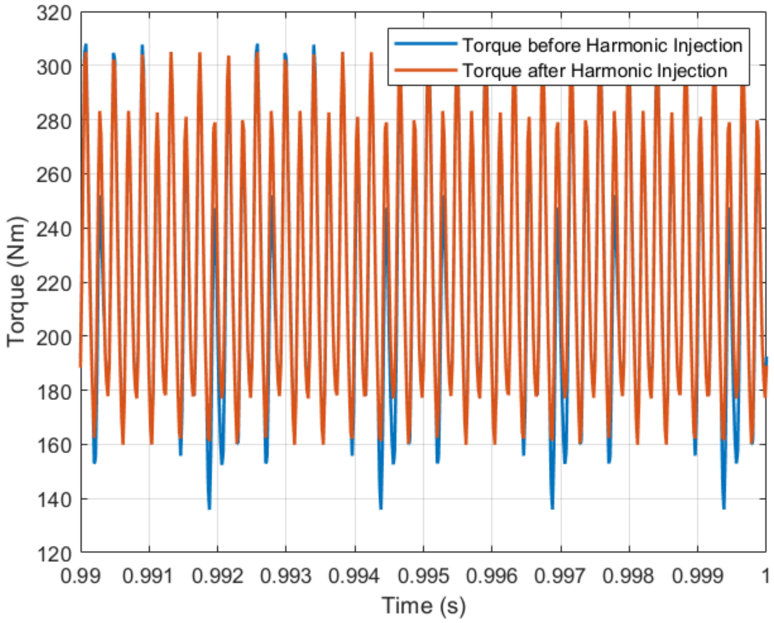

Figure 5.24: Torque response of the PMaSynRM at 6000 rpm before and after harmonic injection.

The torque ripple remains large after injection, although a small reduction can be observed. The injected harmonic currents are therefore able to reduce the ripple to some extent, but they cannot suppress the dominant torque oscillations as effectively as in the 1000 rpm case.

Figure 5.25 shows the torque harmonic amplitude spectrum before and after harmonic injection for the PMaSynRM at 6000 rpm. Before harmonic injection, the torque ripple is dominated by the 12th torque harmonic. The 6th harmonic is also significant, while the 24th harmonic has a smaller contribution. The remaining higher-order components are comparatively small.

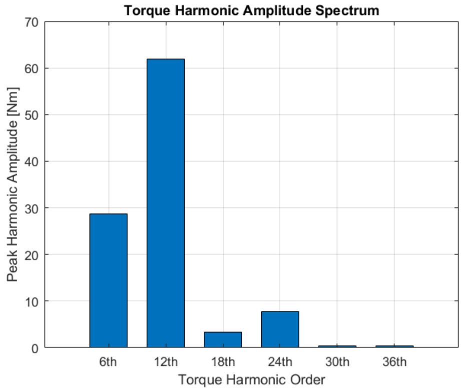

(a) Before harmonic injection

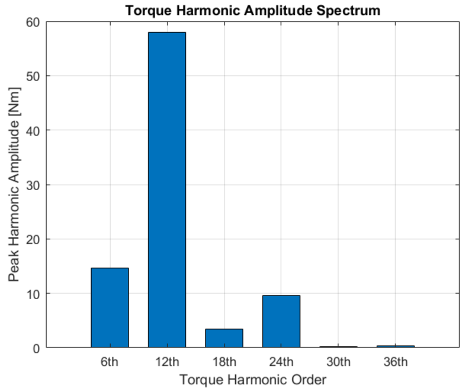

(b) After harmonic injection

Figure 5.25: Torque harmonic amplitude spectrum of the PMaSynRM at 6000 rpm before and after harmonic injection.

After harmonic injection, the 6th harmonic is reduced considerably, while the 12th harmonic is only slightly reduced. This explains why the total torque ripple reduction at 6000 rpm is much lower than in the 1000 rpm case. At high speed, the 12th harmonic of currents are not injected. As a result, the optimizer is able to reduce part of the torque ripple, especially the 6th harmonic contribution, but it cannot fully suppress the dominant 12th harmonic component.

As in the previous cases, the post-injection flux linkages and estimated torque are not plotted separately. The final post-injection performance is evaluated using the true machine torque response. The mean values of the relevant quantities and the corresponding losses are summarised in Table 5.3.

Table 5.3: Comparison of mean quantities and losses for the PMaSynRM at 6000 rpm before and after harmonic injection.

Quantity(Mean)	**Before Injection**	**After Injection**	**Unit**
i_d	-351.1	-325.4	A
i_q	101.6	126.4	A
T_e (Actual)	195	219.5	Nm
T_e (KF)	207.9	215	Nm
Copper loss	910.73	978.39	W
Core loss	1560.04	1632.28	W

From Table 5.3, it can be observed that the harmonic injection causes a noticeable shift in the mean current operating point at 6000 rpm. This indicates that, unlike the 1000 rpm case, the controller is not able to maintain the original current operating point exactly after harmonic injection.

The mean actual torque increases from 195 Nm to 219.5 Nm after harmonic injection. This increase is mainly caused by the shift in the mean current components, especially the increase in i_q.

The losses also increase after harmonic injection. The copper loss increases from 910.73 W to 978.39 W due to the additional harmonic current components. The core loss increases from 1560.04 W to 1632.28 W, which is expected at high speed because additional harmonic flux variations are introduced. But this increase in losses is much lesser than 1000 rpm case. This is because the 12th harmonics of current were not injected.

5.3.2.2 Ferrite Spoke PMSM behaviour

Figure 5.26 shows the d and q-axis current responses before harmonic injection.

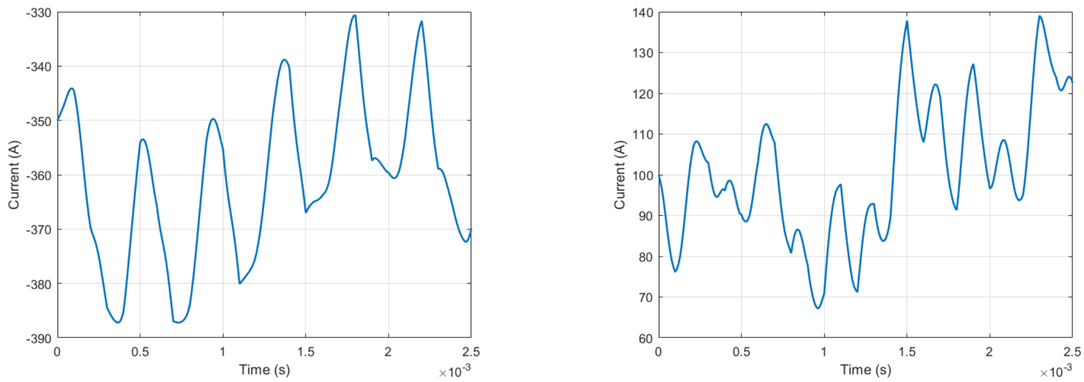

(a) d-axis current

(b) q-axis current

Figure 5.26: Current response of the Ferrite Spoke PMSM at 6000 rpm before harmonic injection.

The currents remain around the selected high-speed operating point, but noticeable oscillations are present.

The flux estimation results before harmonic injection are shown in Fig. 5.27.

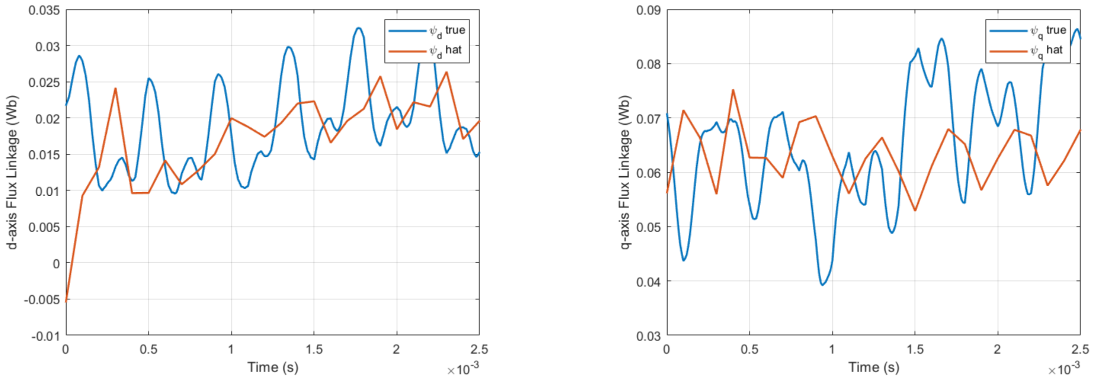

(a) *d*-axis flux linkage

(b) *q*-axis flux linkage

Figure 5.27: Comparison between true and estimated flux linkages for the Ferrite Spoke PMSM at 6000 rpm before harmonic injection.

The estimated flux linkages follow the general variation of the true flux linkages, although the agreement is not as close as in the 1000 rpm case. Nevertheless, the Kalman Filter still captures the main trend of the flux variation before harmonic injection.

Figure 5.28 compares the true and estimated torque before harmonic injection.

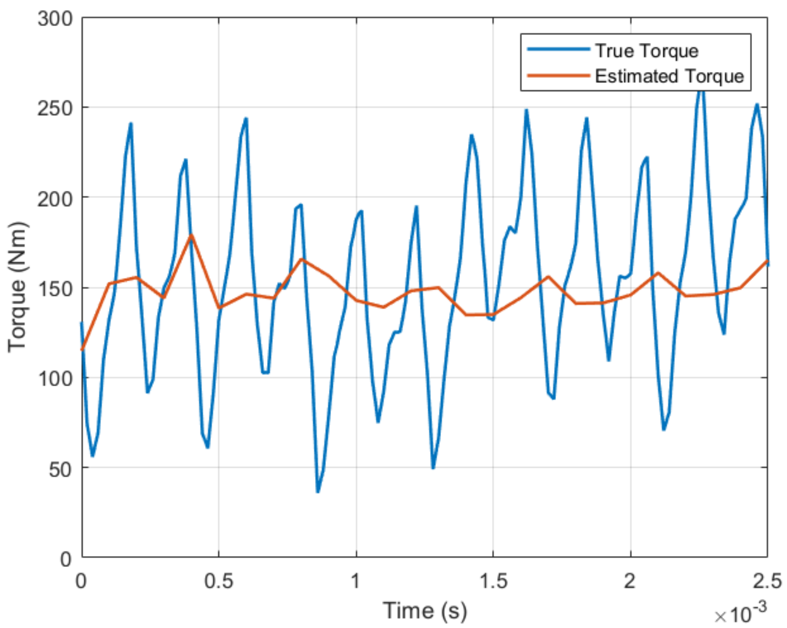

Figure 5.28: Comparison between true and estimated torque for the Ferrite Spoke PMSM at 6000 rpm before harmonic injection.

The true torque contains a large ripple component, while the estimated torque mainly follows the average torque level and captures only a limited part of the oscillatory behaviour.

After harmonic injection, the resulting d and q-axis currents are shown in Fig. 5.29.

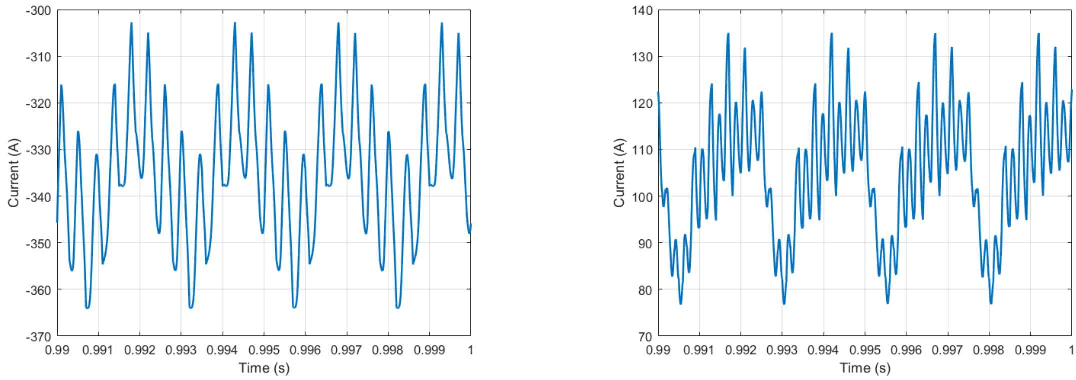

(a) d-axis current (b) q-axis current

Figure 5.29: Current response of the Ferrite Spoke PMSM at 6000 rpm after harmonic injection.

The harmonic components are clearly visible in both current waveforms. Compared with the low-speed case, the current oscillations are larger and the mean current values are more affected by the high-speed operating condition.

The evolution of the torque ripple reduction is shown in Fig. 5.30.

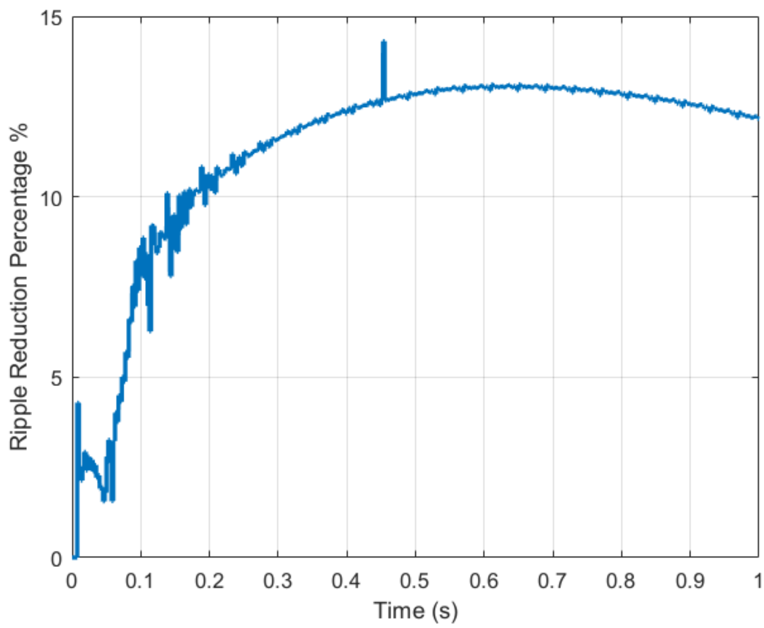

Figure 5.30: Torque ripple reduction percentage for the Ferrite Spoke PMSM at 6000 rpm.

Since the initial transient is relatively brief, the optimizer begins improving the ripple reduction much earlier than in the PMaSynRM high-speed case. The ripple reduction increases gradually and reaches approximately 12.5%.

The torque response before and after harmonic injection is shown in Fig. 5.31.

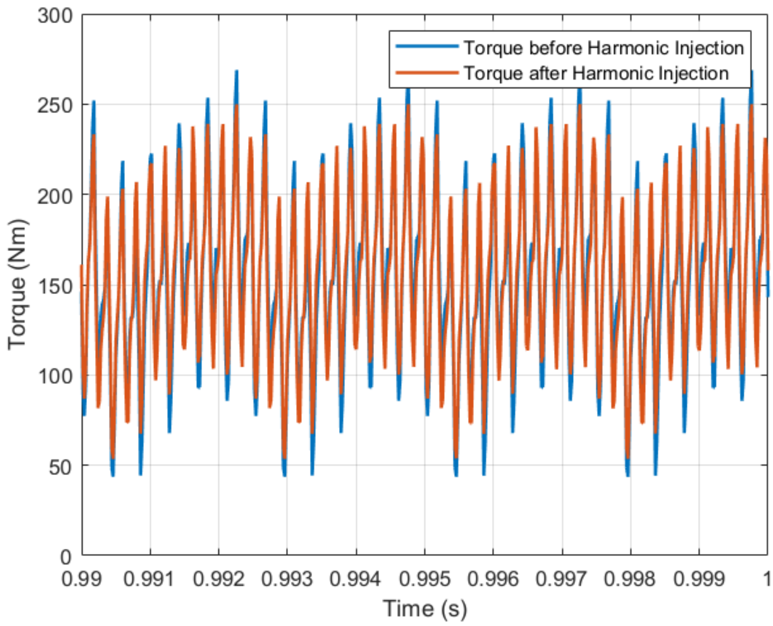

Figure 5.31: Torque response of the Ferrite Spoke PMSM at 6000 rpm before and after harmonic injection.

The original torque contains a large ripple component, and the optimized torque shows only a moderate reduction in ripple amplitude.

Figure 5.32 shows the torque harmonic amplitude spectrum before and after harmonic injection for the Ferrite Spoke PMSM at 6000 rpm. Before harmonic injection, the torque ripple is mainly dominated by the 12th torque harmonic. The 24th harmonic is also significant, while the 6th harmonic has a moderate contribution. The remaining higher-order harmonics are comparatively small.

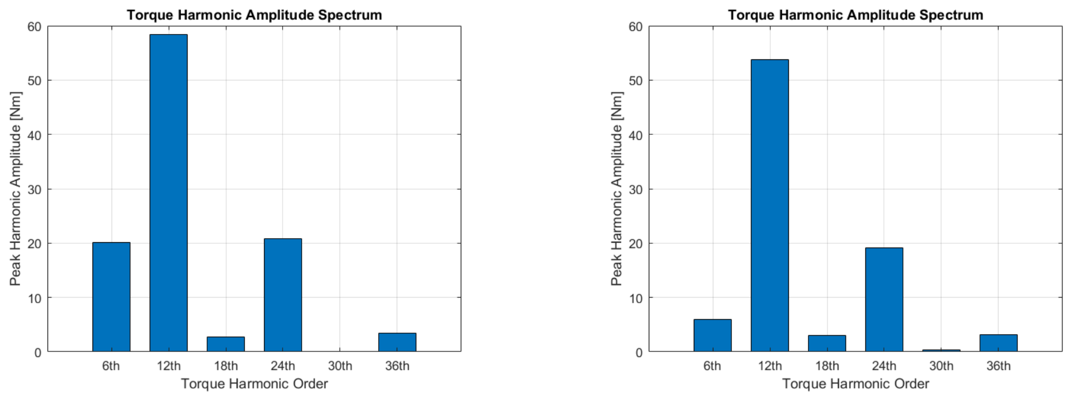

(a) Before harmonic injection (b) After harmonic injection

Figure 5.32: Torque harmonic amplitude spectrum of the Ferrite Spoke PMSM at 6000 rpm before and after harmonic injection.

After harmonic injection, the 6th harmonic is reduced considerably. However, the 12th harmonic remains the dominant component and is only slightly reduced. The 24th harmonic also remains relatively large after injection. This explains why the total torque ripple reduction at 6000 rpm is limited compared with the 1000 rpm case.

As in the previous high-speed case, the post-injection flux linkages and estimated torque are not plotted separately. The final performance after harmonic injection is evaluated using the true torque response of the machine model. The mean values of the main quantities and the corresponding losses are summarised in Table 5.4.

Table 5.4: Comparison of mean quantities and losses for the Ferrite Spoke PMSM at 6000 rpm before and after harmonic injection.

Quantity(Mean)	**Before Injection**	**After Injection**	**Unit**
i_d	-355	-339.6	A
i_q	102.1	106.8	A
T_e (Actual)	150.2	155.7	Nm
T_e (KF)	149.7	158	Nm
Copper loss	478.48	670.61	W
Core loss	3306.03	3592.45	W

From Table 5.4, it can be observed that the harmonic injection causes a moderate shift in the mean current operating point of the Ferrite Spoke PMSM at 6000 rpm.

The mean actual torque increases from 150.2 Nm to 155.7 Nm after harmonic injection. This increase is mainly due to the change in the mean current components, especially the reduction in negative i_d and the slight increase in i_q.

The losses increase noticeably after harmonic injection. The copper loss increases from 478.48 W to 670.61 W, which indicates that the injected harmonic current components significantly increase the RMS current content. The core loss also increases from 3306.03 W to 3592.45 W. The increase in core loss is, however, much less.

6
Conclusion

6.1 Results from present work

The motor design and analysis carried out in this thesis show that all three machine topologies are capable of satisfying the required traction performance. However, they achieve this performance through different electromagnetic, material and packaging trade-offs. The NdFeB VPMSM provides a strong reference design with high torque density, the lowest active volume and good torque-producing capability, but it relies heavily on rare-earth magnet material and exhibits the highest local magnetic flux. The hybrid PMaSynRM reduces the amount of NdFeB material while maintaining competitive torque-speed performance and high drive-cycle efficiency. This reduction in rare-earth magnet usage, however, comes with a higher copper-loss. The ferrite spoke PMSM demonstrates that a rare-earth-free design can achieve comparable traction capability by using a larger rotor diameter and a flux-concentrating rotor structure, but this leads to higher core losses, larger machine mass and a heavier overall design.

Among the three machines, the hybrid PMaSynRM provides the most balanced performance in this study. It achieves the lowest drive-cycle energy losses and the highest average electromagnetic efficiency in both the city and highway driving cycles, while also reducing NdFeB magnet usage compared with the reference V-PMSM. The ferrite spoke PMSM remains attractive from a rare-earth-free and low-cost perspective, but its higher hysteresis and eddy-current losses, especially at higher speeds, reduce its overall efficiency. The sustainability assessment further shows that the VPMSM has the lowest mass and embodied CO_2, but the highest cost and strongest NdFeB dependency. The spoke PMSM has the highest mass and emissions, but the lowest cost and no rare-earth magnet dependency. Therefore, considering electromagnetic performance, drive-cycle efficiency, material usage, cost and sustainability together, the hybrid PMaSynRM offers the best overall compromise for the considered traction motor application.

It is shown that a Map Based ROM Model can be a good replacement of an actual 2D FEA Model. Using ROM, saves a lot of time and computational resources without degrading the quality of simulation. The LQI Controller and the Torque Ripple Optimizer performed well even when sampling delays and Zero Order Hold was introduced. Moreover, the controller stabilises the currents in case of any disturbance or changes in the operating condition. The Torque Ripple Optimizer is able to reduce the torque ripple (respecting inverter switching limits) by upto 70-80% for any user command. Injecting Current harmonics does not make the mean currents and mean torque drift at low speed which indicates its robustness, but it drifts moderately at high speed. The copper losses and core losses increase by approximately 20-30% when harmonics are injected.

It was found that at steady state, a Kalman Filter is not able to estimate the torque ripple fully due to factors other than flux harmonics such as cogging torque. However, it predicts the fluxes and mean torque very accurately which can be useful for driving cycle analysis of the EV but not useful for NVH purposes like torque ripple reduction.

6.2 Future Work

In the current thesis, the current controller depends on feedforward voltages to stabilise the currents at the operating point. In the future, a Robust Non-Linear Model Predictive Controller could be developed which is a very powerful controller and might not need feedforward voltages at all. However, from a thesis point of view, it is a very advanced form of controller and needs a lot of in-depth controls knowledge, so one must be cautious before taking it up.

Alternatively AI-ML Models could be used to replace the controller and the estimator. These can be very accurate if they are modeled correctly. However Pure Neural Network Models lack the knowledge of physics and controls, so it cannot be trusted. Instead, one can use Physics Informed Neural Networks that could be reliable.

This thesis can be further extended to implement a control system in a real digital controller and processors like Digital Signal Processors (DSP) and Field-Programmable Gate Arrays (FPGA) which are widely used in Electric Vehicles. However Steady State + Transient Periods + Temperature Effects + all operating points + Regeneration are necessary to be modeled unlike the current thesis.

Inverter dynamics and Inverter Effects for the most part have not been fully considered in this thesis. It could be interesting to see how inverter dynamics affects the current controller. In the present thesis, the torque ripple is solely produced due to the electromagnetic nature of the motor. Inverter Dynamics will bring in their own harmonics that could increase the torque ripple. It would be interesting to see how the torque ripple optimizer deals with it.

In the present thesis, a speed controller was not developed as the thesis was limited to steady state torque ripple reduction. Adding a speed controller would bring in the mechanical dynamics which would help surface a lot of information that was hidden in steady state.

For the PMaSynRM and Spoke Type PMSM, different rotor designs can be explored. Additionally a full thermal analysis and a mechanical analysis could be performed using Ansys Workbench and Ansys Fluent.

Bibliography

[1] N. Bianchi, S. Bolognani, D. Bon, and M. Dai Pré, “Rotor flux-barrier design for torque ripple reduction in synchronous reluctance and PM-assisted synchronous reluctance motors,” *IEEE Transactions on Industry Applications*, vol. 45, no. 3, pp. 921–928, 2009.

[2] P. Mattavelli, L. Tubiana, and M. Zigliotto, “Torque-ripple reduction in PM synchronous motor drives using repetitive current control,” *IEEE Transactions on Power Electronics*, vol. 20, no. 6, pp. 1423–1431, 2005.

[3] J. Guo, W. Li, J. Wang, Y. Luo, and K. Li, “Safe and energy-efficient car-following control strategy for intelligent electric vehicles considering regenerative braking,” *IEEE Transactions on Intelligent Transportation Systems*, vol. 23, no. 7, pp. 7070–7081, Jul. 2022, doi: 10.1109/TITS.2021.3066611.

[4] P. Pandurangan and N. Manakshya, “Permanent magnet synchronous machine using ferrite vs rare earth magnets-how do they compare?,” M.S. thesis, Department of Electrical Engineering, Chalmers University of Technology, Gothenburg, Sweden, 2021.

[5] J. Pyrhönen, T. Jokinen, and V. Hrabovcová, *Design of Rotating Electrical Machines*, 2nd ed. Chichester, U.K.: Wiley, 2013.

[6] A. Sinervo, *Effects of Slotting and Unipolar Flux on Magnetic Pull in a Two-Pole Induction Motor with an Extra Four-Pole Stator Winding.* Doctoral dissertation, Department of Electrical Engineering, Aalto University, Espoo, Finland, 2013.

[7] H.-J. Kim and S.-W. Baek, “Optimal design of a 15 kW-class interior permanent magnet synchronous motor for micro-EV traction using artificial neural network models,” *Microsystem Technologies*, vol. 29, no. 8, pp. 1165–1179, 2023, doi: 10.1007/s00542-023-05471-4.

[8] M. Tetik and F. Parlak, “Velocity vector controlled S-curve motion profile in permanent magnet synchronous machine (PMSM),” *Technological Applied Sciences*, vol. 12, no. 4, pp. 203–217, 2017, doi: 10.12739/NWSA.2017.12.4.2A0128.

[9] H. Chu, H. Chen, B. Gao, and H. Zhao, “A novel torque controller with direct flux control for permanent magnet synchronous motor,” *IFAC-PapersOnLine*, vol. 50, no. 1, pp. 11589–11594, 2017, doi: 10.1016/j.ifacol.2017.08.1515.

[10] X. Li, Y. Yin, Y. Zhou, W. Liu, and K. Zhao, “The non-singular fast terminal sliding mode control of interior permanent magnet synchronous motor based on deep flux weakening switching point tracking,” *Energy Engineering*, vol. 120, no. 2, pp. 277–297, 2023, doi: 10.32604/ee.2023.022461.

[11] G. Bertotti, "General properties of power losses in soft ferromagnetic materials," *IEEE Transactions on Magnetics*, vol. 24, no. 1, pp. 621–630, Jan. 1988, doi: 10.1109/20.43994.
[12] E. Jin, "The knee point: The 'cliff edge' of irreversible demagnetization," *SDM Magnetics*. [Online]. Available: `https://sdmmagnets.com/knee-point/`.
[13] Volvo Trucks, "Electromobility made easy. Electric trucks are here," Apr. 12, 2018. [Online]. Available: `https://www.volvotrucks.com/en-en/news-stories/stories/2018/apr/electromobility-made-easy.html`.
[14] AK Steel, "DI-MAX M-19 nonoriented electrical steel," material datasheet. [Online]. Available: `https://www.lookpolymers.com/pdf/AK-Steel-DI-MAX-M-19-Nonoriented-Electrical-Steel.pdf`.
[15] S. Sprague, Ed., *Lamination Steels Third Edition: A Compendium of Lamination Steel Alloys Commonly Used in Electric Motors*. South Dartmouth, MA, USA: Electric Motor Education and Research Foundation, 2007, MIT OpenCourseWare excerpt: "AK Steel Di-Max M-19, Fully Processed, .014 inch (.36 mm, 29 gauge)." [Online]. Available: `https://ocw.mit.edu/courses/6-685-electric-machines-fall-2013/64bf1faf0a973d9607334321dd252794_MIT6_685F13_ps03data.pdf`.
[16] TDK Corporation, "FB13B: Ferrite magnet," product datasheet. [Online]. Available: `https://product.tdk.com/system/files/dam/doc/product/magnet/magnet/ferrite/catalog/magnet_fb_fb13b_en.pdf`.
[17] Arnold Magnetic Technologies, "N42SH," product datasheet. [Online]. Available: `https://www.arnoldmagnetics.com/wp-content/uploads/2017/11/N42SH-151021.pdf`.
[18] C. Sahin, "Comparison of aluminum and copper winding materials for switched reluctance machines with finite element analysis," *Ingeniería e Investigación*, vol. 43, no. 2, p. e102038, 2023, doi: 10.15446/ing.investig.102038.
[19] A. Bardalai, D. Gerada, T. Zou, M. Degano, C. Zhang, and C. Gerada, "Comparison of AC losses in the winding of electrical machines with fixed strands positions, fixed conductor shapes and random winding," *Energies*, vol. 15, no. 15, p. 5701, 2022, doi: 10.3390/en15155701.
[20] H. A. Wheeler, "Formulas for the skin effect," *Proceedings of the IRE*, vol. 30, no. 9, pp. 412–424, Sep. 1942, doi: 10.1109/JRPROC.1942.232015.
[21] T. Tokuda, M. Sanada, and S. Morimoto, "Influence of rotor structure on performance of permanent magnet assisted synchronous reluctance motor," in *Proc. 2009 International Conference on Electrical Machines and Systems (ICEMS)*, Tokyo, Japan, 2009, pp. 1–6, doi: 10.1109/ICEMS.2009.5382889.
[22] M. Muthusamy, J. Hendershot, and P. Pillay, "Design of a spoke type PMSM with SMC stator core for traction applications," *IEEE Transactions on Industry Applications*, vol. 59, no. 2, pp. 1418–1436, Mar-Apr. 2023, doi: 10.1109/TIA.2022.3223636.
[23] E. Carraro, N. Bianchi, S. Zhang, and M. Koch, "Design and performance comparison of fractional slot concentrated winding spoke type synchronous motors with different slot-pole combinations," *IEEE Transactions on Industry Applications*, vol. 54, no. 3, pp. 2276–2284, May–Jun. 2018, doi: 10.1109/TIA.2018.2807382.

[24] J. A. Güemes, A. M. Iraolagoitia, P. Fernández, and M. P. Donsión, "Comparative study of PMSM with integer-slot and fractional-slot windings," in *Proc. XIX International Conference on Electrical Machines (ICEM)*, Rome, Italy, Sep. 2010, pp. 1–6, doi: 10.1109/ICELMACH.2010.5608202.
[25] N. Manakshya, Z. Huang, and T. Thiringer, "Demagnetisation and performance study of neodymium and ferrite assisted SynRM," in *Proc. 2024 International Conference on Electrical Machines (ICEM)*, Torino, Italy, 2024, doi: 10.1109/ICEM60801.2024.10700270.
[26] X. Zhang, D. Gerada, Z. Xu, F. Zhang, and C. Gerada, "A review of carbon emissions from electrical machine materials," *Electronics*, vol. 13, no. 9, Art. no. 1714, 2024, doi: 10.3390/electronics13091714.
[27] D. Washio and K. Akatsu, "Study on EV traction motors for life cycle assessment considering changes in winding material and magnet configuration," *World Electric Vehicle Journal*, vol. 17, no. 3, Art. no. 157, 2026, doi: 10.3390/wevj17030157.
[28] A. Nordelöf, E. Grunditz, S. Lundmark, A.M. Tillman, M. C. D. Alatalo, and T. Thiringer, "Life cycle assessment of permanent magnet electric traction motors," *Transportation Research Part D: Transport and Environment*, vol. 67, pp. 263–274, 2019, doi: 10.1016/j.trd.2018.11.004.
[29] International Energy Agency, *Rare Earth Elements: Pathways to Secure and Diversified Supply Chains*. Paris, France: IEA, 2026. [Online]. Available: `https://www.iea.org/reports/rare-earth-elements`.
[30] T. Glad and L. Ljung, *Control Theory: Multivariable and Nonlinear Methods*. London, U.K.: Taylor & Francis, 2000, doi: 10.1201/9781315274737.
[31] A. Erixon and A. Lind-Anderton, "Parameter estimation using a self-commissioning sequence for internal permanent magnet synchronous motors: Determining the inductances L_d, L_q and the stator resistance R_s required to tune a PI current regulator, using high frequency voltage source inverter noise," M.S. thesis, Department of Electrical Engineering, Chalmers University of Technology, Gothenburg, Sweden, 2022.

A

Appendix A

A.1 Gradient Plots of the Drive Cycle

The road gradient profiles used for the city and highway driving cycles are shown in Fig. A.1. These profiles were applied as external road-grade inputs in the vehicle simulation.

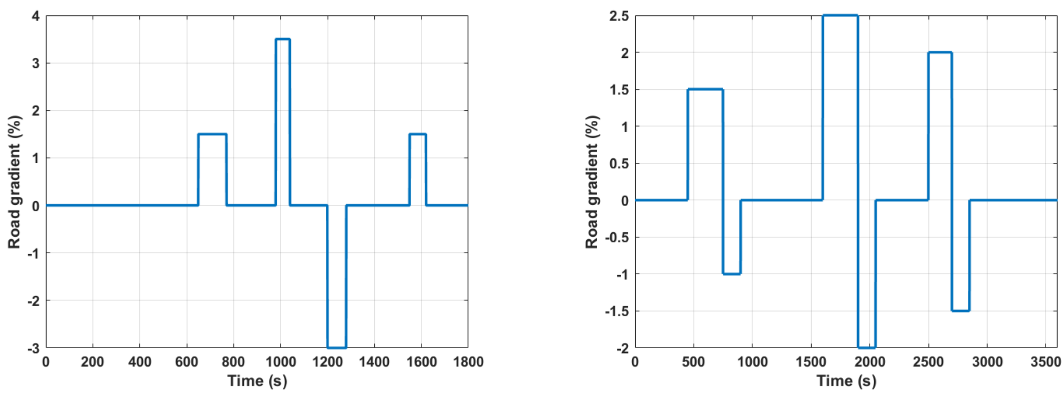

(a) City driving cycle **(b)** Highway driving cycle

Figure A.1: Road gradient profiles used in the vehicle simulations.

A.2 Gear Selection Plots during Drive Cycle

The overall gear-ratio profiles used for the city and highway driving cycles are shown in Fig. A.2. The lower gear ratio of 14.2 was used during most of the cycle, while the higher gear ratio of 22 was selected during specific operating intervals depending on the driving condition.

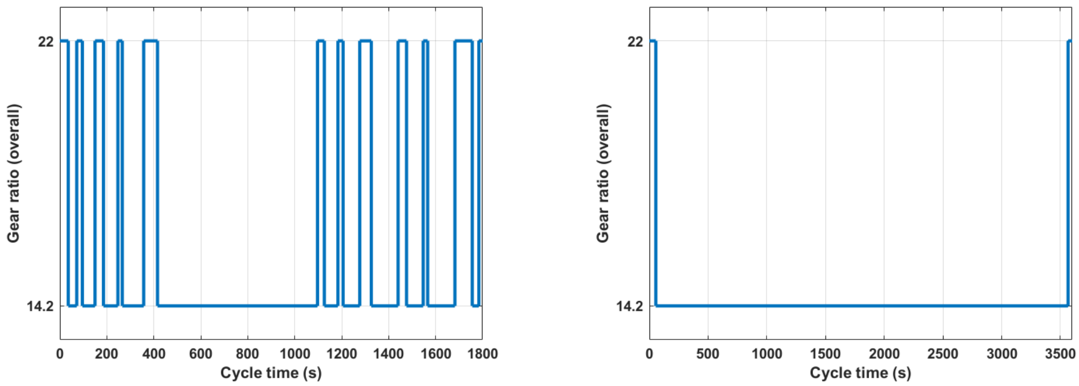

(a) City driving cycle

(b) Highway driving cycle

Figure A.2: Gear Selection during vehicle simulations.

A.3 Short-Circuit Currents

The d and q-axis current responses of PMaSynRM during the short-circuit simulation are shown in Fig. A.3. The currents exhibit a damped oscillatory response after the short-circuit is applied, with the largest positive and negative current peaks occurring shortly after the fault initiation.

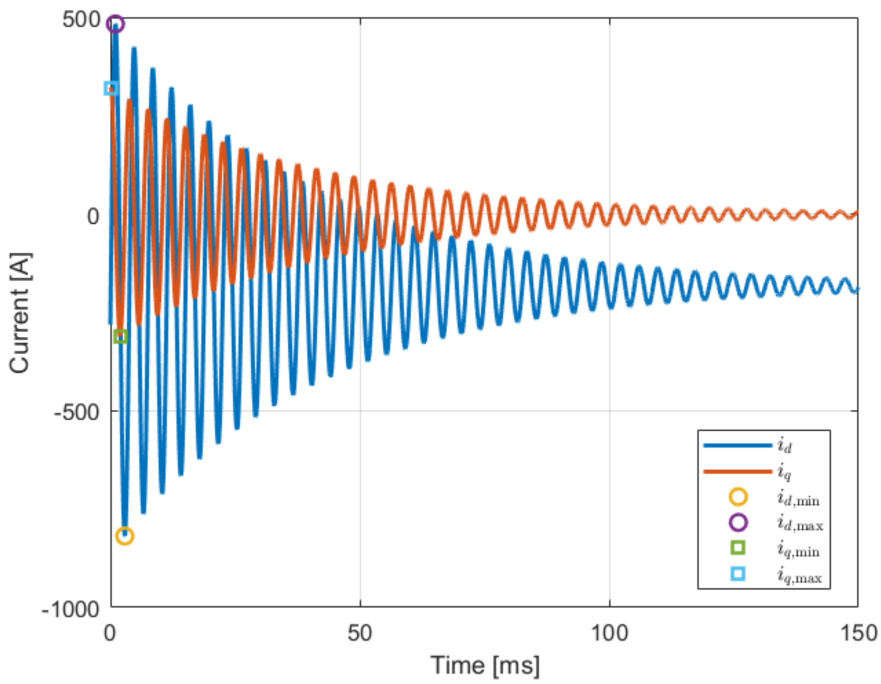

Figure A.3: Damped d- and q-axis current response during the short-circuit simulation of PMaSynRM. The markers indicate the maximum and minimum values of i_d and i_q.

A.4 Mechanical Transmitted Power Maps

The mechanical transmitted power maps of the three optimized machines are shown in Fig. A.4. The black curve represents the torque-speed operating envelope, while the contour lines indicate the transmitted mechanical power levels over the speed-torque plane.

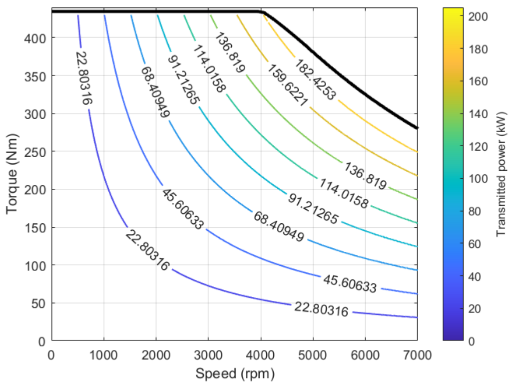

(a) Hybrid PMaSynRM

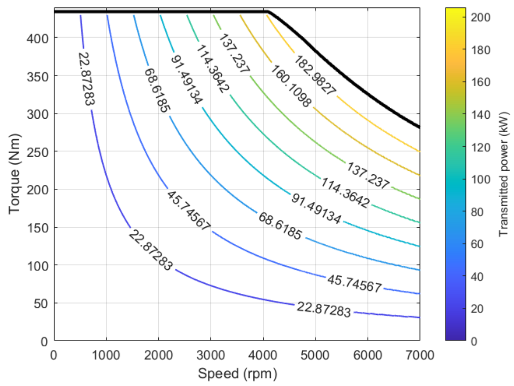

(b) NdFeB VPMSM

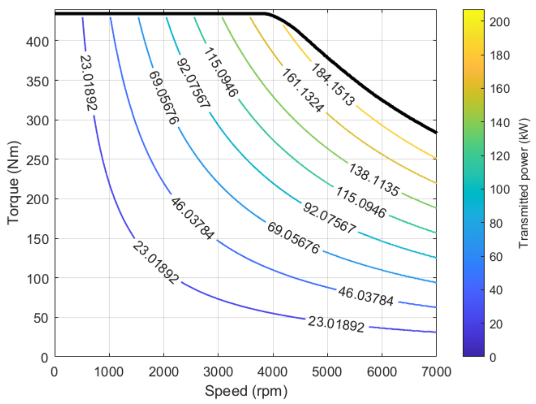

(c) Ferrite spoke PMSM

Figure A.4: Mechanical transmitted power maps of the three optimized machines.

DEPARTMENT OF ELECTRICAL ENGINEERING
CHALMERS UNIVERSITY OF TECHNOLOGY
Gothenburg, Sweden
www.chalmers.se

CHALMERS
UNIVERSITY OF TECHNOLOGY